REPUBLIC OF IRAQ

MINISTRY OF HIGHER EDUCATION AND SECINTIFIC RESEARCH

AL-FURAT AL-AWSAT TECHNICAL UNIVERSITY

ENGINEERING TECHNICAL COLLEGE – NAJAF

Investigation The Performance of Double-Pass Solar Air Heater with Various Types of Absorption Plates

Fatima Abd-Allatif Tali

M.TECH.

IN MECHANICAL ENGINEERING TECHNIGUES OF POWER

2023

Investigation The Performance of Double-Pass Solar Air Heater with Various Types of Absorption Plates

A THESIS

SUBMITTED TO THE DEPARTMENT OF MECHANICAL ENGINEERING TECHNIQUES OF POWER

AS PARTIAL FULFILLENT OF THE REQUIRMENTS FOR MASTER DEGREE OF THERMAL TECHNOLOGIES IN MECHANICAL ENGINEERING TECHNIQUES OF POWER (M. TECH.)

BY

FATIMA ABD-ALLATIF TALI

(B. Tec. Automobile Eng.**)**

2016

Supervised by:

Lec. Dr. Salah M. Salih **Asst Prof. Dr Tahssen Ali Hussain**

February / 2023

بِسْمِ اللَّهِ الرَّحْمَٰنِ الرَّحِيمِ

هُوَ الَّذِي بَعَثَ فِي الْأُمِّيِّينَ رَسُولًا مِنْهُمْ يَتْلُو عَلَيْهِمْ آيَاتِهِ وَيُزَكِّيهِمْ وَيُعَلِّمُهُمُ

الْكِتَابَ وَالْحِكْمَةَ وَإِنْ كَانُوا مِنْ قَبْلُ لَفِي ضَلَالٍ مُبِينٍ

صَدَقَ اللهُ العَلِيُّ العَظِيم

سورة الجمعة الاية (2)

DECLARATION

I assure you that the work exhibited in this manuscript is my special work and has not been exhibited to other institutions or to get another degree.

Signature:

Name: Fatima Abd-Allatif Tali

Date: / / 2023

ACKNOWLEDGMENTS

First, I would like to thank the almighty ALLAH, all praise be to him for providence. I wish to express my deep gratitude to my supervisors **Lec. Dr Salah M. Salih** and **Asst Prof. Dr Tahssen Ali Hussain** for their valuable help, advice, and encouragement during the project.

Special thanks go to the Dean of Engineering Technical College- Najaf **Asst Prof. Dr Hassanain Ghani Hameed** and special thanks are to the Head of the Department of Mechanical Engineering Techniques of Power **Asst Prof. Dr Adel Abdel Aziz Idan** in the Technical Engineering College /Al-Najaf, Al-Furat Al-Awsat Technical University, for their support and advice.

I would also like to give special thanks to my husband and my family as a whole for their continuous support and understanding. Your prayer for me was what sustained me this far.

Fatima Abd-Alltif Tali

SUPERVISOR CERTIFICATION

We certify that the thesis entitled " **Investigation The Performance of Double-Pass Solar Air Heater with Various Types of Absorption Plates** ", submitted by **Fatima Abd-Allatif Tali**, has been prepared under our supervision at the Department of Mechanical Engineering Techniques of Power, College of Technical Engineering-Najaf, AL-Furat Al-Awsat Technical University, as partial fulfilment of the requirements for the degree of Master of Techniques in Thermal Engineering.

Signature:

Name: Lec. Dr. Salah M. Salih

(Supervisor)

Date: / / 2023

Signature:

Name: Asst Prof. Dr. Tahssen Ali Hussain

(Supervisor)

Date: / / 2023

In view of the available recommendation, we forward this thesis for debate by the examining committee.

Signature:

Name: **Asst Prof. Dr Adel Abdel Aziz Idan**

Head mechanical Eng. Tech of power Dept.

Date: / / 2023

LINGUISTIC CERTIFICATION

This is to certify that this thesis entitled "**Investigation the Performance of Double-Pass Solar Air Heater with Various Types of Absorption Plates**" was reviewed linguistically. Its language was amended to meet the style of the English language.

Signature:

Name:

Date: / / 2023

ABSTRACT

The energy and exergy efficiencies of double-pass solar air heaters (DP-SAH) using three types of absorption plates (flat, trapezoidal and V-groove) are investigated experimentally and numerically. This study aims to improve the maximum energy performance of the SAH by using two paths with different absorption surface geometries to guide the heat transfer fluid with less pressure drops. The effect of varying the mass flow rates (MFR) and constant solar intensity on the energy gain and pressure drops at a steady state is determined for various types of SAHs using an indoor solar simulation.

The experimental study is conducted on a DP-SAH with dimensions (1.284 × 0.320 × 0.084) m and a project area of (0.411) mm^2. Three absorbent plates of aluminum metal with a thickness of 0.7 mm are designed to be the conventional type (flat plate); the second type is trapezoidal plate, and the third type is a V-groove plate. The dimensions of each plate are (1200 × 320) mm.

The aspect ratio (W/H) is set at (10) in two channels to achieve fully turbulent flow (DP-SAH). The minimum inlet and outlet units are based on the ASHARE standard for solar thermal collectors. The system experiments are carried out in the laboratory using six tungsten halogen lamps as a projector simulator.

The numerical study is also conducted using the commercially available COMSOL Multiphysics v5.5 software to solve the two-dimensional governing equations for continuity, Navier Stokes and energy, and the turbulent model equations (κ-ε). The current simulations are carried out under the same boundary conditions to confirm the accuracy of the experimental data with an average error in the thermal efficiency of the flat, trapezoidal and V-groove plate SAHs (± 1.54 %,

± 8.06 %, ±17.75 %), respectively, and the results are acceptable and good. The investigations are carried out at different air mass flow rates (0.6, 1.2, 1.8, and 2.4) kg/min and a constant solar radiation of 825 W/m^2.

The results showed that the air temperature is inversely proportional to the air MFR; it is also noted that the maximum energy efficiency is highly dependent on the air MFR in all models.

In addition, the thermal efficiency of a DP-SAH at a flat, trapezoidal and V-groove absorption plate when conducting experimental in the laboratory ranged between (27.69 – 55.64) %, (45.7 – 72.91) %, and (53.92 – 82.46) %, respectively, under the air MFR ranging from (0.6 – 2.4) kg/min. While the maximum exergy efficiency of a flat, trapezoidal and V-groove absorption plate when conducting experiments in the laboratory ranged between approximately (5.18 – 10.04) %, (9.35 – 16.025) %, and (10.3 – 21.93) %, respectively.

While the thermal efficiency ranges in the numerical analysis for the flat plate is (28.8 – 56.27) %, the trapezoidal plate is (48.94 – 87.8) %, and V-groove plate is (67 – 99) %.

TABLE OF CONTENTS

Nomenclature

Symbol	Description	Unit
A_c	Collector surface area	m^2
A_{cs}	Duct cross-section area	m^2
c_p	Specific heat capacity	KJ/kg. K
C_μ, $C_{1\varepsilon}$, $C_{2\varepsilon}$	Constant in turbulence model	_
D_h	Hydraulic diameter	m
Ex_{dest}	Exergy destruction	W
F_x, F_y	The external (volume) forces	N
h	Heat transfer coefficient	W/m^2. K
H	Height	m
h	Specific enthalpy	J/kg. K
I	Solar radiation	W/m^2
k	Thermal conductivity	W/m. K
L	Length	m
$\dot{m}$	Mass flow rate	kg/s
N	The number of speed points observed at the duct output	
$\bar{p}$	Time-averaged values of pressure	N/m^2
ΔP	Pressure drops through collector	Pa
$\dot{Q}$	Rate of energy	KW
R	Gas constant	J/mol. K
Re	Reynolds number	_
S	Entropy	J/K
T	Temperature	°C
t	Thickness	m
U	Overall heat loss coefficient	W/m^2. K
u, v	Velocity component in x and y directions	m/s
$\bar{u}, \bar{v}$	Average velocity in x and y directions	m/s

Symbol	Description	Unit
$\acute{u}, \acute{v}$	Fluctuation of mean velocities in x and y directions	m/s
V	Total velocity vector	m/s
W	Width	m
$\dot{W}$	Power consumption of fan	KW
x, y	Cartesian coordinates	m

Greek symbols

Symbol	Description	Unit
κ	Kinetic energy of turbulent	_
P_κ	Production	
υ	Kinematic viscosity	m^2/s
υ_e	Effective kinematics viscosity	m^2/s
υ_t	Eddy or turbulent viscosity	m^2/s
Γ_e	Effective diffusion coefficient = $\frac{\upsilon_e}{\sigma_e}$	$N.s/m^2$
Δs	Entropy change	J/K
ϵ	Emissivity	_
η	Thermal efficiency	%
μ	Dynamics viscosity	$N.s/m^2$
μ_T	Eddy viscosity	$N.s/m^2$
ρ	Density of air	Kg/m^3
σ	Stefan-Boltzmann constant	$W/m^2. K^4$
$\sigma_k, \sigma_\varepsilon$	Turbulent Prandtl number for κ, ε	_
$\tau\alpha$	Effective transmittance-absorbance	_
ψ	Specific exergy	J/kg
ε	Dissipation rate of turbulent kinetic	_

Abbreviations

Symbol	Title
ASHRAE	American Society of Heating, Refrigeration and Air Conditioning Engineers.
CFD	Computation fluid dynamics
DP-SAH	Double-pass solar air heater
FP-SAH	Flat plate solar air heater
κ-ε	Two-equations turbulence model
MFR	Mass flow rate
PP-SAH	Parallel-pass solar air heater
RANS	Reynolds-averaged Navier-Stokes
SAH	Solar air heater
SP-SAH	Single-pass solar air heater
TTI	Twisted tape inserts
VC	V-corrugated
VTP	V-groove triple type plate
VARIAC	Variable Alternating Current

Subscript

Symbol	Title
a	Ambient
abs	Absorber
acc	Accumulated
b	Bottom
bg	Backplate
e	Edge
ex	Exergy
f1	First flow

Symbol	Title
f2	Second flow
g	Glass cover
in	Inlet
L	Loss
m	Mean
out	Outlet
p	Plate
r	Radiation
s	Sun
t	Top
w	Wind

Chapter One

Introduction

Chapter One:

Introduction

1.1. General Concept:

Renewable energy is energy derived from natural sources that are renewed. For example, sunlight, wind, hydropower, biomass, and ocean energy are constantly replenished sources. Renewable energy sources are abundant and all around us. On the other hand, fossil fuels - coal, oil, and natural gas - are non-renewable resources that take hundreds of millions of years to form. When fossil fuels are burned to produce energy, they emit harmful greenhouse gases, such as carbon dioxide. Generating renewable energy produces far fewer emissions than burning fossil fuels. A shift from fossil fuels, which currently account for the lion's share of emissions, to renewable energy is key to addressing the climate crisis [1].

Solar energy is the most abundant of all energy sources. The Earth's exposure to solar energy is about 10,000 times greater than the rate at which humanity consumes energy. Solar technologies can provide heat, cooling, natural lighting, electricity, and fuel for various applications. Solar energy technologies convert sunlight into electrical or thermal energy through photovoltaic panels or mirrors that concentrate solar radiation or solar heaters and other applications. Although not all countries are equal in solar energy, a significant contribution to the energy mix from direct solar energy is possible for each country [1].

The achievements in renewable energy are undoubtedly impressive, but there is a long way to go before a full energy transition occurs. Even in the United States of America, where there are many global clean energy giants, renewable energy

accounted for only 12% of national primary energy consumption in 2021, as shown in figure (1.1) [2].

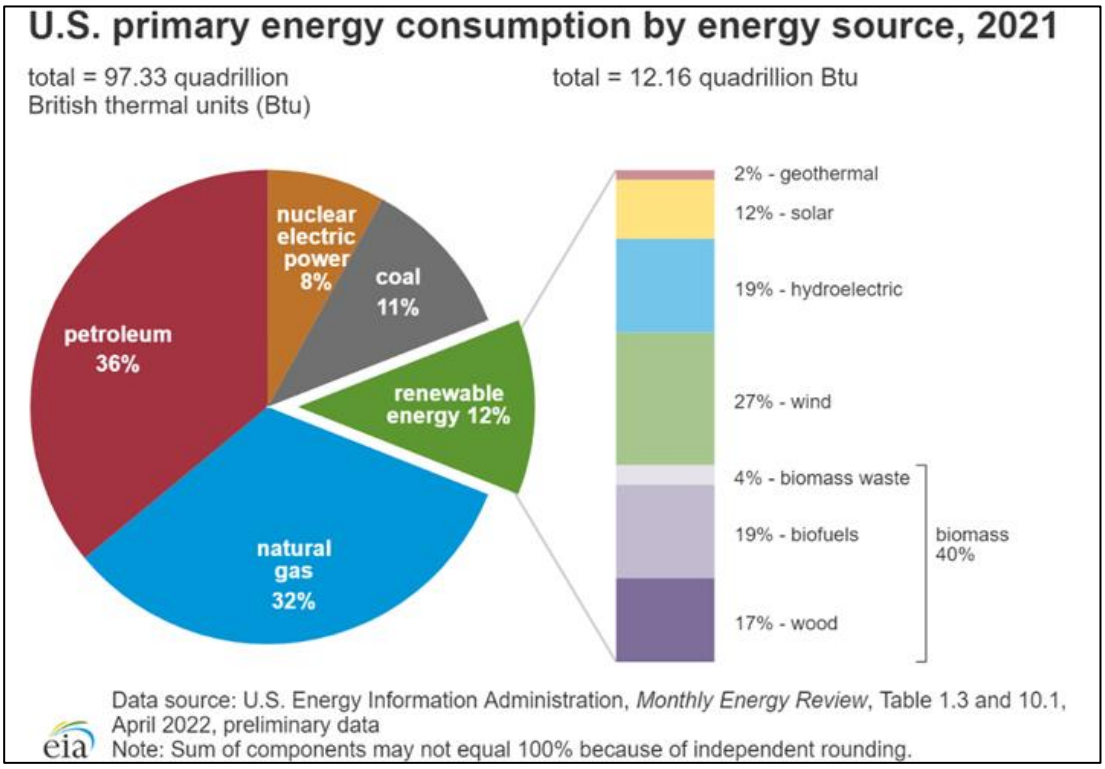

Figure 1. 1: Energy consumption in the United States of America by source, 2021 [2].

Solar energy considers one of Iraq's most important renewable energy sources, as this energy is available permanently and for free. That is due to the geographical location of Iraq, where Iraq is in southwest Asia between latitudes (29-37) north and longitudes (38-48) east, as it discovers near the solar belt, which receives an amount of solar radiation with an average of (6.5-7) kW/hour per square meter. The sunshine period ranges from (2800-3300) hours per year, giving Iraq the necessary qualifications to exploit solar energy [3].

Al-Najaf Al-Ashraf is considered one of the highest cities with a high solar radiation intensity that reaches about (220-980) during the year, where Najaf is

located at latitude 32.01 and longitude 44.32. The coordinates indicate that Najaf enjoys bright days most of the year, about 330 days per year, like the capital, Baghdad. Hence, different solar energy systems can be used in the atmosphere of Najaf [3].

One of the most significant solar thermal energy innovations that helps conserve fossil fuels and lessen environmental pollution is the use of solar air heaters.

As a result, it can be applied economically and practically using the flat plate solar air heater in heat engineering applications (SAH). To generate hot air from collected energy for low-temperature applications (between 20 – 50 °C) that run inefficiently without any thermal energy storage, such as solar drying for agricultural and industrial uses or space heating for buildings and greenhouses, as thoroughly evaluated by the authors. The discrepancy between the need for thermal energy after sundown and the availability of sunlight during the day [4-7].

1.2. Solar Radiation:

Nuclear fusion events take place in the sun's core to produce solar radiation, which releases a significant quantity of potential energy from electromagnetic radiation. A surface's ability to radiate heat is proportional to the fourth power of its temperature in the visible and near-infrared spectrums. The planet will swiftly shine more energy into space as the earth's temperature rises. The sun's surface reaches a temperature of roughly 5500 ◦C [8].

As illustrated in figure (1.2), roughly 51% of the solar energy entering the earth's atmosphere makes it to the surface. The other 49% is reflected in space and absorbed by the environment. Solar energy needs to cut its cost to be more competitive, and it

also needs to be more responsive to market demands. Promoting the use of renewable energy is now a long-term national policy in several nations [8].

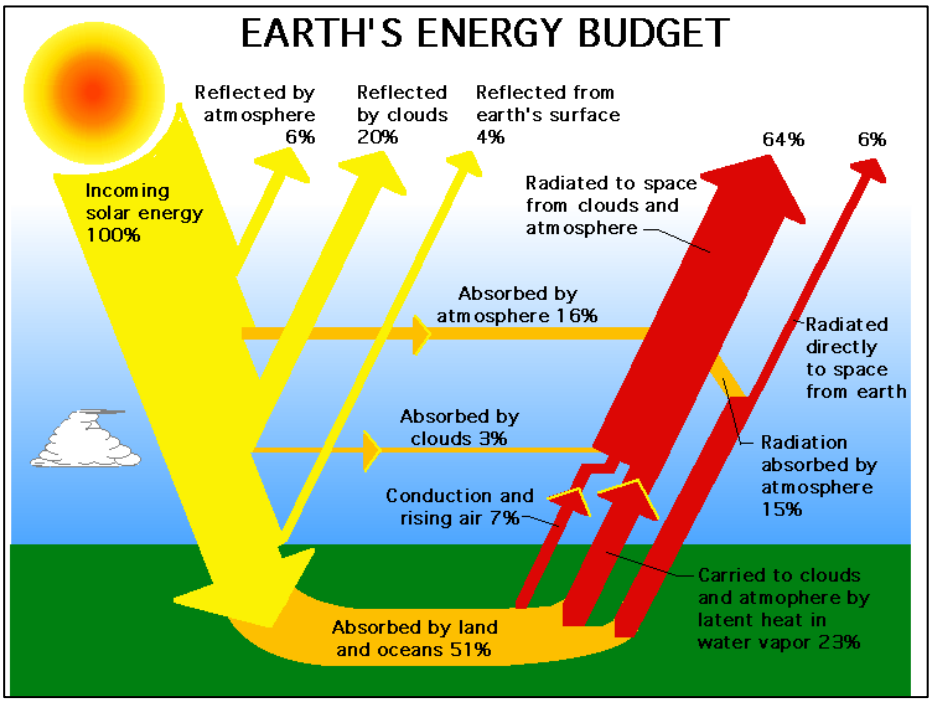

Figure 1. 2: This diagram illustrates how Earth reflects and absorbs solar radiation [8].

1.3.Flat Plate – Solar Air Heaters (SAH):

SAHs are the technology that harnesses solar energy for various thermal system uses. In principle, SAHs consist of an insulating substance, a top cover, and a black absorbent plate.

This chapter discusses various SAH kinds that travel immediately above or below the absorber plate and use air as the working fluid rather than water. Air flows in the space created between the absorbent surface and the cover glass. Solar radiation was directed at the absorbent plate. The air stream's temperature increases through the collector duct's energy absorption. Numerous uses for this hot air exist, including drying crops, room heating, and industrial heating. Due to the following advantages

of SAHs over other solar water heaters (SWHs), there has been an increase in interest in the use of SAHs [9]:

1. Compared to SWHs, SAH technology is safer, cheaper, and easier to maintain and operate.
2. When compared to SWHs, this system has fewer wear and leakage issues.
3. The working fluid (air), which does not freeze, does not pose a threat if it leaks.
4. The pressure rise in this design is minimal.
5. Compared to SWHs, SAHs can produce useful energy at lower solar radiation intensities.

Although it can use less expensive materials to create the SAH. However, the following are the disadvantages of solar air collectors [9]:

1. Compared to SWHs, the working fluid (air) has less thermal conductivity and heat capacity.
2. Heat energy transmission requires greater mass or volumetric fluxes than SWHs because of the lower air density.
3. Planning and installation are needed for this system to utilize less additional energy.
4. A heat storage device is required for solar air heaters to provide usable energy at night.

1.3.1. Types of Solar Air Heaters:

Due to the energy lost to the environment and the poor heat convection coefficient between the airflow and the absorber plate, solar air collectors have poorer thermal efficiency. SAHs can be divided into two primary groups based on the technology

used to create the flat plate absorbent surface. The first category refers to the optimization of solar air collector performance. It should use the black plate to improve the convection area and airflow turbulence. Several techniques, including extended surfaces (fins/obstacles), wire screens used as porous materials, and rough or grooved surfaces, can improve the thermal efficiency of SAHs, as shown in figure (1.3) [10].

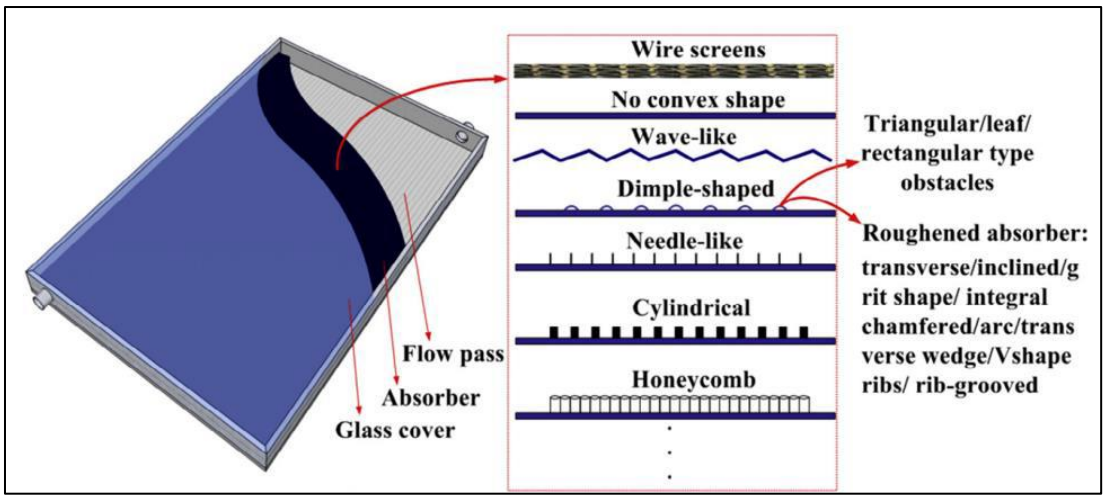

Figure 1. 3: Typical flat plate SAHs with rough components [10].

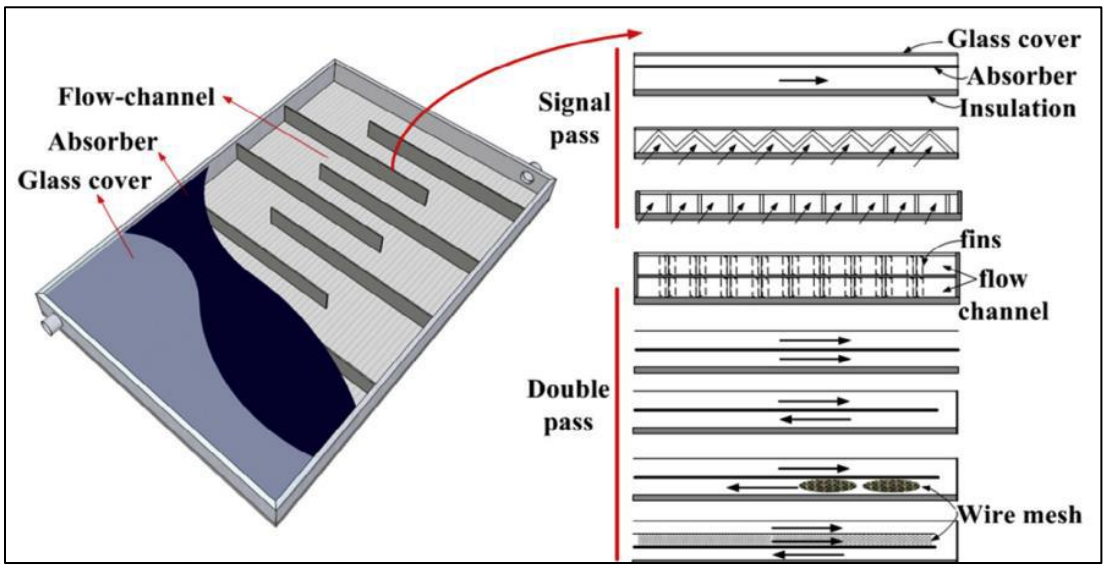

Figure 1. 4: Typical flat plate SAHs with more turbulence [10].

The second group is determined by the number of air passageways, the kind of airflow channel, and the best design to minimize energy loss in the atmosphere, as shown in figure (1.4) [10].

Significantly, the airflow channel model influences the output temperature and the SAH thermal efficiency. As a result, SAHs can be divided into four categories:

a) A above flow SP-SAH.
b) A below flow SP-SAH.
c) A parallel flow DP-SAH.
d) A counter flow DP-SAH, as shown in figure (1.5).

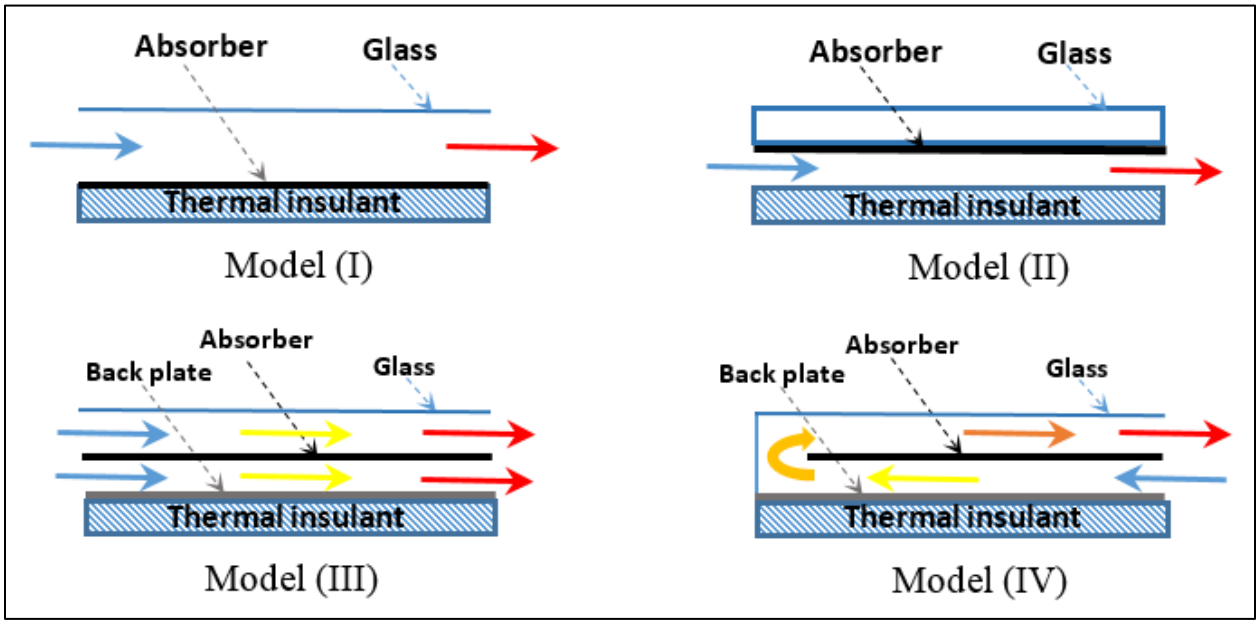

Figure 1. 5: Different types of Airflow pass in FP-SAHs: (I) a above flow SP-SAH, (II) a below flow SP-SAH, (III) a parallel flow DP-SAH, and (IV) a counter flow DP-SAH.

In the two single-pass SAH (SP-SAH) models, air moves in one direction (single pass) from the air input to the duct outlet, either above or below the suction surface.

As opposed to the other two double-passes SAH types, which allow for parallel or reversed airflow, respectively. SAH double-pass flat plates typically include the following several fundamental parts, as shown in figure (1.6) [11]:

1. ***Pellucid cover***: high transmittance and low absorption that transfers radiation to the absorption material, with an air gap to separate the surrounding environment from the heated air to reduce energy losses.
2. ***An absorbent plate*** has high thermal conductivity and a high ability to absorb solar radiation, such as (copper, aluminum, galvanized iron, etc.).
3. ***A backplate:*** with a high heat conductivity is fastened to the collector's bottom wall.
4. ***Container box:*** to hold and attach the solar collector structure's parts.
5. ***Thermal insulators:*** to prevent energy radiation from escaping into the environment, the bottom and edge walls of the collector are insulated with low-conductivity materials like wood, glass wool, and foam.

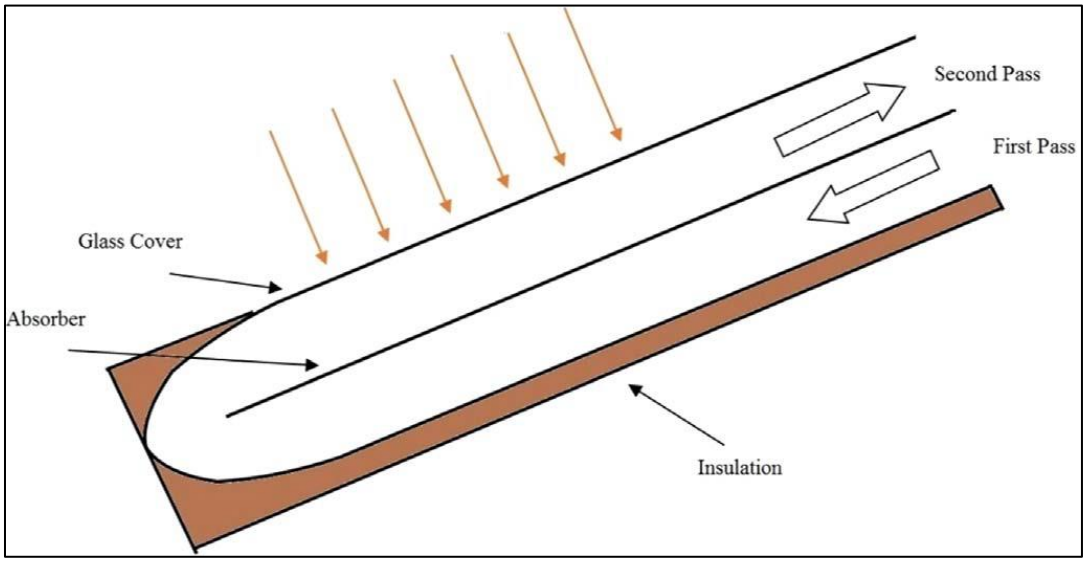

Figure 1. 6: Flat plate double-pass solar air heater [6].

1.3.2. Solar Air Heaters Applications:

In numerous thermal engineering applications, solar air collectors have been widely used. The absorbent plate absorbs solar radiation, and the additional energy is delivered to the air traveling through the channel to increase the air temperature. Consequently, one can apply this heater air in a variety of ways, including [9]:

1. ***Use in the home:***
    - ***a.*** Heating for residential, commercial, and workshop spaces.
2. ***Agriculture-related uses:***
    - ***a.*** Solar agricultural drying, such as paddy grains, fruit, etc. that makes the crop dehydrating with solar radiation can save energy while protecting it from vermin, damage, etc.
    - ***b.*** Space heating for glasshouses, warehouses, and livestock ranches.
3. ***Industrial heating techniques:***
    - ***a.*** Preheating air for burning, which includes a wide range of procedures.
    - ***b.*** Drying things like food, paper, wood, charcoal, etc., especially brown coal drying, is important for power plants.
    - ***c.*** Heating of areas in factories, warehouses, etc.

1.4.Exergy in solar air heater:

In thermodynamics, a system's exergy is defined as the most productive amount of work that may be done to bring about thermal equilibrium. In other words, as the system approaches equilibrium, exergy—the maximal capacity of energy to perform useful work—increases, but irreversibility increases entropy at the expense of exergy. Exergy is the difference between the system's total energy and any energy unavailable due to losses, for example. Zero exergy in a system that is in perfect balance with its surroundings. For the analysis, design, and improvement of energy

(and other) systems, exergy analysis uses the conservation of the second law of thermodynamics. Due to its ability to pinpoint the location, nature, and scope of wastes and losses, this method can be used to find efficient energy utilization. Exergy analysis may show whether an energy system's design is effective and how its effectiveness could be increased by eliminating inefficiencies [12].

Energy efficiency refers to the first rule of thermodynamics; in contrast, exergy efficiency refers to the second law, which is typically lower than energy efficiency because the irreversible process destroys some input energy. Exergy is the energy wasted during an irreversible process or system's entropy production. This energy loss is calculated by adding entropy to the steady-state temperature of the immediate environment. The proportion of heat a substance absorbs to temperature is known as entropy. While exergy is being accumulated, energy is awakened [13].

1.5. Objectives of the Work:

The present work focuses on improving the efficiency of a double-pass solar air heater by increasing the absorption plate area and turbulence of the airflow by conducting practical experiments and numerical tests. The main objectives of this study are:

1. Fabricating three different absorbent plate modules: a flat plate, trapezoidal, and V-groove absorber plates, as shown in figure (1.7).
2. Investigating the effect of air MFR on outlet temperature, pressure drop, and energy/exergy efficiencies through the DP-SAH, where the fan operates at four speeds ranging from (0.9 – 3.4) m/sec, which achieves turbulent flow of the Reynolds number between (4300 – 16200) and a MFR ranging between (0.6 – 2.4) kg/min (The speed of 0.9 m/sec achieves turbulent flow, whereas at less than this

speed, the flow is laminar. When the velocity is higher than 3.4 m/sec, achieving a decrease in efficiency is possible after reaching its highest value).

3. Studying the thermal performance analysis results, comparing three different types of absorber plates used in SAH, as well as comparing the experimental and theoretical results with each other.

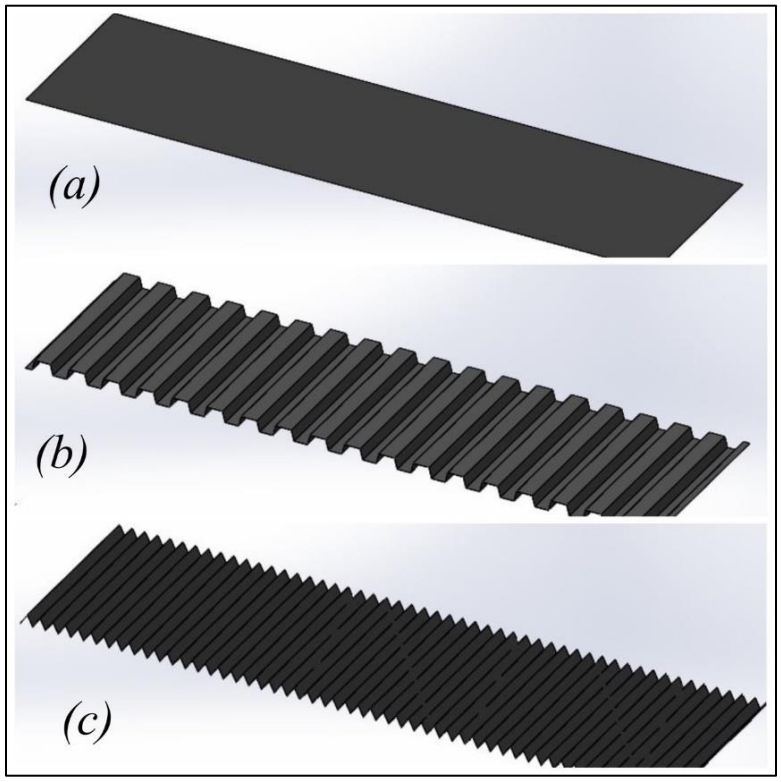

Figure 1. 7: Picture of absorber plates drawn by Solidworks.

Chapter Two

Literature Review

Chapter Two

Literature Review

2.1.Introduction:

This chapter is centered on previous studies that improved the heat transfer coefficient between the absorption plate and the airflow. Using artificial roughness to create a disturbance inflow is one technique to achieve a substantial increase in heat transfer. Various types of rib, grooves, baffles, fins, corrugated, and other disturbance generators have been examined by multiple researchers.

2.2.Flat plate:

Adel A. Hegazy (2000) [14] examined the effect of the absorption plate's shape on the accumulator's thermal-hydraulic performance for three standard airflow models (above, below, and on both sides of the absorption plate). Three forms of absorbent plates were used: the traditional rectangular, parabolic trapezoidal, and concave with the same surface area. Comparisons indicate that variable-width collectors exhibit performance behavior similar to that of the corresponding fixed-width models but are accompanied by a marginal decrease in air temperature rise and collection efficiency along with a slight increase in fan power consumption. Thus, the comparisons support the idea of using variable-width collectors in solar air heating applications, especially those with design limitations on investment costs and the space available for installing the air collectors.

Al-Jethelah et al. (2019) [15] studied the effect of the height of the air space between the absorbent plate and the glass cover on the air temperature and the mass flow rate at the outlet of the solar air heater experimentally and numerically. They manufactured three identical solar air heaters, each with a different air space, and

the heights ranged between (3-9) cm. The experiments were carried out in Tikrit-Iraq. They also studied the results numerically using the COMSOL Multiphysics ® software. The results showed that the highest outside temperature was obtained with the narrowest area, especially 88.95 °C at 3 cm.

2.3.Trapezoidal Plate:

Lakshmi et al. (2017) [16], carried out a practical experiment on a trapezoidal absorber plate along with sensible heat storage material, and analyzed the energy and exergy, where the experiments were conducted in Odisha, India. FP-SAH and the trapezoidal plate have a rate daily thermal efficiency of 8.5 percent and 12.2 percent, whereas the thermal efficiency of trapezoidal absorbers with sensible heat storage material was 36.6 percent. With a trapezoidal absorber and a material that stores sensible heat, the best energy efficiency was 12.56 percent.

Harde et al. (2018) [17] designed and tested a solar air collector with jet impingement on the trapezoidal absorption plate and compared the results with a conventional solar air heater. The jet generated a turbulent current, producing a high outside air temperature. The trapezoidal absorption plate also increased the air turbulence rate and the absorption surface area, thus increasing the heat exchange between the air and the plate. The results showed that this change enhanced the heat transfer rate by 1.47, and heat absorbed was 900 W.

Diana et al. (2019) [18], used Computational Fluid Dynamics, this study examined airflow and heat transport inside a trapezoidal solar air heater channel. The Re varies between (10600 – 12700). The heat flux uniformity on the top and tilt surfaces is between (800 – 1000) W/m^2. This paper's simulation uses the finite volume method, and the algorithm is simple. The results showed that the highest outside air temperature is 322.2 K at Re is 10600, and the lowest is 318.3 K at Re is

12700. That means the numerical study by the Ansys program showed that the outside air temperature is the highest for all solar radiation values when the Reynolds number is low.

Darici and Kilic (2020) [19] experimentally tested the thermal performance of two SAH designed with trapezoidal and flat absorber plates as shown in figure (2.1) under Konya/Turkey weather conditions. Three separate air MFRs of (0.022, 0.033, and 0.044) kg/s were utilized in the tests and the amount of solar radiation varies between (400 – 1026) W/m^2 during the day. These results are compared with an FP-SAH. The differential between SAH's input and output air temperatures increased. Compared to an FP-SAH with an air MFR of 0.022 kg/s, the trapezoidal plate SAH had a maximum temperature increase of 9 °C.

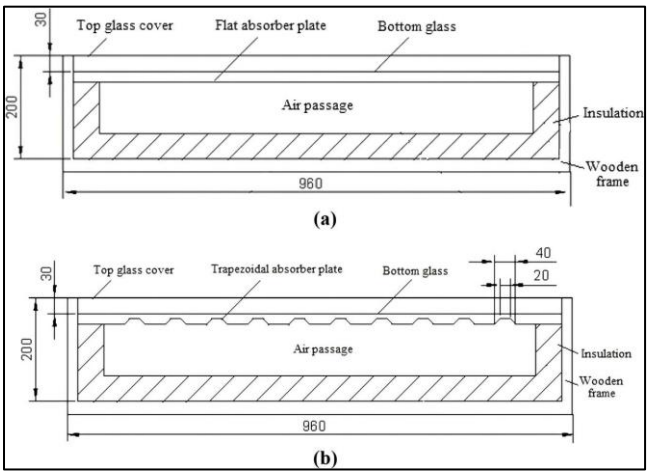

Figure 2. 1: Section views SAH (a) Flat plate (b) trapezoidal plate [19].

Xiao et al. (2020) [20] verified the flow properties of the mechanism of enhancing heat transfer, thermal-hydraulic performance and energy efficiency in solar air heaters with inclined trapezoidal vortex generator plates (ITVGs) as shown in figure (2.2) by conducting a numerical simulation. The main goal was to enhance the heat transfer performance of the solar air heater by generating multiple

longitudinal swirls flow. The amount of solar radiation reached 1000 W/m^2 and Reynolds number varying from (6000 – 18000). Compared to the flat plate, energy and exergy efficiencies have been improved to 24% and 31 %.

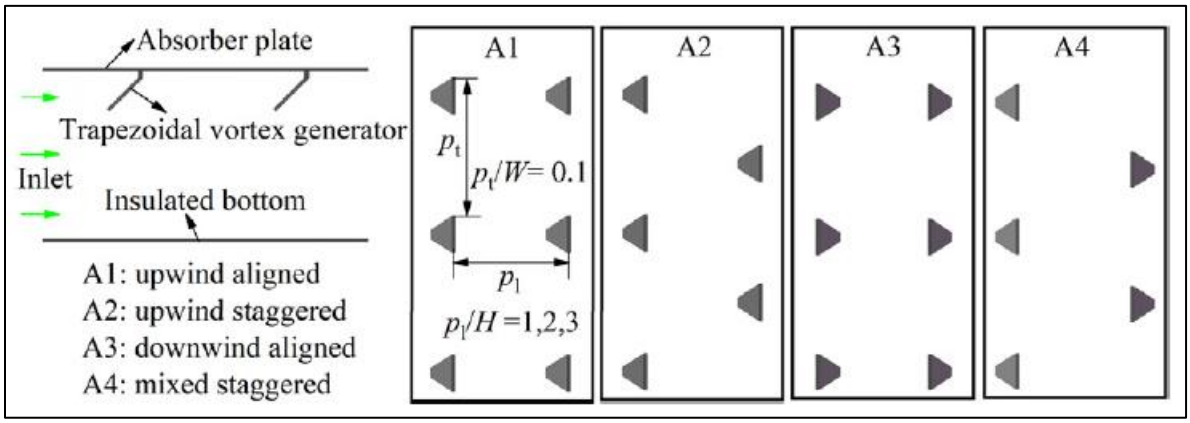

Figure 2. 2: Different types of arrangements of ITVGs in the SAH [20].

Reddy et al. (2021) [21] experimentally investigated the thermal performance of two solar air collectors with absorber plates: reverse trapezoidal and cross-corrugated trapezoidal, as shown in figure (2.3). Experiments are carried out under the climatic conditions of Assam in India. The values of MFR range between (0.00039 - 0.0156) kg/sec, inclination angles (15°, 30°, and 45°), the solar radiation values range between (290 – 965) W/m² and the ambient air temperature between (14.28 – 33.3) °C. The maximum temperature rises values of the first and second types of 74.1 and 77.9 °C, respectively. The results also showed the maximum thermal efficiency of 30.3 % and 39.4 % for the first and second types, respectively, for the inclination angle of 45° and the air MFR of 0.0156 kg/s, while the exergy efficiency of 26.98 % and 36.19 % for the first and second types, respectively.

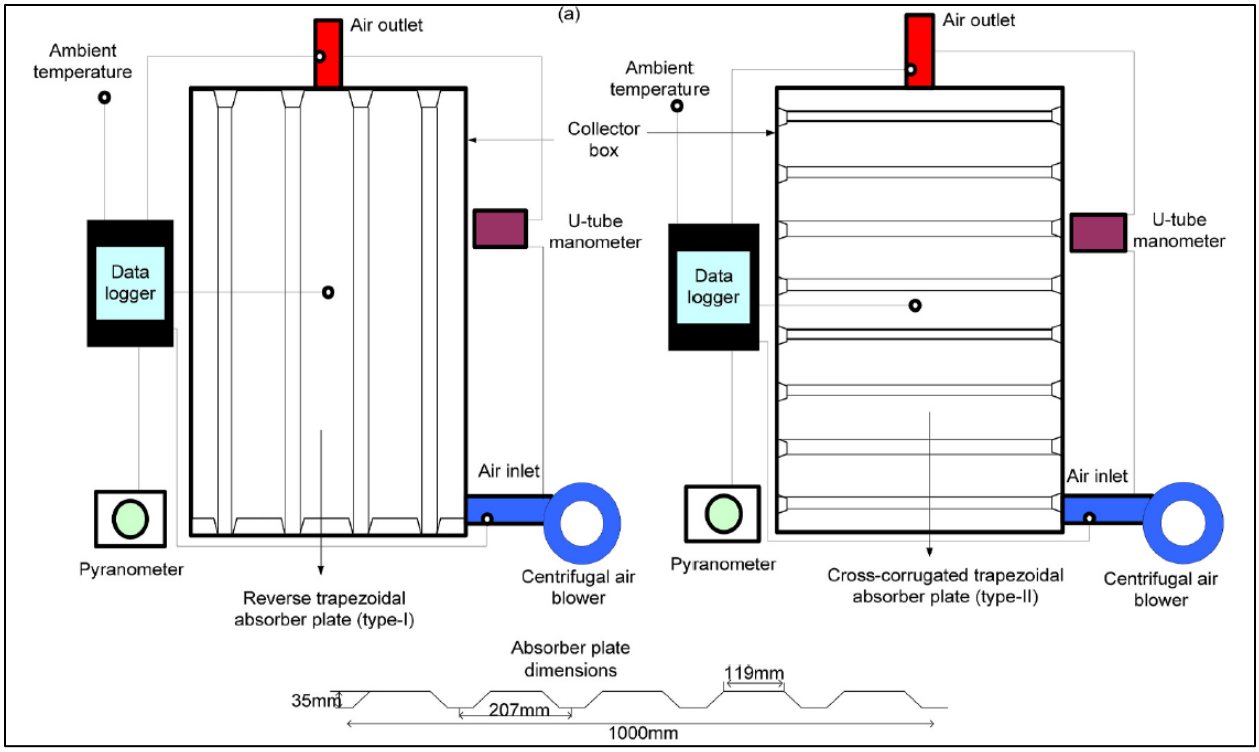

Figure 2. 3: Two types of solar air collectors [21].

Four different absorption plates are designed by **Alic et al. (2021) [22]** to evaluated the environmental impacts of the solar air heater as shown in figure (2.4), whereby their thermal performance and energy efficiency are determined. The performance of flat, Das model, Das model rev., and Z-type plates under climatic conditions in the province of Elazig in Turkey are investigated, and numerical analysis is performed using ANSYS software in 3D format. The results showed the thermal efficiency of the flat, Das model, Das model rev., and Z-type plates of 26, 60, 70, and 78%, respectively. The highest exergy input values are 47.7 W for Z-type, and the lowest exergy input values are 11.2 for a flat plate.

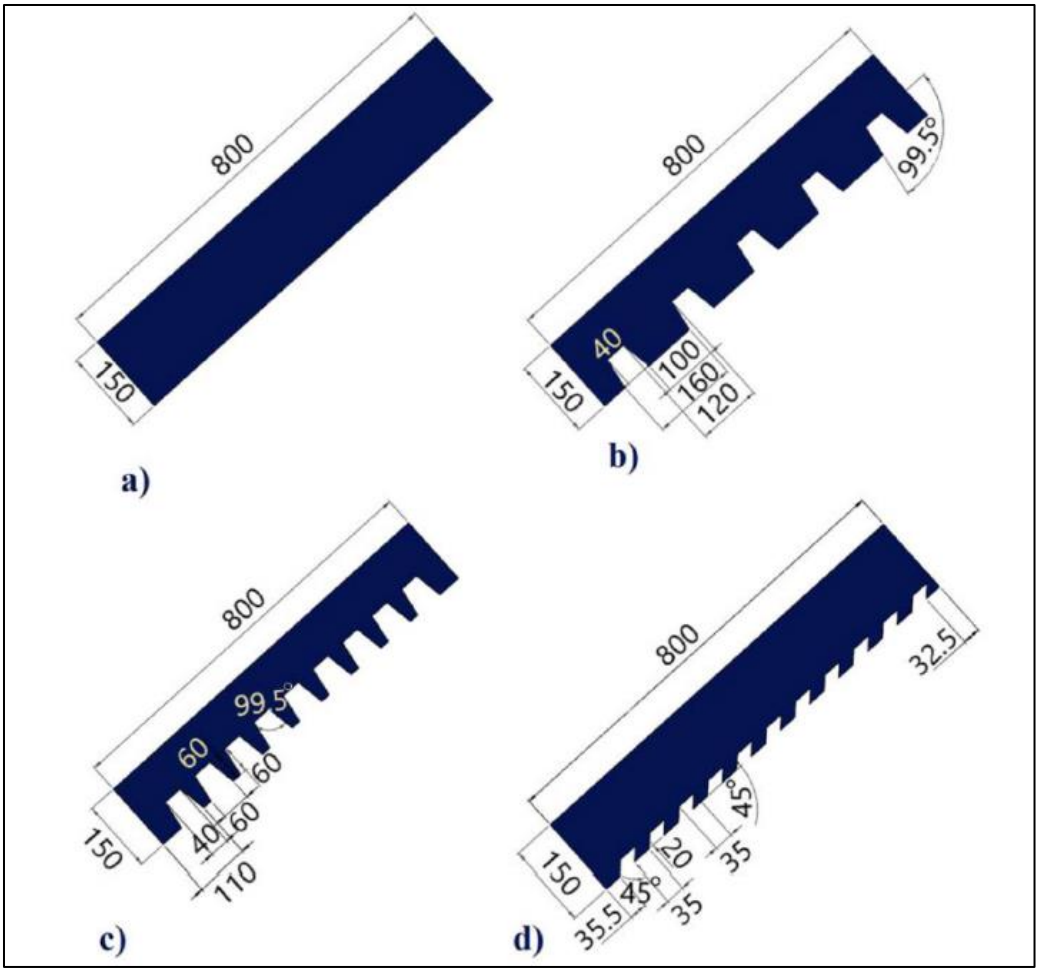

Figure 2. 4: Different types of absorption plates (all dimension in mm) [22].

2.4.V- Groove or V- Corrugated Plate:

Joudi and Mohammed (1986) [23] studied the performance of a V-corrugated plate solar air heater experimentally under the weather conditions of Basra. The collector is tilted at 20 degrees in the summer and 40 degrees in the winter to maximize the heat collection during the solar radiation period. The MFR per unit collector area of air values ranges between (0.016-0.0385) kg/s.m². The results showed that the thermal efficiency at an air MFR of 0.016 kg/s.m^2 was 48% experimentally and 41% analytically. The thermal efficiency at an air MFR of 0.0348 kg/m^2 was 56% experimentally and 50% analytically. The experimental

thermal efficiency values were higher by (6-7.5) % than the analytical thermal efficiency.

Kabeel and Mecarik (1998) [24] studied the effect of changing the absorber's shape factor on the collector's performance. They created a theoretical model for two types of collectors, triangular (V-corrugated) and longitudinal fins, considering the absorber's shape factor, as shown in figure (2.5). The heat transfer between airflow and absorber plate in the heater and the pressure drop increase with the increase of the triangular angle of the triangular collector. The optimal angle of the collector is in the range of 50-60 degrees. The efficiency of the triangular collector was higher than that of the longitudinal fins' collector.

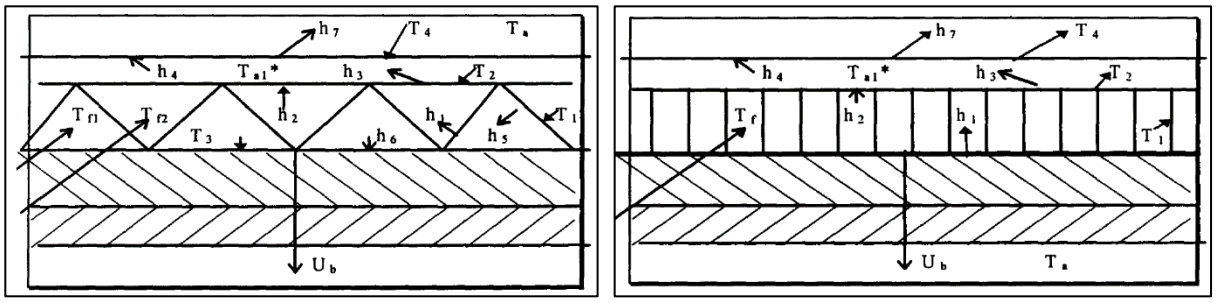

Figure 2. 5: Triangular and longitudinal fins solar air collector [24].

The flat and v-corrugated plate of DP-SAH shown in figure (2.6) was examined theoretically and experimentally by **El-Sebaii et al. (2011) [25]** in Tanta weather conditions. The v-corrugated plate DP-SAH was 11-14 percent more efficient than the flat plate DP-SAH. According to the data, the highest thermal-hydraulic efficiency of the v-corrugated and flat plate SAH was attained when the MFR of air is 0.02 kg/s.

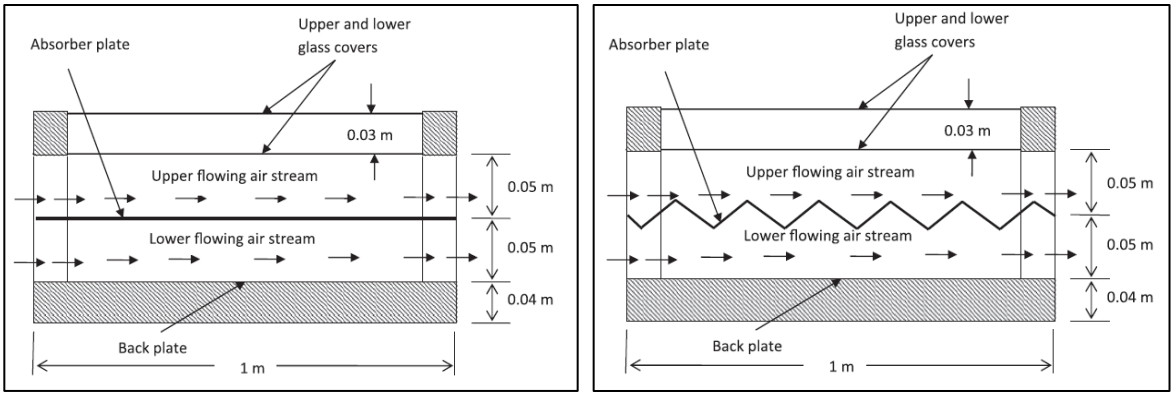

Figure 2. 6: Double-pass solar air heater with flat and V-corrugated plates [25].

Through a parametric investigation, **Hedayatizadeh et al. (2012) [26]**, focused on approaches to increase the supply of exergy by a v-corrugated SAH as shown in figure (2.7). The effect of the collector's AR, input air temperature, MFR per collector area, and other factors are investigated. According to the energy output assessment criterion, it was strongly prescribed to have a high aspect ratio, low height of triangular duct, and MFR, as well as to keep the input air temperature as low as expected. The exergy output for MFR was determined by the distinction between the values of the energy and entropy-generated terms.

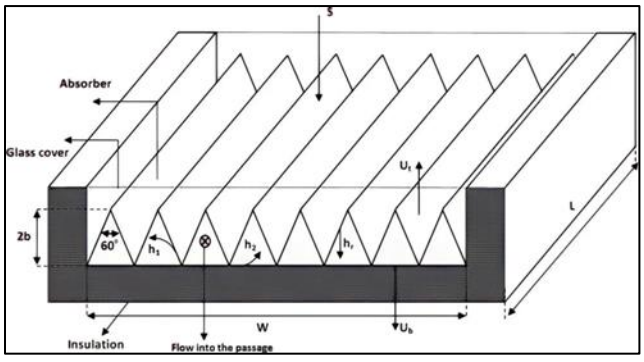

Figure 2. 7: Front view of the VC-SAH [26].

Hedayatizadeh et al. (2016) [27] analyzed the double-pass solar air heater and V-corrugated absorbent plate and determined the amount of exergy loss using the MATLAB program. Through numerical simulations, it was concluded that the maximum exergy efficiency was 6.27 % when using the best-corrugated height of 0.0122, the best heater area of 1.79 m^2, and a MFR of air of 0.005 kg/s for double-pass solar air heater.

Ho et al. (2016) [28] investigated the performance of a double-pass V-corrugated solar air heater with external recirculation experimentally and theoretically. The operating conditions are solar radiation of (830 – 1100) W/m^2 and MFR of (0.0107, 0.0161, and 0.0214) kg/s. A comparison was made between this heater and a flat plate solar air heater to find the efficiency difference between the two collectors. The improvement of the heat transfer efficiency of a V-corrugated solar air heater was greater than that of a flat plate. Collector thermal efficiency improvements increased with increased recirculation ratio but with decreased air MFR.

Sharma and Saha (2017) [29] conducted an analytical study of the thermal and hydraulic performance of three types of solar air heaters, one of which is the conventional solar air heater (type A). The other two are double pass with flat absorption (type B) and corrugated absorption plates (type C). The C++ software estimated the air outlet temperature to evaluate the thermal and hydraulic efficiency by numerically solving the governing equations. The systems and operating parameters are MFR of (0.014 – 0.083) kg/s, solar radiation of 1000 W/m^2, and ambient temperature of 30 °C. The results showed that double-flow solar air heaters had higher efficiency than conventional solar air heaters by (54.27 – 163.32) %. However, the thermal efficiency of a double-flow corrugated absorber solar air heater is upper of a double-flow flat plate solar air heater. The maximum value of

air temperature rise is 17.2 °C of type A, 38 °C of type B, and 45.3 °C of type C at MFR of 0.014 kg/sec.

Ho et al. (2017) [30], the effect of recycling on DP-SAH by welding the V-corrugated absorber was studied experimentally and theoretically. Recycling DP-VC-SAH was technologically and economically viable compared to wire mesh-packed and flat plate SAH. When the recycling ratio increased while the air MFR decreased, collector performance improves, and device performance improved when the intake air flows first through the bottom channel (flow pattern A) rather than the upper channel (flow pattern B). The best recycle ratio was R=0.5 from both a technological and an economic viewpoint, requiring the least compensation for increased hydraulic energy lost.

Omer et al. (2020) [31] aim to look at several design factors for the V-corrugated absorber plate, displayed in figure (2.8), to improve the flat plate SAH's thermal performance. For various design parameters, such as V-groove apex angle, absorber plate height, and v-groove triangular channels form, the analysis was carried out numerically by CFD techniques. The simulation results and methodologies were compared to experimental data from the literature and found to be 0.66 percent in agreement, and thermal efficiency was enhanced by 29%.

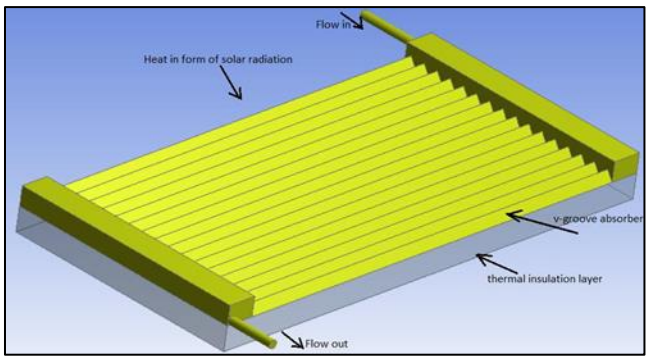

Figure 2. 8: Computational domain of the Study [31].

Under the same climatic conditions, **Tuncer et al. (2020) [32]**, a v-groove type SAH shown in figure (2.9), was created to PP-SAH and DP-SAHs. Also, CFD simulations of SAHs were carried out to discuss the heat and flow conduct within the systems. The studies were conducted in February and June at MFR of 0.015, 0.013, and 0.011 kg/s to assess the performance of SAHs in varied climatic circumstances in Burdur, Turkey. The yearly average thermal efficiency for VTP-SAH, PP-SAH, and DP-SAH was 70.91-78.18, 54-60.29, and 61.86-66.95 percent, respectively, according to the results. In all experiments, the max immediate thermal efficiency was 90.65% at the highest MFR in VTP-SAH in February.

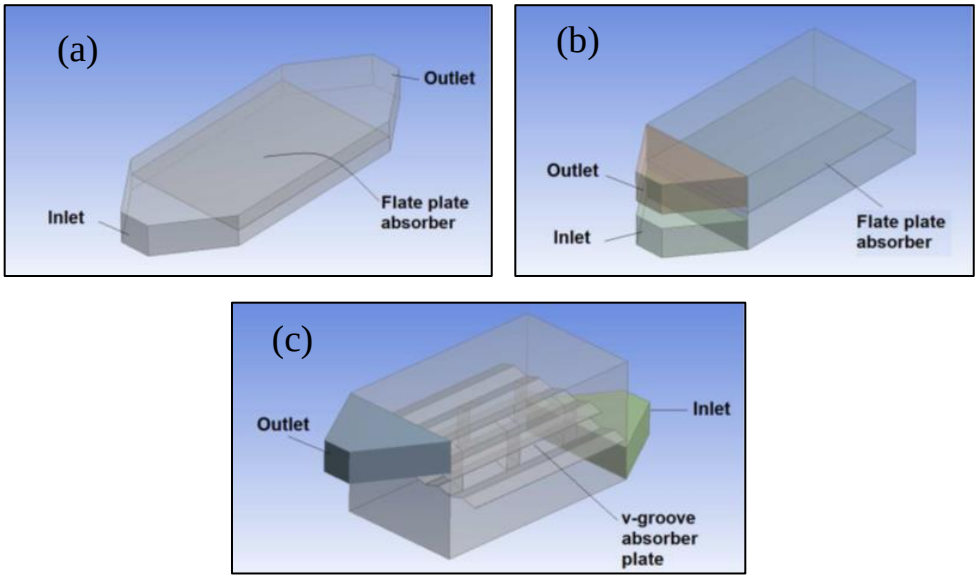

Figure 2. 9: SAH geometries [32].

.

Farhan et al. (2021) [33] studied the exergy and energy analysis of a V-corrugated SAH combined with twisted tape inserts (TTI). Their work was explored analytically and numerically, as shown in figure (2.10). As the twisted tape ratio (Y) reduced, the thermo-hydraulic efficiency of VC-SAH-TTI first increased to a certain value of Re to obtain the gain, then falls. The recommended channel number for the maximum thermo-hydraulic efficiency when using the TTI is N=5. Compared to the

VC-SAH without TTI, the maximum thermo-hydraulic and thermal efficiencies of the VC-SAH-TTI are 17% and 17.5%, respectively.

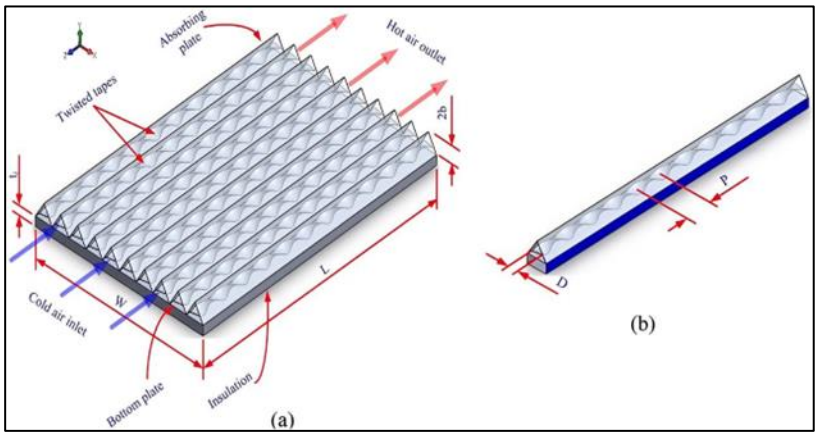

Figure 2. 10: Schematic illustration of (a) VC-SAH-TTI elements. (b) Single section including TTI [33].

Hassan et al. (2021) [34] presented an experimental study on a double-pass solar air heater with a flat plate having V-corrugated (type I) and corrugated-perforated (type II), as shown in figure (2.11), on the roof of the mechanical power lab, Assiut University, Egypt. The study is conducted in four values of air MFR; (a) all the air mass flow upper the absorption plate and then passes down it (double-pass condition), (b) two-thirds of the air mass flow upper the absorption plate and then it is mixed with the rest of air mass to pass down the absorption, (c) as the previous case but third of the air mass flow upper the absorption plate, and (d) all the air mass flow only down the absorption plate (single-pass), as shown in figure (2.12). The results showed that the air temperature rise was higher in DP compared with the other flow ratios for three types of absorption plates, where the temperature rise was for the flat plate 5.51 °C, type I 6.76 °C, and type II 6.85 °C.

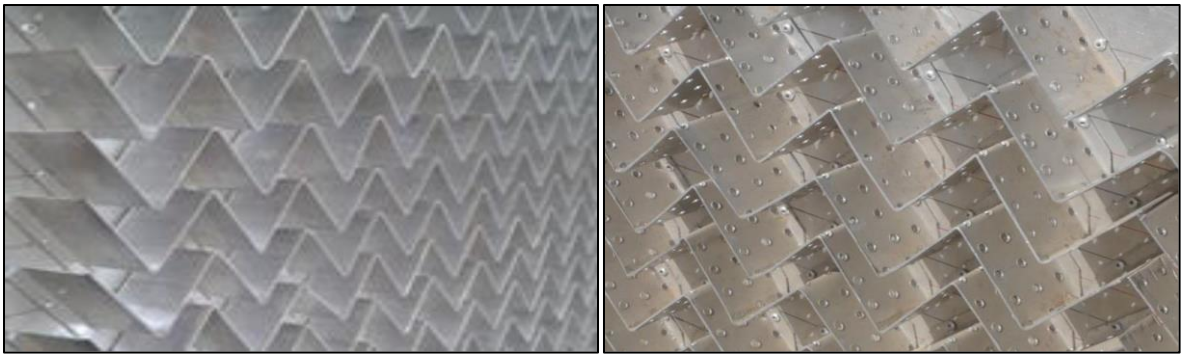

Figure 2. 11: (a) V-Corrugated absorber plate, (b) V-Corrugated perforated absorber plate [34].

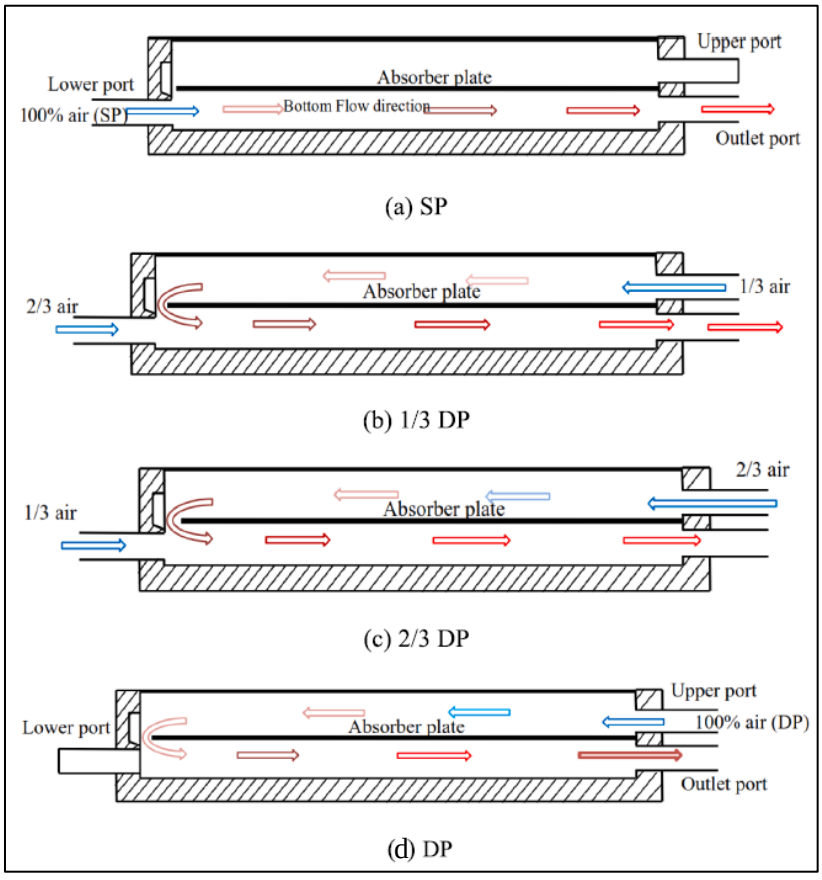

Figure 2. 12: Different types of SAH [34].

2.5.Compared Between Two Type of Plate or More:

Metwally et al. (1997) [35] presented the results of the experimental research and performance analysis of the corrugated channel solar collector. The results are compared with five other designs flow above the absorber plate, flow below the absorber plate, flow above and below the absorber plate, flow parallel to staggered V-folded absorber plate, flow through multi-layers mesh screens, and flow through the corrugated duct. The experiments are conducted under the climatic conditions of Cairo for a flow range of (0.01 – 0.1) kg/s.m^2 and a radiation intensity ranging from (650 – 950) W/m^2. The highest outside air temperature was achieved in the corrugated collector, while the lowest temperature is achieved in the conventional collector. The results showed that the efficiency of the corrugated collector increased by (15-43) % compared to the traditional design (flow below flat absorber).

Karim and Hawlader (2006) [36] conducted a detailed analytical and experimental study to evaluate the thermal performance of single and double passages of solar air collectors under the meteorological conditions of Singapore. Flat, finned, and V-groove plates, , as shown in figure (2.13) are tested and compared under various operating conditions. The MFR of (0.0154 - 0.056) kg/s.m^2. The results showed that the flat plate collector was the least effective, and the v-corrugated collector was the most effective. The v-corrugated collector is 10-15% and 5-11% more efficient than flat plate collectors in single-pass and double-pass modes, respectively, according to the results.

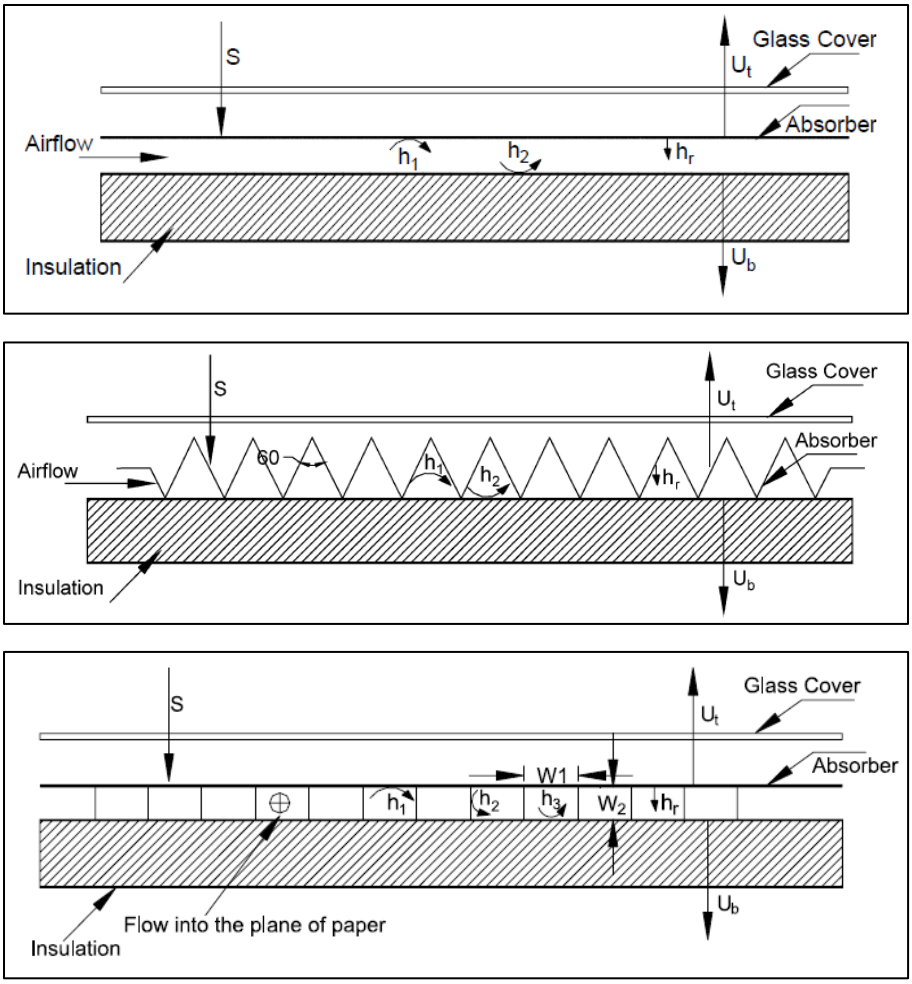

Figure 2. 13: flat, V-groove, finned solar air collector [36].

Huseyin Benli (2013) [37] analyzed the performance and energy of five types of solar air collectors. The experimental analysis included the first and second thermodynamics laws for all collectors. This study compared the experimental results of the following types: corrugated, trapeze, reverse corrugated, reverse trapeze, and flat plate, as shown in figure (2.14). Thermal efficiency range between (25 – 55) %, (22 – 46) %, (20 – 42) %, (15 – 28) %, and (7 – 17) %, respectively. The collectors' efficiency increased approximately 3.5-fold in type one, 2.75-fold in type two, 2.25-fold in type three, and 40% in type four compared to type five. Due

to improved heat transmission to the airflow, the collector's efficiency rises as the MFR increases. The efficiency of air collectors is affected by the collector's surface geometry and the length of the airflow line.

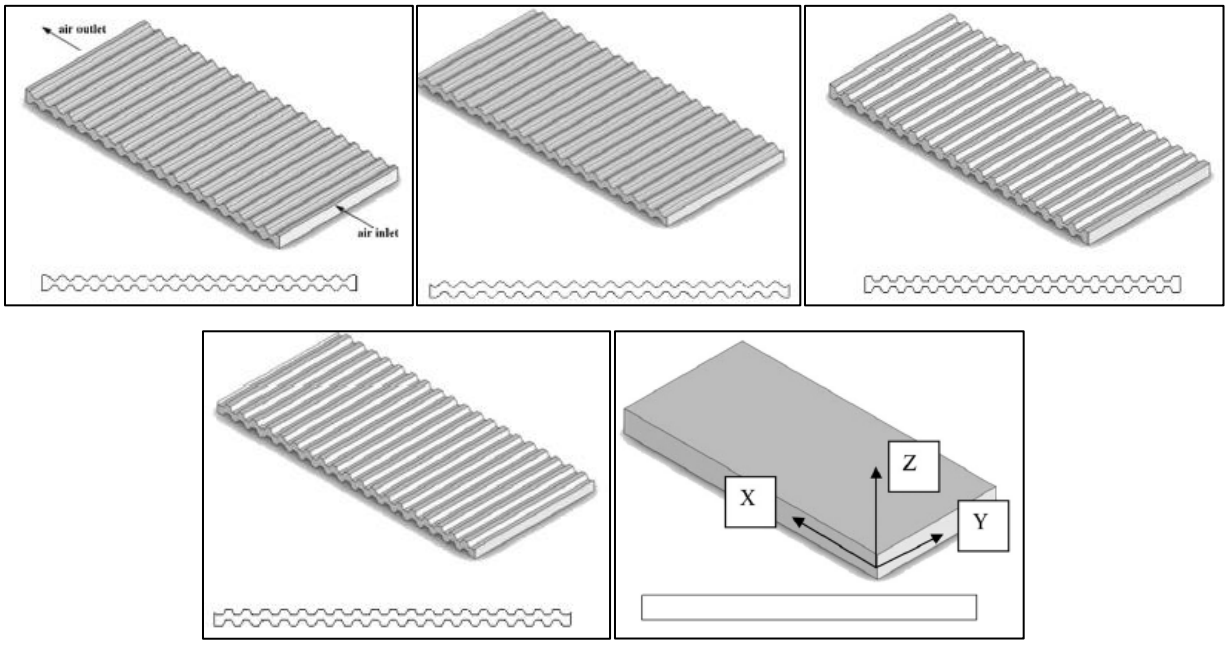

Figure 2. 14: different types of absorption plates [37].

Handoyo et al. (2014) [38] conducted an experimental study on the solar air heater after combining two types of modified absorption plates. They combined a V-corrugated absorber plate and obstacles bent vertically as shown in figure (2.15), starting from 0° to 80° with an interval of 10° on its bottom plate. The study is conducted indoors under three different values of solar radiation intensity (430, 573, and 716) W/m^2 and five values of the Reynolds number (1447, 2895, 4342, 5790, and 7237). When the obstacles are bent 30° instead of 0◦, the air temperature increase, the efficiency of 5.3 percent is reduced, and the pressure drop is 17.2 percent lower.

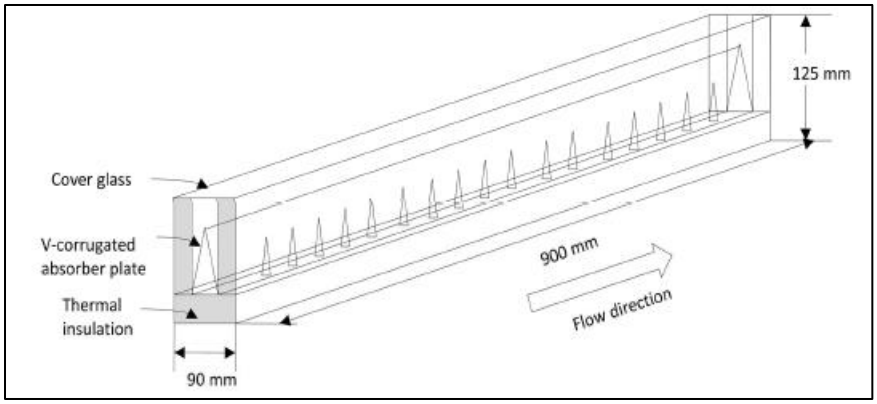

Figure 2. 15: Isometric of V-corrugated absorber plate and obstacles bent vertically [38].

An attempt was made to improve the energy and exergy performance of the solar air heater by **Velmurugan and Kalaivanan (2016) [39]** through the use of different types of absorbent plates. A double-pass solar air heater is studied with V-corrugated wire mesh with longitudinal fins (A), a finned plate with longitudinal fins (B), roughened plate with longitudinal fins (C), and a single-pass solar air heater with a conventional flat plate (D) under steady-state conditions and an indoor solar simulator. Two independent groups of experiments are conducted, the first group at constant solar radiation 600 W/m^2 and variable MFR of air ranging between (0.01-0.04) kg/sec, the second group of experiments at constant MFR of air (0.04) kg/sec and variable solar intensity ranging between (500-600) W/m^2. The results showed that the temperature rise decreases with the increase in the air MFR and increases with the increase in the intensity of solar radiation, as it reaches 26.28 °C at MFR of 0.01 kg/sec and I = 600 W/m^2 for the type A. Energy efficiency increases with increasing air MFR, reaching 82.29 % at an MFR of 0.04 kg/sec and I=600W/m^2 for type A. The exergy gain decreases with the increase in the air MFR, reaching 63.15 W at an MFR of 0.01 kg/sec and I = 600 W/m^2 for type A.

Abed et al. (2017) [40] developed mathematical models to evaluate the dynamic behavior of two solar air collectors. The first type was equipped with a V-porous absorbent plate, and the second was a U-corrugated plate, as shown in figure (2.16). They conducted tests in Bucharest, where he found that the V-porous absorbent plate collector has higher efficiency than the U-corrugated plate collector. Based on the relative root, the average error was around 7.75 percent for the V-corrugated porous absorber and 10.55 percent for the U-corrugated absorber.

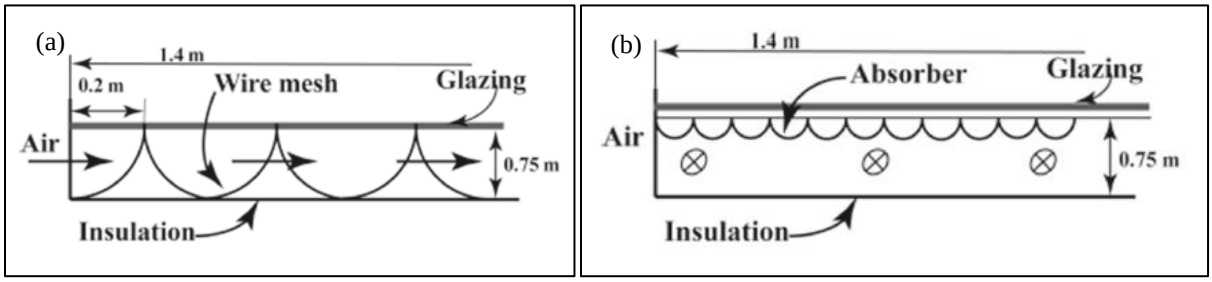

Figure 2. 16: (a) V-porous absorber plate (b) U-corrugated absorber plate *[40]*.

Li et al. (2017) [41] introduced the performance analysis of four types of solar air collectors: flat, sinusoidal corrugated, protrusion, and sinusoidal corrugated and protrusion plates, as shown in figure (2.17). The results showed that the collector's efficiency increased with the increase in the MFR of the fluid. The thermal efficiency of the third type was the highest among the four types under the same mass flow. The collector's efficiency increased by about 1.08 times in the second type, 1.31 times in the third type, and 1.23 times in the fourth type compared to the flat-plate collector (the first type).

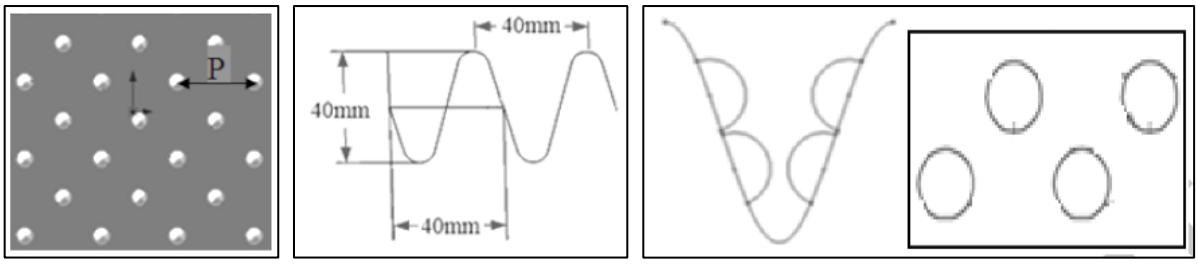

Figure 2. 17: different types of the absorber plate [41].

Saha and Sharma (2017) [42] analyzed DP-SAH. They developed a computer program in C++ language to solve the mathematical model and get results in the energy, effectiveness, and exergy efficiencies. Different types of absorbent plates were used: v-corrugated absorption and v-corrugated bottom plate, trapezoidal absorption and trapezoidal bottom plate, v-corrugated absorption with the flat bottom plate, and flat plate absorber, as shown in figure (2.18). It was observed that thermal energy gain and energy efficiency increased, but the exergy efficiency decreases with the MFR increase. Still, the effective thermal energy gain and efficiency increase until a specific value of the MFR decreased sharply. The enhancement in energy is 7.12%, effectiveness is 7.20%, and exergy efficiencies are 15.43% at MFR of 0.035 kg/s for the v-corrugated absorption and v-corrugated bottom plate collector concerning the flat plate absorber collector.

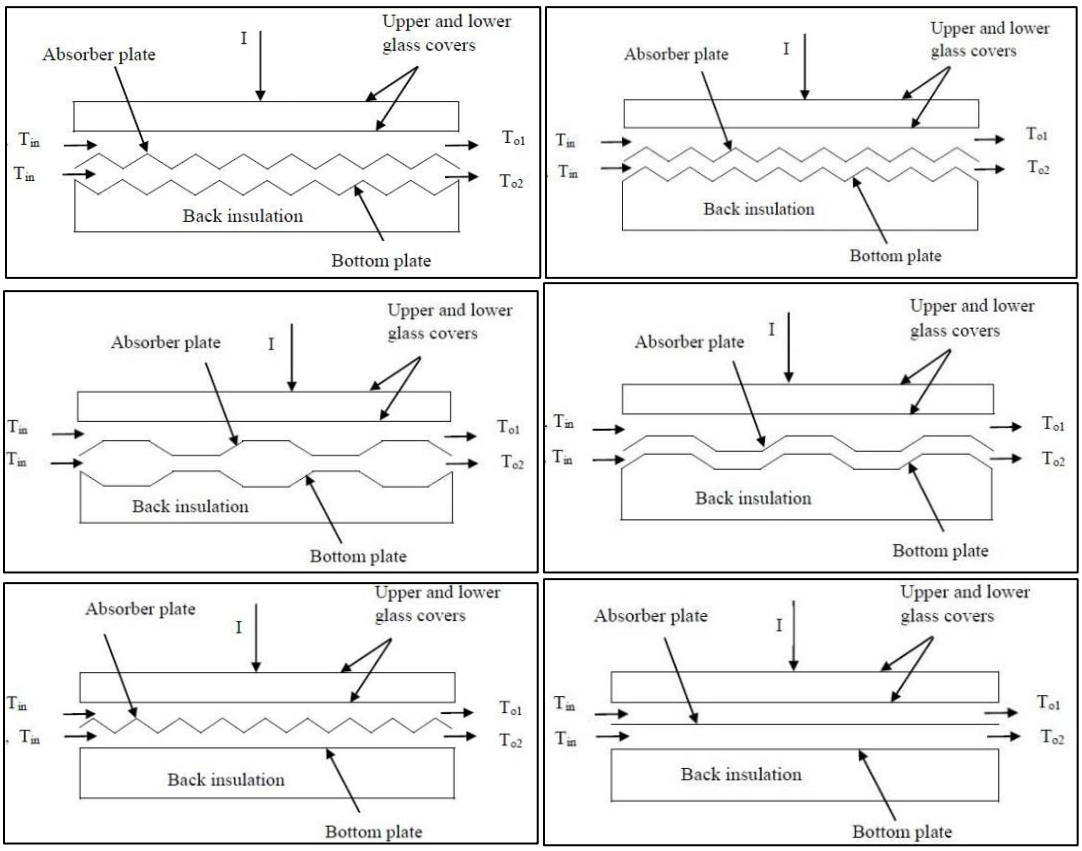

Figure 2. 18: Double-pass solar air heater with different geometry of absorption plates [42].

Satyender Singh (2020) [43], studied experimentally a bed SAH is composed of a porous serpentine wire mesh as shown in figure (2.19). The best thermal and thermo-hydraulic efficiencies were around 80 percent and 74 percent, respectively, with 93 percent porous serpentine-packed bed DP-SAH, which is around 18 percent and 17 percent higher than SP-SAH, respectively. The numerical investigations are executed using a Computation Fluid Dynamics tool, and the results are validated using experimental data. A range of 85 to 95 percent porosity, 0.05 to 0.075 m wavelength, 0.012 to 0.016 m amplitude, 0.025 to 0.046 m hydraulic diameters, and 0.01 to 0.05 kg/s MFR is tested.

When comparing serpentine-packed bed SAH to flat-packed bed SAH, the numerical results showed that serpentine-packed bed SAH had a maximum of 24.33 percent greater thermo-hydraulic performance. The ideal configuration had a wavelength, an amplitude, a hydraulic diameter, a porosity, and an MFR of 0.075m, 0.012 m, 0.0835 m, 90 %, and 0.03 kg/s, respectively.

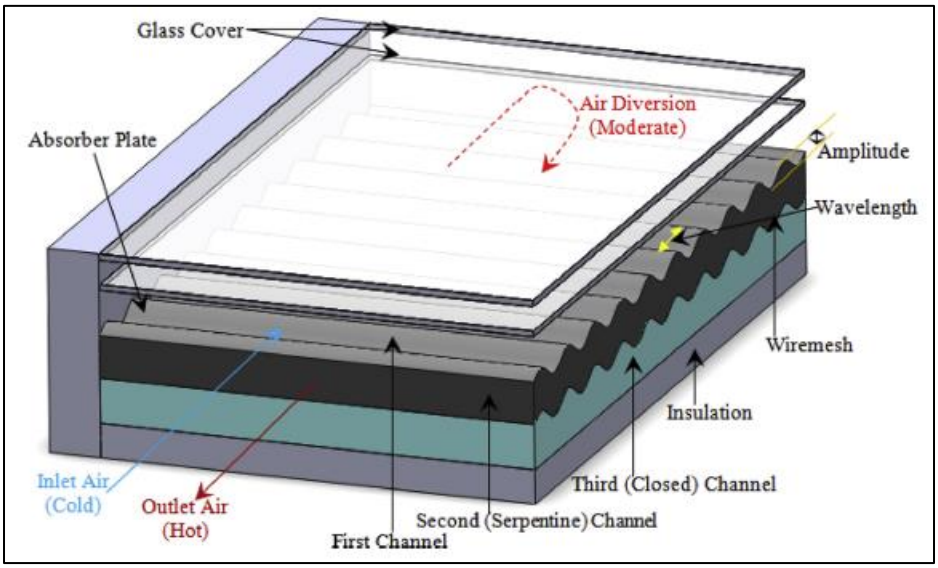

Figure 2. 19: Schematic of the SAH [43].

Khatri et al. (2020) [44] fabricated and evaluated the performance of a solar air heater with an arched wavy absorber plate having porous aluminum wire mesh cylindrical fins. The arched absorbent plate design results in increased air turbulence and vortex generation. This design breaks the laminar sublayer near the surface of the absorbent plate and improves heat transfer. The presence of porous cylindrical wires fins from aluminum increased the porosity of the fins, which reduced pressure drop and improved the thermal performance of the solar air heater. A comparative analysis was carried out for three different arrangements; wavy plate without fins, arched wavy plate without fins, and arched wavy plate with fins.

Three different speeds are considered for the experimental analysis, which are 3, 5, and 9 m/sec, and solar radiation ranging between 600-800 W/m². A temperature difference is obtained between the inlet and outlet of the arched wavy-shaped plate with fins, arched wavy-shaped plate without fins, and straight wavy-shaped plate without fins are in the range of (55 – 70) °C, (30 – 40) °C, and (20 – 30) °C, respectively. While the efficiency reaches (55 – 80) %, (35 – 50) %, and (25 – 40) %, respectively, at the flow velocity of 5 m/sec.

Table 2. 1: Show the summery of the authors studied multi types of corrugated SAH.

Author (s)	year Heater type Study	Place of study	Modifications	Operation conditions	Finding
Joudi and Mohammed [23]	1986 Single Exp.	Basra	v-corrugated	MFR = 0.016-0.0385 kg/s.m^2	The collector's efficiency was approximately 6% higher in the winter than in the summer. With an average collector efficiency of 42 percent, summer noon air outlet temperatures of 70 °C were achieved.

Author (s)	year Heater type Study	Place of study	Modifications	Operation conditions	Finding
Metwally et al. [35]	1997 Single Exp.	Cairo	Different geometry	MFR=0.01-0.1 kg/s.m^2, I=650-950 W/ m^2.	The results showed that the efficiency of the corrugated collector increased by (15-43) % compared to the traditional design (flow below flat absorber).
Kabeel and Mecarik [24]	1998 Single Th.	Egypt	v-corrugated	/	The pressure drops in the SAH, and the heat transfer to the flow in the heater rise as the triangle angle of the triangular collector increases (ranges from 50 to 60˚).
Karim and Hawlader [36]	2006 Single and Double Exp. and Th.	Singapore	Flat, finned and v-corrugated	MFR=0.0154 -0.056 kg/s.m^2	Compared to FP-SAH, the VC-SAH is 10-15% more efficient in an SP-SAH and 5-11% more efficient in DP-SAH modes.
El-sebaii et al. [25]	2011 Double Exp. and Th.	Tanta	Flat and v-corrugated plate	I max = 978 W/ m^2, Ta = 36 °C, MFR=0.01-0.06 kg/s	The thermo-hydraulic efficiency, efficient, and outlet temperature of DP-VCP-SAH are 14%, 11-14% and 5%, respectively higher than that of the DP-FP-SAH.
Hedayatizadeh et al. [26]	2012 Single Num and Th.	Iran	V -corrugated	I=1000W/m^2, Ta = 300-330 K, MFR=100 kg/h.m^2.	High Aspect Ratio, low triangle duct altitude, and MFR are required, as is maintaining the incoming air temperature as low as feasible.
Huseyin Benli [37]	2013 Single Exp.	Elazig / Turkey	Different types of absorber plates	I=307-597 W/ m^2, Re=2500-5000	Thermal efficiency range between (25 – 55) %, (22 – 46) %, (20 – 42) %, (15 – 28) %, and (7 – 17) %, for corrugated, trapeze, reverse corrugated, reverse trapeze, and flat plate, respectively.
Handoyo et al. [38]	2014 Single Exp.	Indonesia	v-corrugated and obstacles bent (80 – 0) °	I=430-716 W/ m^2, Re=1447-7237	When the obstacles are bent 30° instead of 0°, the air temp increase, the efficiency of 5.3 percent is reduced, and the pressure drop is 17.2 percent lower.
Hedayatizadeh et al. [27]	2016 Double Th. and Num	Iran	V – corrugated	I= 700 W/ m^2, Ta = 300 K, MFR= 0.001- 0.049 kg/s	Max. η_{Ex} for double-pass/glazed v-corrugated plate SAH at corrugated height = 0.0122 m, heater area = 1.79 m^2, and MFR = 0.005 kg/s is 6.27%.

Author (s)	year Heater type Study	Place of study	Modifications	Operation conditions	Finding
Ho et al. [28]	2016 Double Exp. and Th.	Taiwan	V-corrugated	I=830-1100 W/ m^2, MFR=0.0107 - 0.0214 kg/sec.	When the air MFR and/or the recycling ratio rise, the additional improvement in collector efficiency E_h diminishes.
Velmurugan and Kalaivanan [39]	2016 Single and Double Exp.	India	Finned, roughened, and v-corrugated wire mesh	I=500-600 W/ m^2, MFR=0.01-0.04 kg/sec.	The max temp of air gained is 26.28 °C for type-A SAH at an MFR of 0.01 kg/s, max efficiency of 82.29% is obtained at an MFR of 0.04 kg/s and max exergy gain is 63.15 W for type-A at an MFR of 0.01 kg/s and I=600 W.
Ho et al. [30]	2017 Double Exp. and Th.	Taiwan	v-corrugated	I = 830-1100 W/ m^2, T in = 293 – 313 K, MFR=0.0107 - 0.0214 kg/s	When the recycling ratio goes up and the air MFR goes down, the collector works better, and the device works better when the air comes in first through the bottom channel (flow pattern A) rather than the upper channel (flow pattern B).
Lakshmi et al. [16]	2017 Single Exp.	Odisha, India	Trapezoidal corrugated	I max = 992 W/m^2,	The max. thermal efficiency of an FP-SAH is 15.8 percent, while that of a trapezoidal-corrugated absorber is 21.5 percent. The max. thermal and exergy efficiency for trapezoidal with storage material is 58.16 and 14.6 %.
Abed et al. [40]	2017 Single Exp.	Bucharest	V-porous and U- corrugated	I=222–1118.5 W/m^2, MFR=0.33 kg/sec.	Based on the relative root, the average error was around 7.75 percent for the V-corrugated porous absorber and 10.55 percent for the U-corrugated absorber.
Sharam and Saha [29]	2017 Double Th.	India	v-corrugated	I=1000 W/ m^2, MFR = 0.014 - 0.083 kg/sec, T_a = 30 °C.	η_{th} increases with the increase in MFR, but thermo-hydraulic efficiency rises up to a specific constraint of MFR and there after it decreases for double-pass.
Li et al. [41]	2017 Single Exp.	Zhengzhou city of China	Different types of absorber plates	I=1200– 2500 W/m^2, MFR = 40 – 80 m^3/h.	The collector's efficiency increased by about 1.08 times in the second type, 1.31 times in the third type, and 1.23 times in the fourth type compared to the flat-plate collector (the first type).
Som Nath Saha [42]	2017 Double Th.	India	Different types of absorber plates	I= 200 - 1000 W/ m^2, MFR = 0.035 - 0.083 kg/sec, T_a = 303K.	The enhancement in energy is 7.12%, effectiveness is 7.20%, and exergy efficiencies are 15.43% at MFR of 0.035 kg/s for the AH-1 collector concerning the AH-6 collector (flat plate collector).

Author (s)	year Heater type Study	Place of study	Modifications	Operation conditions	Finding
Harde et al. [17]	2018 Single Exp.	India	Trapezoidal corrugated	I=500 – 1000 W/m^2	When comparing conventional and modified SAH, heat absorbed is 600 W and 900W, respectively, higher in modified SAH by about 50% than the convectional SAH.
Diana et al. [18]	2019 Single Th.	Surabaya / Indonesia	Trapezoidal corrugated	Re = 10600-12700, I= 800 – 1000 W/m^2.	The results showed that the highest outside air temperature is 322.2 K at Re is 10600, and the lowest is 318.3 K at Re is 12700.
Darici and Kilic [19]	2020 Single Exp.	Konya / Turkey	Trapezoidal corrugated	I=400 –1026 W/m^2, MFR=0.022-0.044 kg/sec.	The results show that the SAH with a trapezoidal absorber plate has a daily thermal efficiency of 63% at 0.044 kg/s. The outlet temp. of trapezoidal is higher than flat plate is 9 °C at MFR is 0.022 kg/s.
Khatri et al. [44]	2020 Single Exp.	Jaipur / India	Different geometry	I= 600-800 W/m^2, speed=3-9 m/sec.	A temperature difference is obtained between the inlet and outlet of types A, B, and C are in the range of (55 – 70) °C, (30 – 40) °C, and (20 – 30) °C, respectively. While the efficiency reaches (55 – 80) %, (35 – 50) %, and (25 – 40) %, respectively, at the flow velocity of 5 m/sec.
Omer et al. [31]	2020 Single Num	Nairobi / Kenya	v-groove	I=259- 817 W/ m^2, MFR = 6.6 g/sec, T_a = 291 K.	The thermal efficiency was enhanced by 29%. It was concluded that modifying the corners of the triangular channels of the v-groove absorber plate increases the coefficient of convection heat transfer.
Satyender Singh [43]	2020 Single and double Exp. and Th.	Jalandhar / India	A serpentine wavy wire mesh that is porous	I max =905 W/ m^2, MFR = 0.01 - 0.04 kg/sec.	Thermal and thermo-hydraulic efficiencies were 80% and 74%, respectively, for a 93% porous serpentine packed bed DP-SAH, which is around 18% and 17% higher than SP-SAH, respectively.

Author (s)	year / Heater type / Study	Place of study	Modifications	Operation conditions	Finding
Tuncer et al. [32]	2020 / Double / Exp. and Num.	Burdur / Turkey	v-groove absorber plate	MFR = 0.015 – 0.011 kg/sec, I=900 – 1100 W/m^2.	The yearly average thermal efficiency of VTP-SAH, DP-SAH, and PP-SAH is in the range of 70.91 – 78.18, 61.86 – 66.95, and 54 – 60.29 %, respectively, so max. η_{th} is 90.65% for VTPSAH. The average exergy efficiency of PP-SAH, DP-SAH, and VTP-SAH is 6.68 – 9.74, 12.28 – 15.68, and 14.62 – 18.95 %, respectively.
Xiao et al. [20]	2020 / Single / Num.	Wuhan / China	Trapezoidal corrugated	I=1000 W/m^2, Re= 6000-18000	When compared to the FP-SAH, the maximum enhanced in energy efficiency was 24%, and exergy efficiency was 31%.
Alic et al. [22]	2021 / Single / Exp. And Num.	Elazig / Turkey	Trapezoidal aluminum sheet material	I max = 930 W/m^2, MFR = 0.0385 kg/sec	It stated that the design could improve temperature, velocity, and pressure distribution residences and that Z-type SAH had an average efficiency of 78 percent.
Farhan et al. [33]	2021 / Single / Th. and Num.	Baghdad / Iraq	v-corrugated integrated with twisted tape inserts	I max = 1053 W/m^2, Re = 1000-20000.	When compared to VC-SAH without TTI, the max thermo-hydraulic and thermal efficiencies of the VC-SAH-TTI are 17 and 17.5 percent, respectively. Max. η_{th} is 74.42% and max h is 68.3 W/m^2. C for VCSAH-TTI
Hassan et al. [34]	2021 / Single and Double / Exp.	Egypt	v-corrugated perforated finned	/	Under SP, 1/3 DP, 2/3 DP, and DP conditions, average daily exergy efficiency for CP-SAH 47, 55, 76, and 54%, percentage increments compared to FP-SAH. FP-SAH has the worst daily energy efficiency, better efficiency for C-SAH, max. air temp. rise, thermal η, and exergy efficiency for CP-SAH. Max. η is 56.7, 70.58, and 71.85% for FP-SAH, C-SAH, and CP-SAH, respectively.
Raddy et al. [21]	2021 / Single / Exp.	Assam / India	Reverse and cross - corrugated trapezoidal	MFR= 0.00039– 0.0156kg/sec, inclination angles 15, 30, 45°, I=290 - 965 W/m^2, Ta= 14.28-33.3 °C	The max energy efficiency for type-1 and type-2 SAH was 30.3 percent and 39.4 percent, respectively.

Based on what was presented in this chapter from previous studies, it was found that the plate in the form of a trapezoidal was studied in the single-pass solar air heater only, and it was not studied in the double-pass solar air heater so that it will be examined in this thesis. Also, a plate with a V-groove will be manufactured. The effect of the mass flow rate on it will be studied, which differs from the parameters of operating conditions that previous researchers studied. The results will be compared with the third plate, which is flat for the double-pass solar air heater, to see the extent of improvement in thermal efficiency and the output temperature of the air.

Chapter Three

Experimental Work

Chapter Three

Experimental Work

3.1.Introduction

This chapter reviews the experiments side as several experiments are conducted distributed over three states of turbulent flow in the (DP-SAH), flat, trapezoidal and V-groove plates. These are experimentally examined, with MFR of (0.6, 1.2, 1.8, and 2.4) kg/min corresponding to Reynolds' numbers (4300, 8300, 11900, 16200), respectively. The model of the current DP-SAH has been manufactured and tested under indoor operating conditions. The study was conducted indoors to control the surrounding external parameters such as ambient temperature, wind speed, and solar radiation and to facilitate the analysis of the effect of changing the air mass flow rate on the different plates. Additionally, the fundamental components of every experimental setup and general operating principles are described. This chapter also includes information on the suggested DP-SAH with the solar simulator, measurement tools, experimental procedures, and uncertainty analysis. Finally, the test's practical components are explained, and the validity of the experimental data obtained with the numerical data results is described.

3.2.Experiment Devices

The artificial solar simulator with a voltage regulator, the absorber unit, and the DP-SAH test platform make up the experimental system's three main components. The experimental apparatus is depicted in pictures, and an outline diagram in figures (3.1) and (3.2) below is a detailed description of these elements:

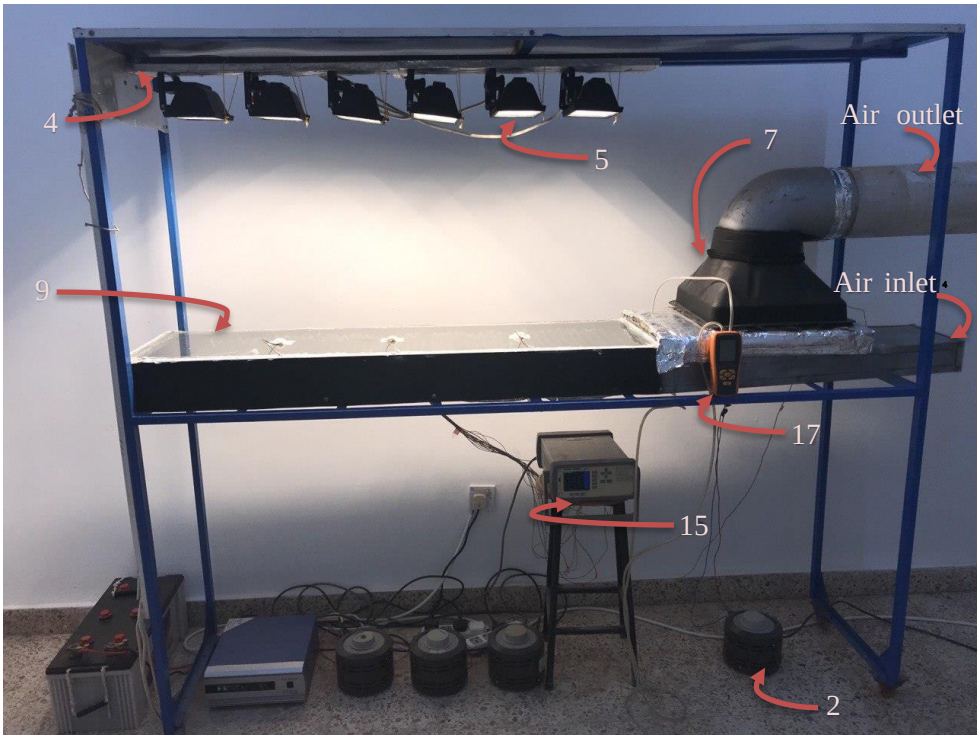

Figure 3. 1: Digicam image of indoor experimental apparatus of the DP-SAH.

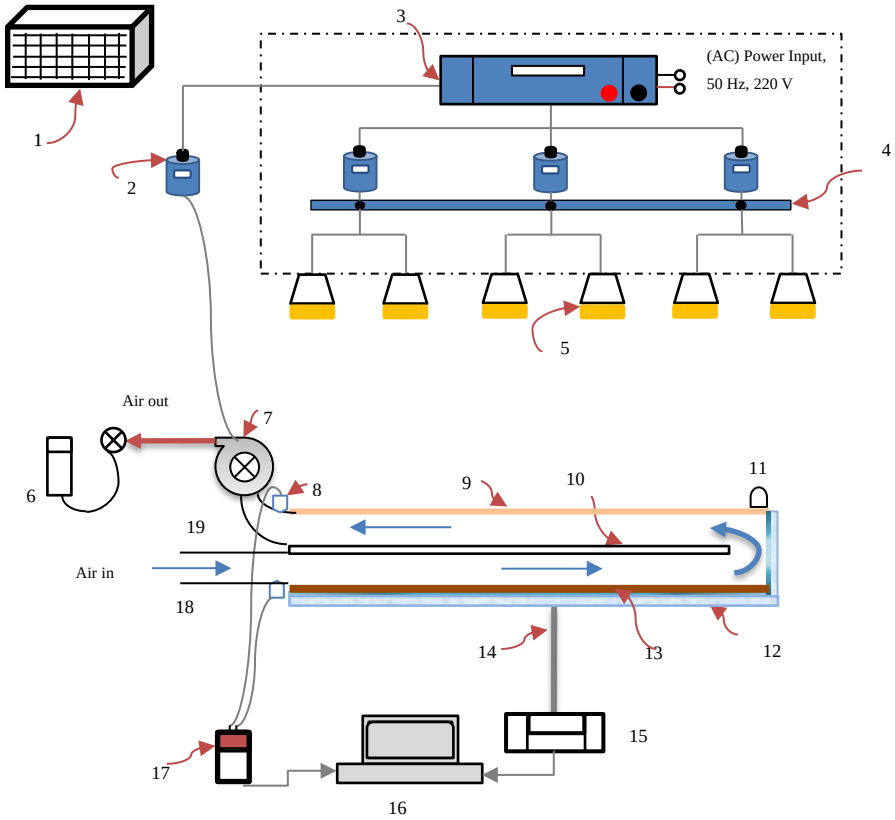

1	Air conditioner
2	Contact voltage regulator
3	Automatic voltage regulator
4	Electrical connector
5	Halogen lamps
6	Anemometer (Vane type)
7	Axial fan
8	Pressure typing
9	Glass cover
10	Absorber plate
11	Solar power meter
12	Insulation (wood and glass wool
13	Back plate
14	Thermocouples wires
15	Data logger
16	Laptop
17	Digital manometer
18	Inlet duct
19	Outlet duct

Figure 3. 2: Sketch diagram of indoor experimental devices of the DP-SAH.

3.2.1. Double-Pass Solar Air Heater (DP-SAH)

The experiment apparatus of DP-SAH is a rectangular duct made of plywood 0.025 m thick with a cross-section of (1.284 × 0.320 × 0.084) m used to make the multi-passes. It is covered by a single-layer glass layer and has great transmittance at a thickness of 4 mm. The flow channel of the experimental setup consists of three units:

1. The entrance portion (0.9 × 0.32) m,
2. The test section (1.2 × 0.32) m,
3. The exit section (0.45 × 0.32) m;

There is also an 0.084 m air space at the end of collector, enabling airflow towards the top channel. The aspect ratio (W/H) of the first and second channels of the heater is always kept at 10. They have a 0.032 m and 0.411 m^2 gap height and area of the collector, respectively; this data is taken from ASHRAE standards [45].

Provide the solar air heater with an axial fan in the air outlet area. The fan draws air, and a voltage regulator can control its speed (mass flow rate). This fan has the following specifications; type: VIF-25V2S, IP: 54, V: 220, Cos (): 0.95, W: 54, Hz: 50, rpm: 2500, m3/h: 1450, kg: 3, the fan shown in figure (3.3).

Figure 3. 3: Axial fan.

The experimental setup consists of the entry section, exit section, test section of the DP-SAH, and axial fan. the DP-SAH counter-flow consists of two passes of air, as follows:

1. The first pass flow, in which air travels through the lower channel, is constructed between the absorption plate and the backplate of the collector.
2. The second-pass flow, in which air passes between the cover glass and the absorption plate. The channel (second-pass flow) is established through which recirculated air passes, as shown in figure (3.2).

Table (3.1) contains information on the experimental rig DP-SAH and the trapezoidal and V-groove absorption plates used in it.

Table 3. 1: Description of the DP-SAH with absorber plate.

Parameter	**Values**
DP-SAC:	
Length	1.284 m
Width	0.32 m
Height	0.084 m
Channel height	0.032 m
Effective glazing area	0.411 m^2
Glass thickness	0.004 m
U-turn spacing	0.084 m
Absorber Plate	
Length	1.2 m
Width	0.32 m
Thickness	0.0007 m
Backplate	
Thickness	0.0007 m
Length	1.284 m
Width	0.32 m

3.2.2. The Absorber Plates:

The absorber plate is an essential part of the system. It is made of aluminum sheets for its high thermal conductivity with a thickness of 0.7 mm, and the two sides are painted matte black to absorb more solar radiation. The absorber plate is installed in the center of the collector so that the collector is divided into two passages, upper and lower, each of them 32 mm high. At the end of the plate, there is an 84 mm gap that allows air to pass from the first passage (lower) to the second passage (upper).

Experiments are conducted on three types of plates: flat, trapezoidal, and V-groove types. The second and third types have shapes that help increase air turbulence and the absorption surface area, which increases heat transfer by forced convection between the air and the absorbing plate. Figures (3.4), (3.5), and (3.6) show the three types.

The plates were manufactured by Asad Al-Mustakbel Company, where a Hydraulic Press Brake machine was used to form the plates according to the required measurements. The device works by bending, where the plate was cut before starting form with a width of 320 mm, and the trapezoidal plate was formed using the bending method and according to the dimensions shown in Figures (4.5) and (4.8), so that the length of the plate after starting is 1200 mm. In the same way, the grooved plate was created.

Figure (3.4) shows the flat plate after painting both sides with a matte black color. At the same time, figure (3.5) indicates the corrugated board in the manufacturing stage before painting. Figure (3.6) shows the plate with a groove installed in the solar air heater during the practical experiments.

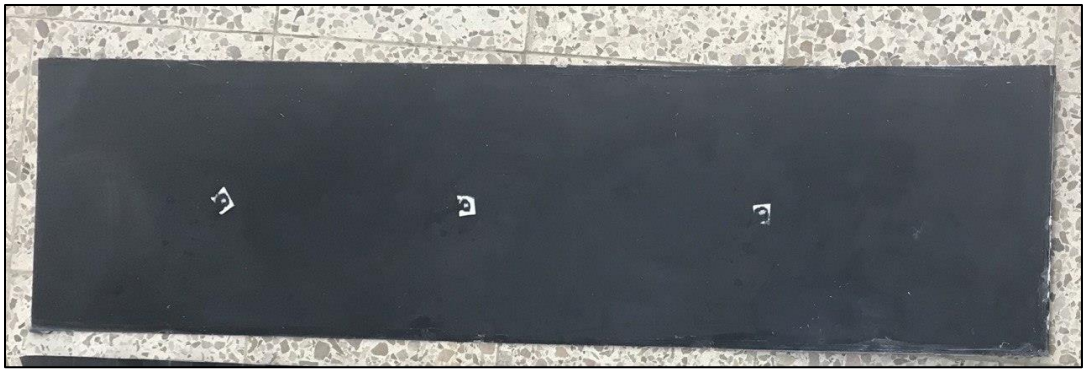

Figure 3. 4: Photograph of flat absorber plate.

Figure 3. 5: Photograph of trapezoidal absorber plate.

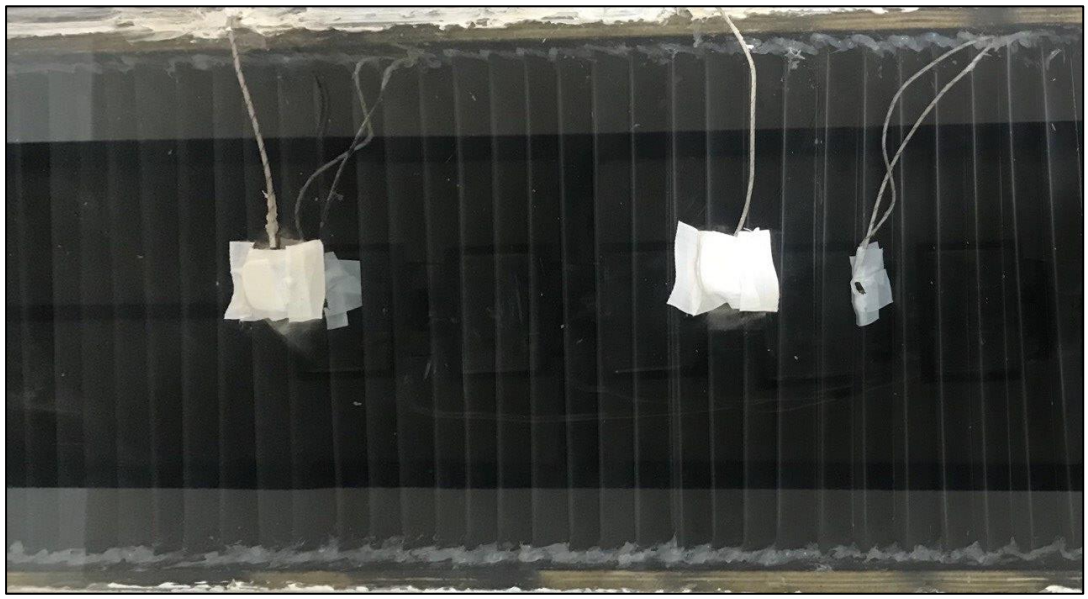

Figure 3. 6: Photograph of V-groove plate.

3.2.3. Simulator For Generating Sunlight:

The solar simulator seeks to provide a solar flux to test solar systems in the laboratory. It is frequently used to evaluate solar collectors, sunscreens, and photovoltaic cells. Furthermore, to prevent the various outdoor conditions and weather variations, the experiment was conducted indoors to provide the ambient temperature and radiation intensity at any time of the day [46]. The halogen lights and automatic voltage regulator control with a power supply are the main parts of the solar simulator used in this study.

3.2.3.1. Halogen Lights:

Recent studies have frequently used tungsten halogen light in indoor testing under lab circumstances; figure (3.7) shows tungsten halogen light. In thermal radiation, tungsten halogen light is identical to the spectrum of sunlight and has a wavelength ranging from 360 to 2500 nm. Halogen lamp radiates at 3200 K black body temperature. A reflector and glass cover must also be built for each lamp to minimize irradiance losses and ensure user safety. The employed tungsten halogen lights' spectrum distribution and properties are detailed in Appendix [A].

Figure 3. 7: Tungsten halogen light.

In the present work, the indoor solar simulator uses six tungsten halogen lamps, each with a maximum power of 500 watts, as shown in figure (3.8). The lamps were placed perpendicular to the DP-SAH glass housing at a distance of 0.7 m, resulting in average full irradiation of approximately 825 W/m^2. Three VARIAC voltage regulators with a capacity of 1000 VA are used to adjust the directed sunlight intensity of the test collector.

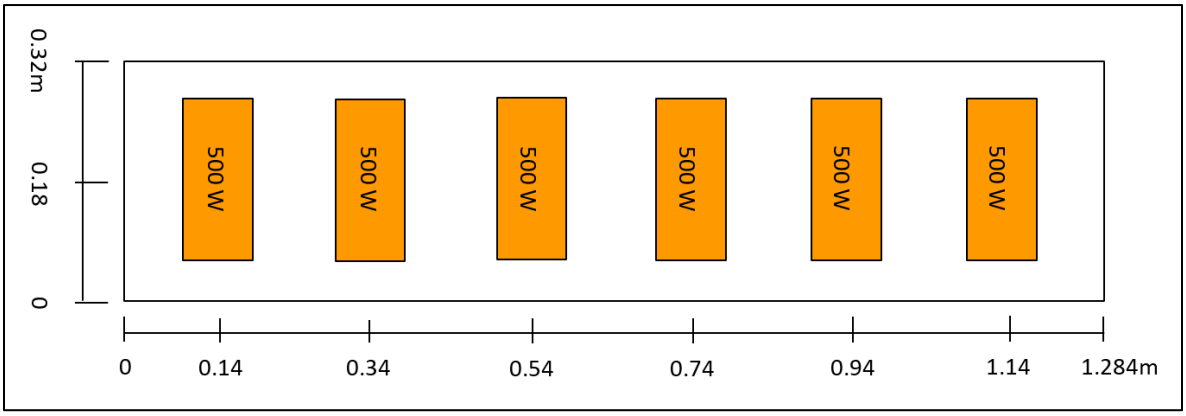

Figure 3. 8: Halogen light configuration diagram for the solar simulator used for testing collectors.

The TM-207 solar power meter is used to measure the solar radiation intensity at the plate of the DP-SAH with an accuracy of (± 5 %). Figure (3.9) shows the average solar flux value calculated at 15 places in the collector's top plane.

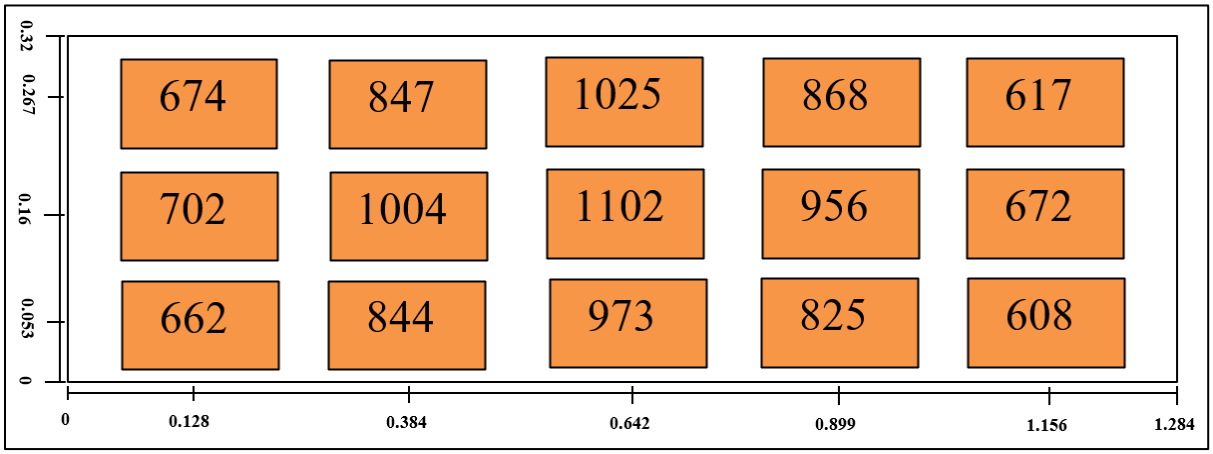

Figure 3. 9: The average solar flux value (W), (all dimension in mm).

3.2.3.2. Voltage Regulator Control

In the present study, three VARIAC voltage regulators, for each unit capacity of 1000 VA, are used to control the inlet power in three halogen lamps; figure (3.10) shows voltage regulator control. Electricity in the range of 220V is delivered to the contact voltage regulators. The properties of VARIAC; type: HSN 0103 220 V PLUG, Up: 220 V, Us: 0-250 V, 50-60 Hz, Is: 5 A, P: 1.25 k VA, IP: 20, ta: 25.

Figure 3. 10: Voltage regulator control.

3.3.Measuring Devices

Different measurement systems are needed for each experimental test to meet the conditions for the success of these readings. The primary factors in the current work, including temperature, pressure, air MFR, and solar irradiation, are specifically measured using a variety of instruments. It is explained in more detail below;

3.3.1. Temperature Recording Device:

In this work, nineteen thermocouples of K-type (Nickel-Chromium/Nickel-Alumel) are employed to monitor the temperatures of the double-pass solar air heater during the experiment. K-type thermocouples used with an accuracy of (± 0.4 % ◦C) and a temperature measuring range (-100 to 1300 ◦C); figure (3.11) shows thermocouples of K-type. Moreover, the thermocouples were attached in three distance locations: a glass cover, the surface of the absorption plate, the backplate surface, the first and second passages of airflow, all at distances of 0.330, 0.660, and 0.990 m from the entry edge, as illustrated in figure (3.12).

Figure 3. 11: Thermocouples K-type.

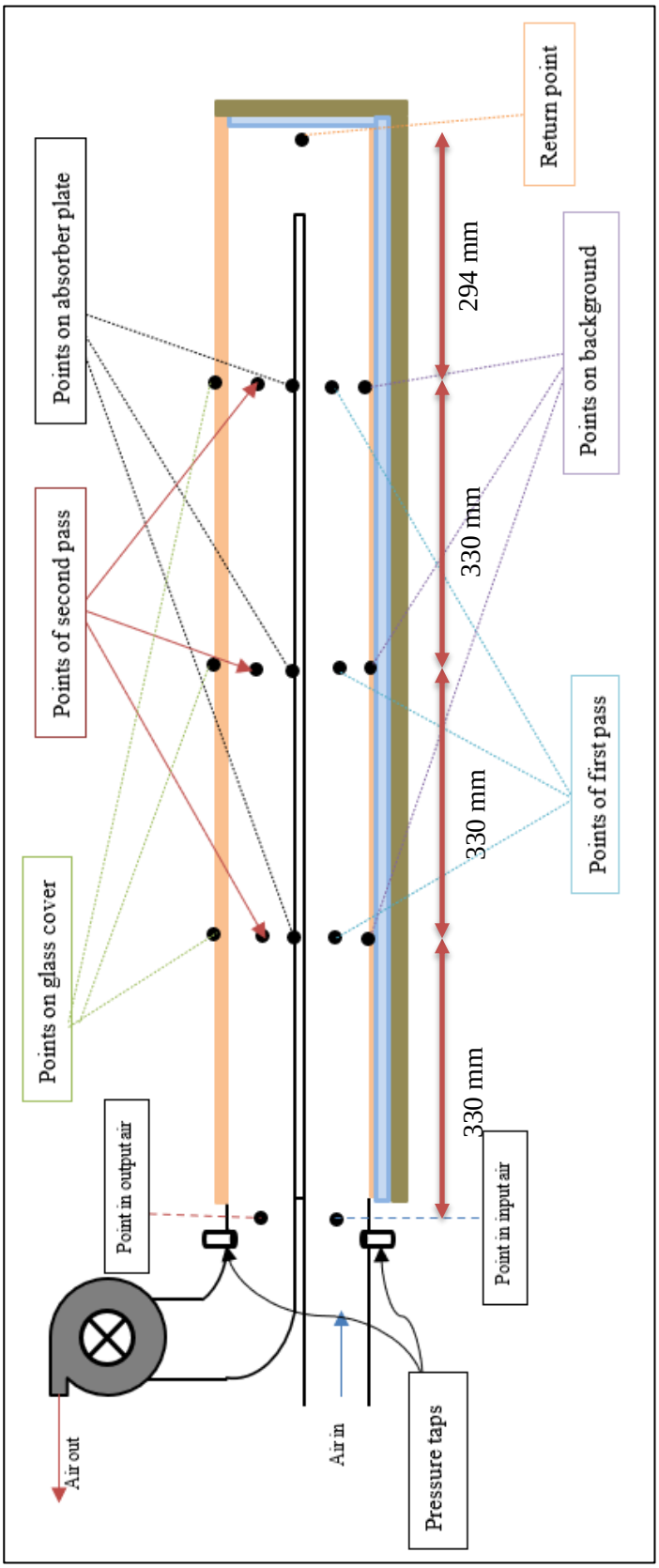

Figure 3. 12: Schematic of thermocouples locations and pressure points in front views.

In addition, one thermocouple is installed at both the input and output air units. During the tests, a data logger model AT-4532x is used to record the temperature readings from the thermocouples in the SAH every 60 seconds, as shown in figure (3.13).

The thermocouples calibration considers eleven-points temperature, i.e., 0 to 100 °C. To monitor temperatures, use a mercury thermometer and all temperature sensors connected to the multi-channel data logger type (AT-4532); calibration of thermocouples is shown in Appendix B, and the data logger's characteristics are shown in Appendix C.

Figure 3. 13: Data logger thermometer device.

3.3.2. Pressure Device:

In the current experiment, a calibrated digital manometer was used to monitor the pressure drop across the collector (510 types). The specifications of the digital manometer, which is situated between the DP-SAH's inlet and outlet ducts, include an operational range of 0 to 35 kPa, an accuracy of (± 0.5%) of a wide scale, and a

resolution of (0.01 kPa). The air gap between the input and output of the double-pass solar air heater has a pressure difference, as shown in figure (3.14).

Figure 3. 14: monitor the pressure drop.

3.3.3. Air Mass Flow Rate

The airflow rate at the DP-SAH duct's outlet was measured using a calibrated vane-type (AM-4206M) anemometer, as shown in figure (3.15), where the device calibration certificate is shown in Appendix D. The airflow value, and air temperature are shown simultaneously on this gadget. Additionally, the anemometer's specification spans (0.4 - 35 m/sec) with an accuracy of (4%). By using the vane-type (AM-4206M) anemometer to measure the air velocity at different points at the end of the air outlet tube, where five points distributed over the circular section of the pipe were taken, and the speed was measured. Then the average of these velocities was taken according to the equation (3.1). The following formulas are used to determine the average velocity value for each trial:

$$V_m = \frac{V_1+V_2+\cdots+V_N}{N} \quad 3.1$$

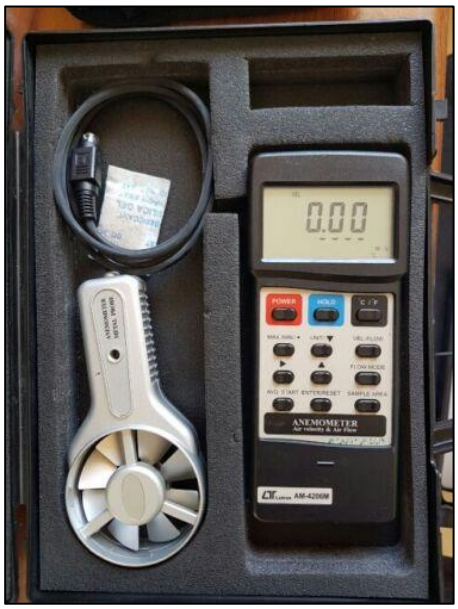

Figure 3. 15: vane-type (AM-4206M) anemometer.

The following method is used to determine the mass airflow rate value for particular research values:

$$\dot{m} = \rho_a V_m A_{cs} \quad 3.2$$

It should be noted that the terms A_{cs} and ρ_a refer to the cross-section area of the duct outlet and the air density at 25 °C, respectively.

3.3.4. Solar Irradiance

In this study, solar irradiation was measured using a calibrated solar power meter (TM-207), as shown in figure (3.13), with an accuracy of (5%) and a range of (0 – 2000 W/m^2), which measures the heat flux intensity at the collector surface in (W/m^2). Additionally, the calibration of the device is shown in Appendix E.

Figure 3. 16: Solar power meter (Pyrometer) device.

3.4.Experimental Tests

In the current study, a chosen solar radiation produced by halogen lights passes through the glass cover and shines on the solar collector's absorption plate. The absorbent wall absorbs the solar radiation and exchanges energy with the moving air in the first and second passes of the DP-SAH.

Additionally, the energy losses from the apparatus's bottom and side walls to the environment are disregarded. According to Table (3.2), the inlet temperature is equivalent to the ambient temperature of 25 °C at one bar of atmospheric pressure. Three models are used for the experiments;

1. Flat plate: it has dimensions of (1200 × 320 × 0.7) mm and is placed in the middle of the solar collector to separate it into two passages with a gap at the end of the collector to allow air to circulate for the second pass at the top of the plate.
2. Trapezoidal plate: it has (1200 × 320 × 0.7) mm and has (20) mm height in the middle of the solar collector.

3. V-groove plate: It has dimensions of (1200 × 320 × 0.7) mm, has (20) mm height and a 60-degree angle, respectively, and is placed in the middle of the solar collector.

Table 3. 2: Air thermal properties at 1 atm pressure and 25 °C[9].

Property	Values
Density	1.184 (kg/m^3)
Heat capacity	1007 (J/kg. K)
Thermal Conductivity	0.02551 (W/m. K)
Dynamic viscosity	1.849 x 10^{-5} (kg /m. sec)

3.4.1. Experimental Procedures

The following steps are used to conduct the experiments:

1. Install the axial fan at the exit point, which is in the form of suction or air withdrawal, and a voltage regulator can control its speed.
2. Fix the halogen light at the height of 70 cm and control it through a voltage regulator to provide the solar air heater with a constant amount of solar radiation up to 825 W/m^2 for all experiments.
3. Install a pressure drop measuring device at the entry and exit points to measure their pressure difference.
4. Fix the flat plate in the middle of the solar air heater to be the first and second passage for air.
5. Install 19 thermocouples in the solar air heater to be in the following locations:
    a. One thermocouple measures room temperature
    b. Two more at the air inlet and outlet.
    c. 3 thermocouples installed on the plate.
    d. 3 thermocouples fixed to the glass.

e. 3 thermocouples installed in the first-pass.
f. 3 thermocouples installed in the second-pass.
g. 3 thermocouples were installed on the background to measure its temperature, where the first thermocouple was seated at a distance of 330 mm, the second at a distance of 660 mm, and the other at a distance of 990 mm from the air inlet for each of (the plate, glass, background, and the first and second passages).
h. The last thermocouple is installed in the U-turn (in 1284 mm).

6. Fix the glass on the solar air heater and seal it.
7. Turn on the data logger and measure the temperatures for all thermocouples so that the reading ranges between 24 – 26 °C, the same as the temperature of the surrounding air entering the device.
8. Turn on the fan to supply the solar air heater with a constant flow rate (0.9 m/s or 0.6 kg/min).
9. Turn on the solar radiation source.
10. After turning on all the devices, wait until the temperature reaches the steady-state point after approximately 50 minutes.
11. Record all temperatures in 19 thermocouples from the data logger and measure the pressure drop at this flow and this plate.
12. Turn off the solar radiation device and wait for it to cool down completely. All readings range from 24 – 26 °C corresponding to the room temperature (the first experiment was completed).
13. Restart the device again with the fan supplied at a constant flow speed (1.75 m/sec or 1.2 kg/min) and repeat steps (from 7 to 12) (the second experiment has been completed).

14. Restart the device again with the fan supplied at a constant flow speed (2.5 m/sec or 1.8 kg/min) and repeat steps (from 7 to 12) (the third experiment has been completed).
15. Restart the device again with the fan supplied at a constant flow speed (3.4 m/sec or 2.4 kg/min) and repeat steps (from 7 to 12) (the fourth experiment has been completed).
16. Install the second plate (trapezoidal plate) and repeat the same steps 4 to 15. Thus, complete four more experiments.
17. Install the third plate with a groove and repeat steps 4 to 15. Thus, complete four more experiments. Finally, a total of 12 trials.

Chapter Four

Mathematical Model and Numerical Analysis

Chapter Four

Mathematical Model and Numerical Analysis

4.1.Overview:

This chapter deals with the methodology used to achieve the objectives mentioned in the first chapter. The research methodology used is mathematical and numerical to investigate the effect of using different types of absorber plates in double-pass solar air heaters and study their effect on thermal and exergy efficiency. This chapter explains the numerical analysis of the current study.

4.2. Physical Geometry Model Description:

Figures (4.1) to (4.8) depict the DP-SAH problem model with three various types of absorber plates (flat, trapezoidal, and V-groove) were constructed using the CFD program COMSOL Multiphysics v5.5.

Building the model began by identifying two geometric domains of a solid nature related to the cover glass, the aluminum absorption, and one fluid domain related to the air. All three models' lengths are 1284 mm, and the width is 320 mm. The glass cover is 4 mm thick, while the thickness of the aluminum absorption was equal to 0.7 mm, and the collector has a 0.411 m^2 aperture area. In this arrangement, air initially inlets through the lower channel (first pass) between the absorption plate and the backplate. Then it recirculates the air into the upper channel (second pass), located between the absorption plate and the glass.

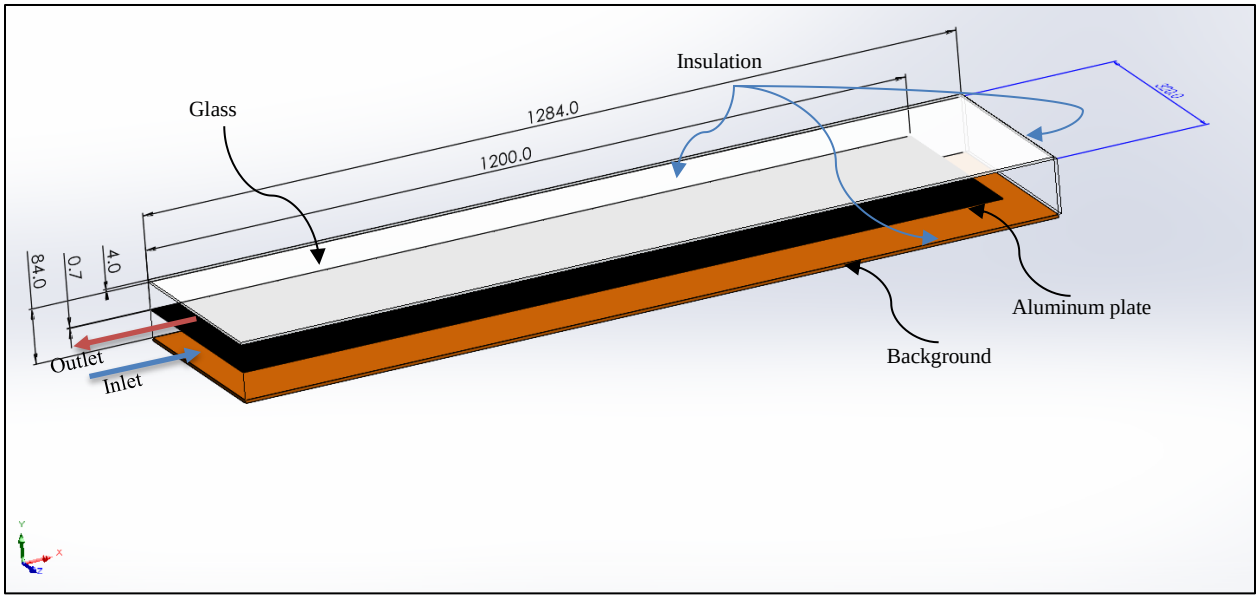

Figure 4. 1: 3D diagram of the flat plate DP-SAH Computational domain (all dimensional in mm).

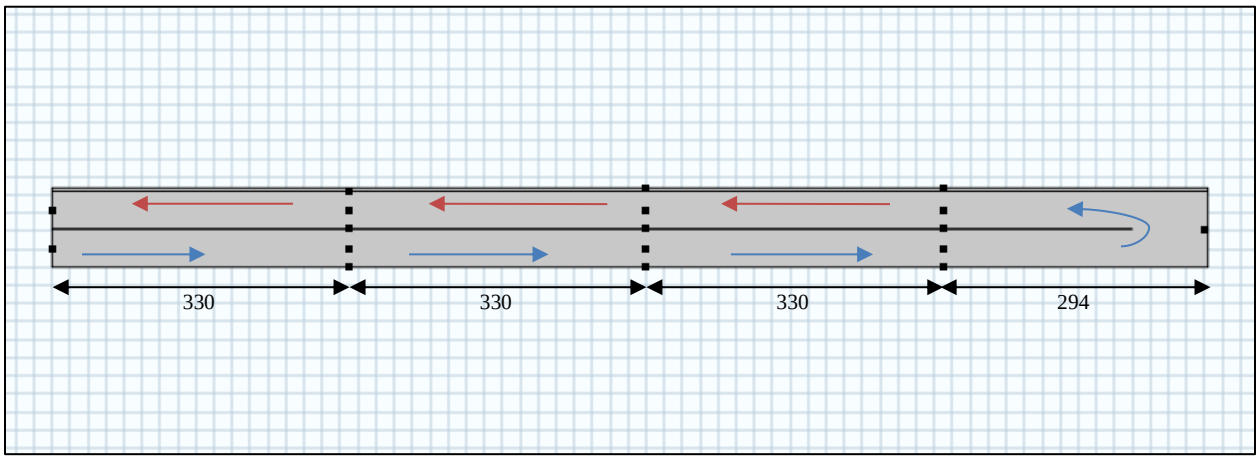

Figure 4. 2: 2D diagram of the flat plate DP-SAH Computational domain with temperature points in the domain (all dimensional in mm).

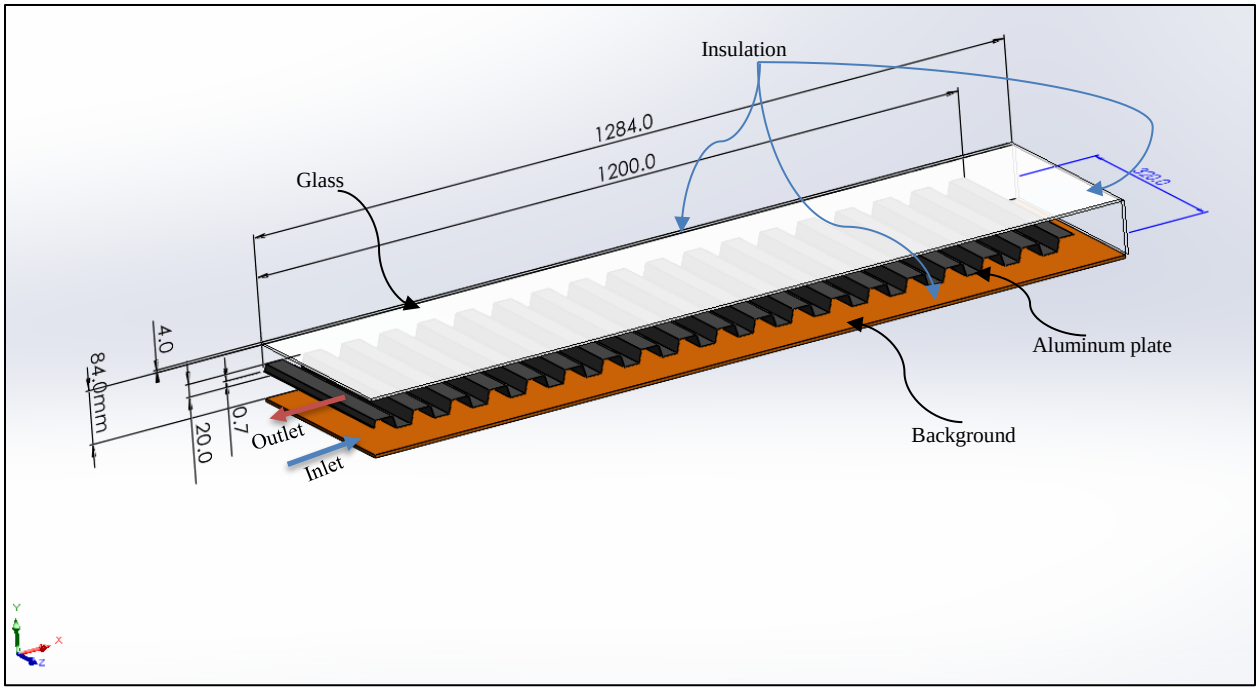

Figure 4. 3: 3D diagram of the trapezoidal plate DP-SAH Computational domain (all dimensional in mm).

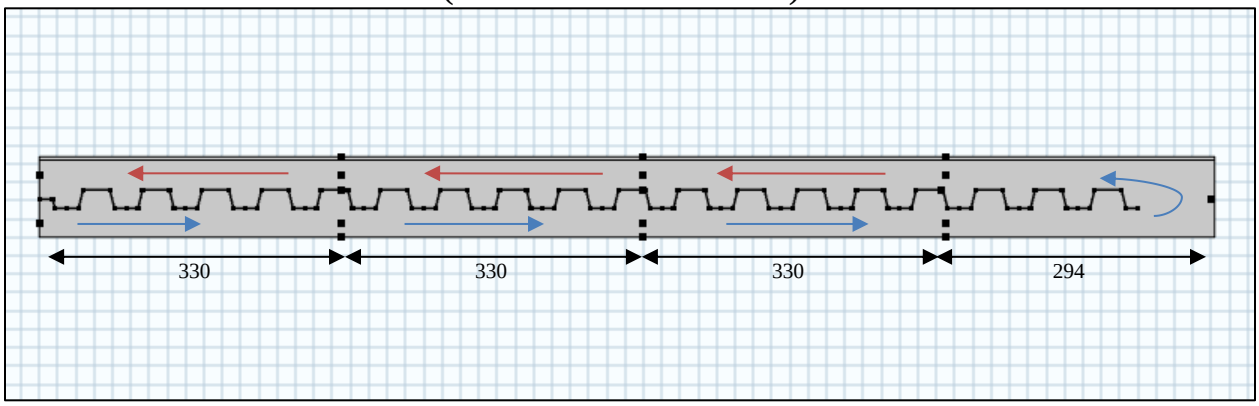

Figure 4. 4: 2D diagram of the trapezoidal plate DP-SAH Computational domain with temperature points in the domain (all dimensional in mm).

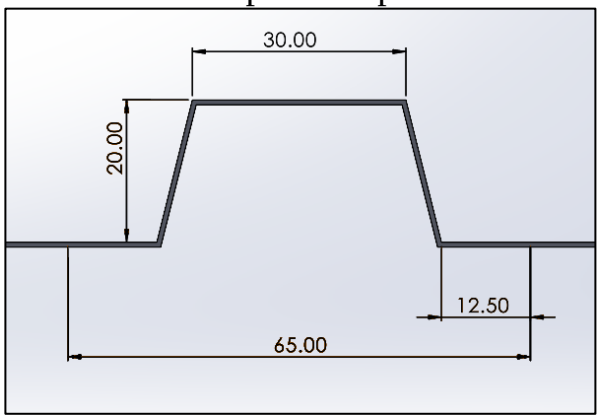

Figure 4. 5: Dimensions of trapezoidal plate (all dimension in mm).

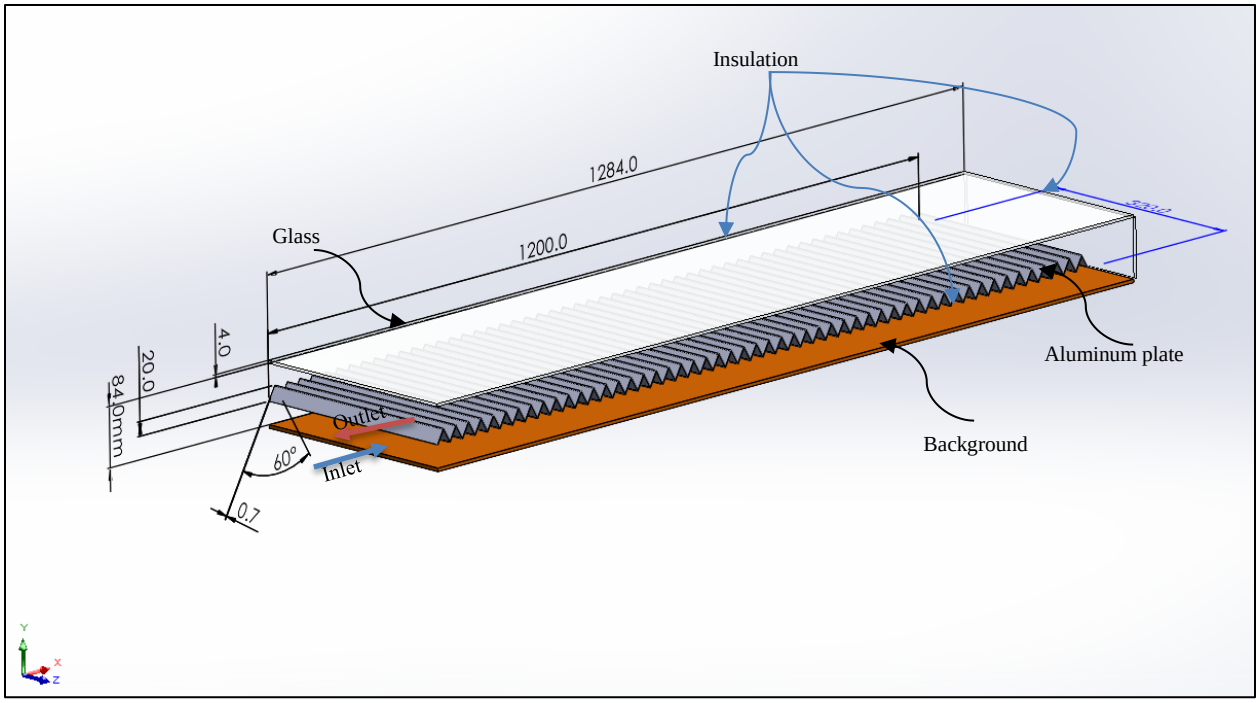

Figure 4. 6: 3D diagram of the V-groove plate DP-SAH computational domain (all dimensional in mm).

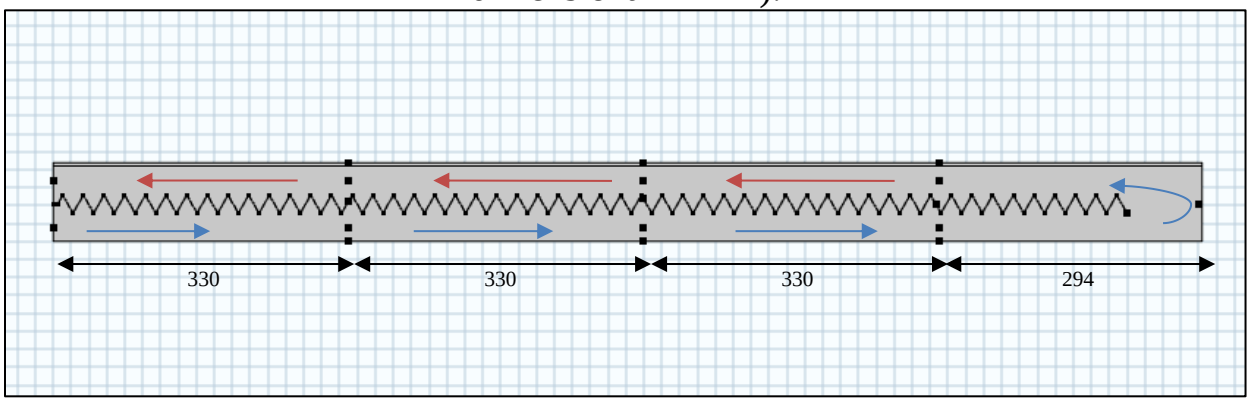

Figure 4. 7: 2D diagram of the V-groove plate DP-SAH Computational domain with temperature points in the domain (all dimensional in mm).

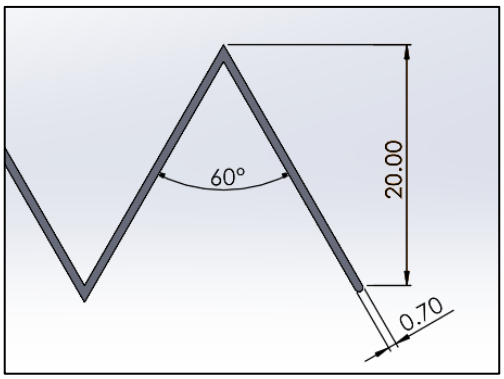

Figure 4. 8: Dimensions of V-groove plate (all dimension in mm).

In the current work, the double-pass solar air heater comprises the following components:

1. ***Glass layer***: 4 mm thick of the transparent cover.
2. ***Channel of airflow***: A two-pass solar heater has an air gap of 32 mm for each channel.
3. ***Absorbent plate***: 0.7 mm thick of the absorber plate is used with different geometry (flat, trapezoidal, and V-groove plate)
4. ***Backplate***: it has 1 mm thick at the bottom of the SAH.
5. ***Insulation materials***: are used on the edges and the bottom as goodness insulation for the collector to reduce heat loss to the ambient; the insulation was used with a thickness of 50 mm surrounding the entire heater, consisting of plywood and glass wool.

Table 4.1 provides a summary of the physical characteristics of the glass cover and aluminum employed in the simulation.

Table 4. 1: Physical properties of the two solid domains [47].

Property	Units	Glass	Aluminum
Density	kg/m^3	2210	2700
Thermal conductivity	W/m. K	1.4	238
Heat capacity at constant pressure	J/kg. K	730	900

4.3. Assumptions and Boundary Conditions:

In the SAH, the main modes of heat transfer are the following:

1. Solar radiation is defined as heat radiation from the sunlight.

2. Heat conduction of the solid walls in the SAH, such as glass cover, absorber plate, and background.
3. Convection heat transfer between the glass cover plate or absorber plate and the airflow.

Under the following presumptions, it is possible to simplify the mathematical model of the governing equations of the double-pass solar air heater for analysis and construction:

1. Two-dimensional, turbulent, and incompressible flow.
2. Performance of the DP-SAH in a quasi-steady state.
3. The temperature was not expected to affect the characteristics of the air properties.
4. The entrance air's temperature was equal to the surrounding air's temperature.
5. Because the collector's thickness is much less than its length, the temperature difference that occurs is rather small. As a result, studies were built to be symmetrical along the z-axis.
6. The energy wasted from the sides and bottom walls of the collector is negligible due to the presence of insulators.

4.3.1. Mathematical Model:

Using a steady-state setting, numerical calculations that are carried out with a commercially available COMSOL Multiphysics v5.5 program have been presented. The PDE-governed continuity, momentum, and energy equations have been solved for the turbulent, stationary, and incompressible flow. The fluid's heat transport is connected, and the pressure governing equation algorithm virtually automatically accounts for the effects of velocity and pressure. The Reynolds Averaged Navier

Stokes (RANS) model, which offers the flexibility of a set of equations utilized in the simulation based on the user's interest, is the model used to finish the simulation of the solar air heaters [48].

The continuity equation, represented by the **conservation of mass,** is given in terms of time-averaged incompressible flow:

$$\nabla V = 0 \qquad 4.1$$

Based on the principle of **momentum conservation**, for 2D steady-state turbulent flows, can write the RANS equations as [47]:

$$\rho\left(\bar{u}\frac{\partial\bar{u}}{\partial x}+\bar{v}\frac{\partial\bar{u}}{\partial y}\right)= F_x-\frac{\partial\bar{p}}{\partial x}+\mu\Delta\bar{u}-\rho\left(\frac{\partial\overline{\acute{u}\acute{u}}}{\partial x}+\frac{\partial\overline{\acute{u}\acute{v}}}{\partial y}\right) \qquad 4.2$$

$$\rho\left(\bar{u}\frac{\partial\bar{v}}{\partial x}+\bar{v}\frac{\partial\bar{v}}{\partial y}\right)= F_y-\frac{\partial\bar{p}}{\partial y}+\mu\Delta\bar{v}-\rho\left(\frac{\partial\overline{\acute{u}\acute{v}}}{\partial x}+\frac{\partial\overline{\acute{v}\acute{v}}}{\partial y}\right) \qquad 4.3$$

Where the volume force $\Delta\bar{u}$ is represented as [47]:

$$\Delta\bar{u}=\frac{\partial^2\bar{u}}{\partial x^2}+\frac{\partial^2\bar{u}}{\partial y^2} \qquad 4.4$$

$$\Delta\bar{v}=\frac{\partial^2\bar{v}}{\partial x^2}+\frac{\partial^2\bar{v}}{\partial y^2} \qquad 4.5$$

Based on the principle of **energy conservation**, for 2D steady-state turbulent flows, can write the RANS equations as:

$$\bar{u}\frac{\partial T}{\partial x}+\bar{v}\frac{\partial T}{\partial y}=\frac{\partial}{\partial x}\left(\Gamma_e\frac{\partial T}{\partial x}\right)+\frac{\partial}{\partial y}\left(\Gamma_e\frac{\partial T}{\partial y}\right) \qquad 4.6$$

4.3.2. The Standard (κ-ε) Turbulent Model:

The Reynolds stress tensor components produced by turbulent oscillations will be solved for using a specific method once the RANS turbulence model has been used. As the flow along the wall differs from that in the free stream section in turbulent flow, we should exercise caution. In this study, the *κ*- ε model is employed to shorten computation time while maintaining a reasonable level of accuracy. As a result, wall functions were used to define flow zones near walls [49]. The basic two equations *κ*-*ε* model with realizability constraints was used to model the impacts of turbulence for the DP-SAH with a U-turn. The turbulent kinetic energy (*κ*) and the turbulent dissipation rate (*ε*) were two dependent variables added to this model, along with two different transport equations. Models for the turbulent viscosity were:

$$\boldsymbol{\mu_T = \rho C_\mu \frac{\kappa^2}{\varepsilon}} \qquad \textbf{4. 7}$$

The transport equation for *κ* (turbulent kinetic energy) is [50]:

$$\boldsymbol{\rho(u.\nabla)\kappa = \nabla\left(\left(\mu + \frac{\mu_T}{\sigma_k}\right)\nabla\kappa\right) + P_\kappa - \rho\varepsilon} \qquad \textbf{4. 8}$$

Where, u is the velocity component in the x-direction, and the production term is:

$$\boldsymbol{P_\kappa = \mu_T\left(\nabla u: (\nabla u + (\nabla u)^T) - \frac{2}{3}(\nabla u)^2\right) - \frac{2}{3}\rho\kappa\nabla u} \qquad \textbf{4. 9}$$

The transport equation for ε (eddy dissipation rate) is [50]:

$$\boldsymbol{\rho(u.\nabla)\varepsilon = \nabla.\left(\left(\mu + \frac{\mu_T}{\sigma_k}\right)\nabla\varepsilon\right) + C_{\varepsilon 1}\frac{\varepsilon}{\kappa}P_\kappa - C_{\varepsilon 2}\rho\frac{\varepsilon^2}{\kappa}} \qquad \textbf{4. 10}$$

The coefficients for the set of equations from (4.7) to (4.10) were determined from experimental data [49]. These are C_μ=0.09, $C_{\varepsilon 1}$=1.44, $C_{\varepsilon 2}$=1.92, σ_κ=1.0, and σ_ε=1.3.

4.3.3. Boundary Conditions

The solution domain of the two-dimensions solar air heater (three models) is a rectangular duct on the x-y plane, in which the inlet, outlet, and walls are boundaries (as illustrated in figures (4.2), (4.4), and (4.7)), Only two dimensions were taken because the temperature distribution in the solar air heater is symmetrical around the third dimension, so the study was done in two dimensions only. The air and absorber plate aluminum properties are temperature dependent based on features built into the COMSOL CFD software. The DP-SAH system is assumed to have an ambient temperature of T_{amb}=25 °C, and glass cover, absorber plates and backplate ($T=T_{amb}$).

The boundary conditions for the whole system consist of

a) At heater cover, absorber plates, backplate and side edge walls: (u=v=0), no-slip condition.
b) Boundaries surfaces of the bottom and the side edges are assumed an insulated:

$$\frac{\partial T}{\partial n} = 0 \qquad 4.11$$

c) Inlet boundary conditions:

At the inlet duct of the first pass of the collector, the stream wise velocity is assumed to be fully developed flow with air MFR.

$$x = 0,\ 0 < y < h_{f1},\ T = T_{in} \qquad 4.12$$

d) Outlet boundary conditions

In the outlet section, a fully developed flow includes the set normal gradients to be zero, which can be written as:

$$\mathbf{x = 0,\ h_{f1} + h_p < y < h_{f2},\ \frac{\partial \emptyset}{\partial x} = 0} \qquad \mathbf{4.13}$$

Where: Ø is referred to the independent variables of: u, v, and T.

e) Solar radiation conditions

The upper surface of the aluminum plate:

$$\mathbf{0 \leq x \leq L, y = h_{f1}, I = 825\ W/m^2} \qquad \mathbf{4.14}$$

f) The pressure:

The inlet of the solar air heater:

$$\mathbf{P_1 = 101\ kPa} \qquad \mathbf{4.15}$$

4.3.4. Meshing and Solution Model:

Mesh generation on of the most critical factors that affect the accuracy of the results in any analysis and simulation process. The convergent solutions of the partial differential equations depend on generating a convenient mesh. In this simulation, Coarser mesh faces were used depending on the geometrical shape of the collector and operating condition, as shown clearly in figures (4.9), (4.10), and (4.11). Various tests were carried out to generate the grid with different size elements to achieve the best results to reach the stability of the temperature with the appropriate number of elements depending on the temperature of the outlet of air.

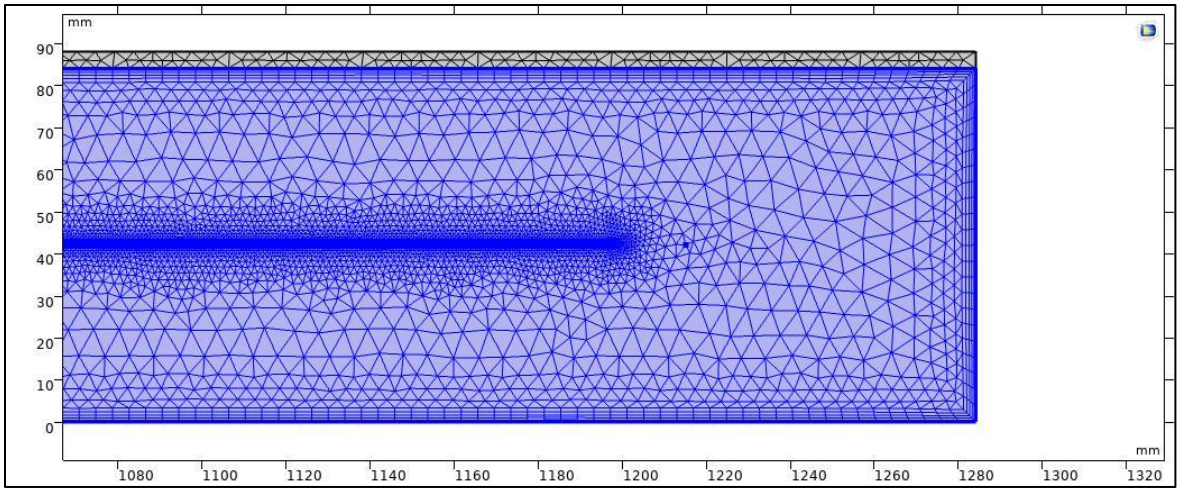

Figure 4. 9: Mesh generation for flat plate DP-SAH.

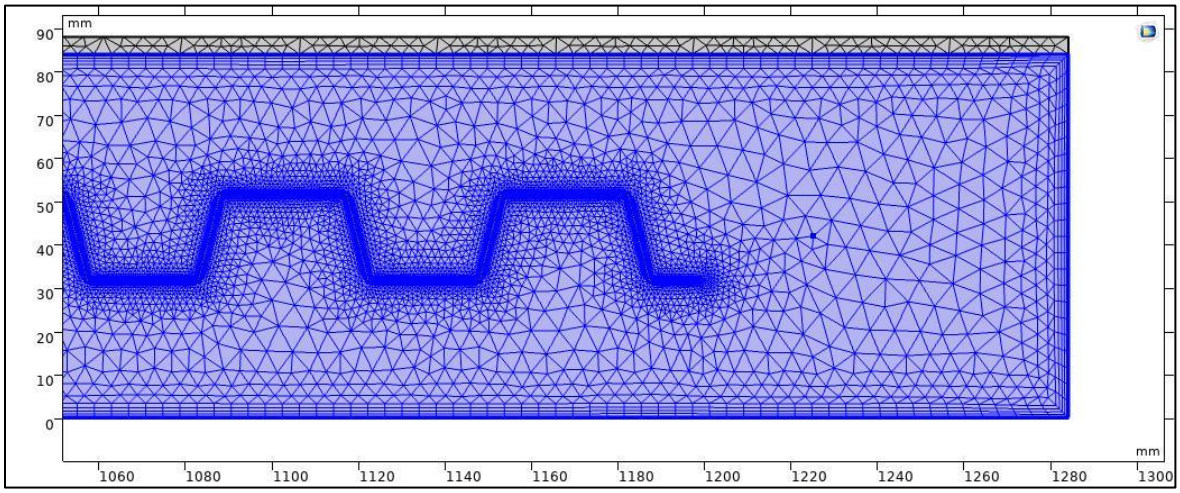

Figure 4. 10: Mesh generation for trapezoidal plate DP-SAH.

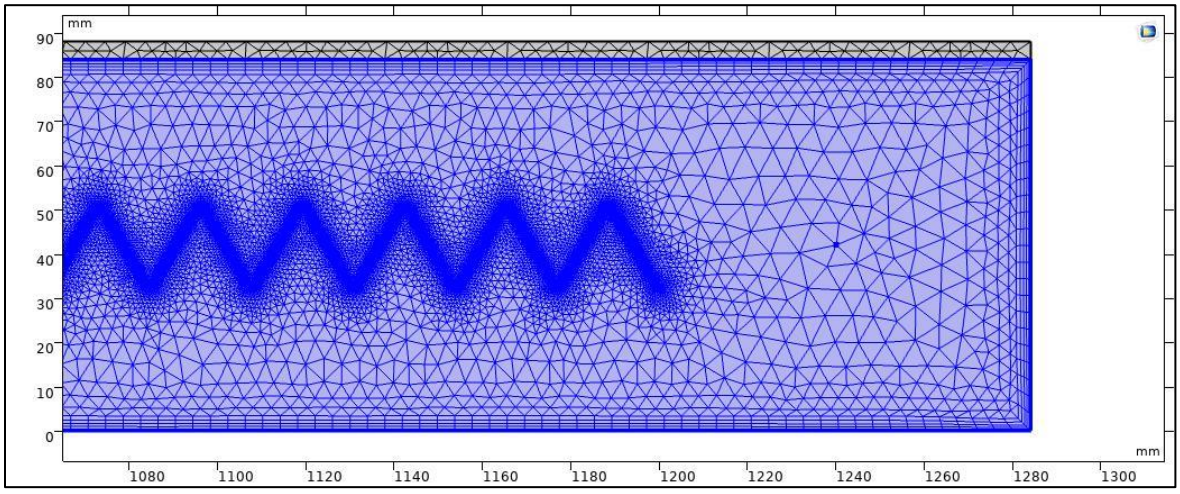

Figure 4. 11: Mesh generation for V-groove plate DP-SAH.

4.3.5. Flow chart of numerical analysis:

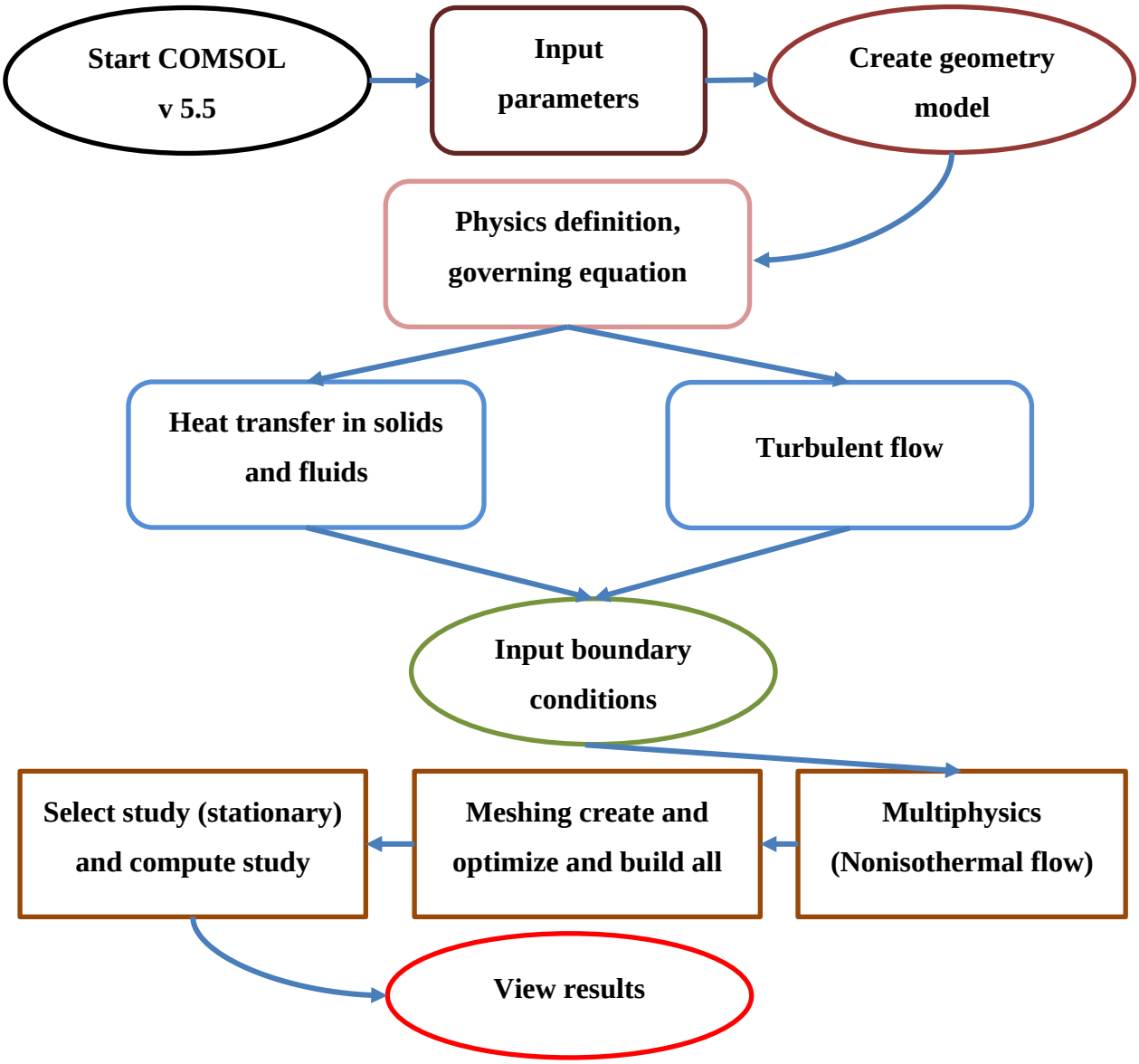

4.4. Analysis of Thermal Performance (Data Redaction):

A thermodynamics analysis is performed to determine the total performance and the direction of energy transfer across a mechanical system. The divaricate ideas of thermodynamics are represented by energy and exergy. A system's exergy is the higher probable useful work through a process that turns the system into a thermal

equilibrium ultimately. Exergy, then, is the capacity of energy to do productive work as a system reaches equilibrium. Reliance on a thermodynamic strategy from the first and second laws' perspectives. Therefore, energy and exergy analyses –known as the first and second laws – are produced to study the DP-SAH system effectively [51-54].

4.4.1. Energy Analysis:

SAH's energy analysis is expressed in terms of the first law of thermodynamics. The energy gain rate of SAH is found as [54]:

$$\dot{Q}_u = \dot{m} c_p (T_{out} - T_{in}) \quad \textbf{4.16}$$

The rate of solar energy absorption is calculated as follows [54]:

$$\dot{Q}_{abs} = A_c I \quad \textbf{4.17}$$

The total rate of energy transfer from the collector to the surrounding environment by conduction, convection, and radiation is known as the lost energy rate, and it can be computed as follows [54]:

$$\dot{Q}_L = U_L A_c (T_{abs} - T_a) \quad \textbf{4.18}$$

Heat losses from the solar air heater to the surrounding occurred by all three heat transfer mechanisms. The overall heat loss coefficient of SAH can be defined by [54]:

$$U_L = U_b + U_e + U_t \quad \textbf{4.19}$$

Bottom and edge heat loss coefficients (U_b and U_e) are neglected, and the top heat transfer coefficient from the SAH could be defined as [55]:

$$U_t = h_w + h_r \quad \textbf{4.20}$$

Convective heat transfer, which occurs by wind, could be obtained by using the following equation [55]:

$$\boldsymbol{h_w = 2.8 + 3V \quad for \quad 0 \leq V \leq 7\ m/s} \qquad \textbf{4.21}$$

The radiation heat transfer coefficient that occurs between the solar air heater transparent cover and surrounding could be calculated by the equation [55]:

$$\boldsymbol{h_r = \sigma\varepsilon\left(T_{abs} - T_g\right)\left(T_{abs}^2 + T_g^2\right)\left(\frac{(T_g - T_s)}{(T_g - T_a)}\right)} \qquad \textbf{4.22}$$

Depending on the absorber's temperature and the wind's convective impact over the glass cover, the glass cover experiences the maximum amount of power loss among these components.

Since we recorded the experimental data for steady-state case, the equation (4.16) is written as [55]:

$$\boldsymbol{\dot{Q}_u = \dot{Q}_{abs} - \dot{Q}_L} \qquad \textbf{4.23}$$

The thermal efficiency of solar air heater, η is found by dividing the energy gain rate of solar air heater defined by equation (4.23) by the rate of solar energy absorption determined by equation (4.17) as [55]:

$$\boldsymbol{\eta = \frac{\dot{Q}_u}{\dot{Q}_{abs}}} \qquad \textbf{4.24}$$

Reynolds number (Re) for the flow within the air duct has been written as [55]:

$$\boldsymbol{Re = \frac{\rho V D_h}{\mu}} \qquad \textbf{4.25}$$

The all-thermos physical properties of the air in the duct are evaluated at the mean temperature of T_m is [55]:

$$T_m = \frac{T_{in}+T_{out}}{2} \qquad 4.26$$

The control volume of energy analysis for solar air heater shown in figure (4.12).

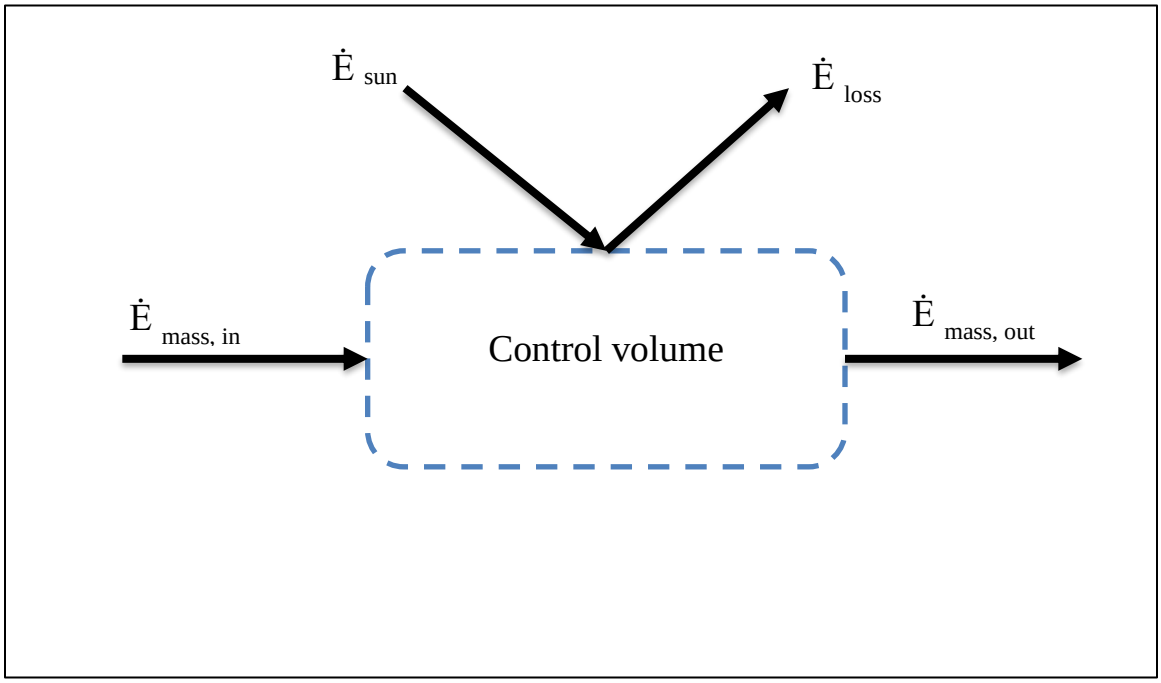

Figure 4. 12: Energy analysis for solar air heater.

4.4.2. Exergy Analysis:

An increase in the exergy in the fluid flow during passage through the SAH is called an exergy gain. Exergy analysis is performed similarly to energy analysis. Considering the SAH and heat collector as one control volume, assuming the steady-state condition the exergy gain (Ex_{out}), is computed by using the following equation [53]:

$$\dot{E}x_{out} = \dot{m}c_p\left(T_{out} - T_{in} - T_a \ln\left(\frac{T_{out}}{T_{in}}\right)\right) - \left(\frac{\dot{m}}{\rho}\right)\Delta P\left(\frac{T_a}{T_m}\right) \qquad 4.27$$

The exergy heat is computed by using the following equation [53]:

$$\dot{E}x_{in} = \left(1 - \frac{T_a}{T_s}\right)\dot{Q}_{abs} \qquad 4.28$$

The exergy efficiency of a solar air heater can be as follows [53]:

$$\eta_{ex} = \frac{\dot{E}x_{out}}{\dot{E}x_{in}} \qquad 4.29$$

The control volume of exergy analysis for solar air heater shown in figure (4.13).

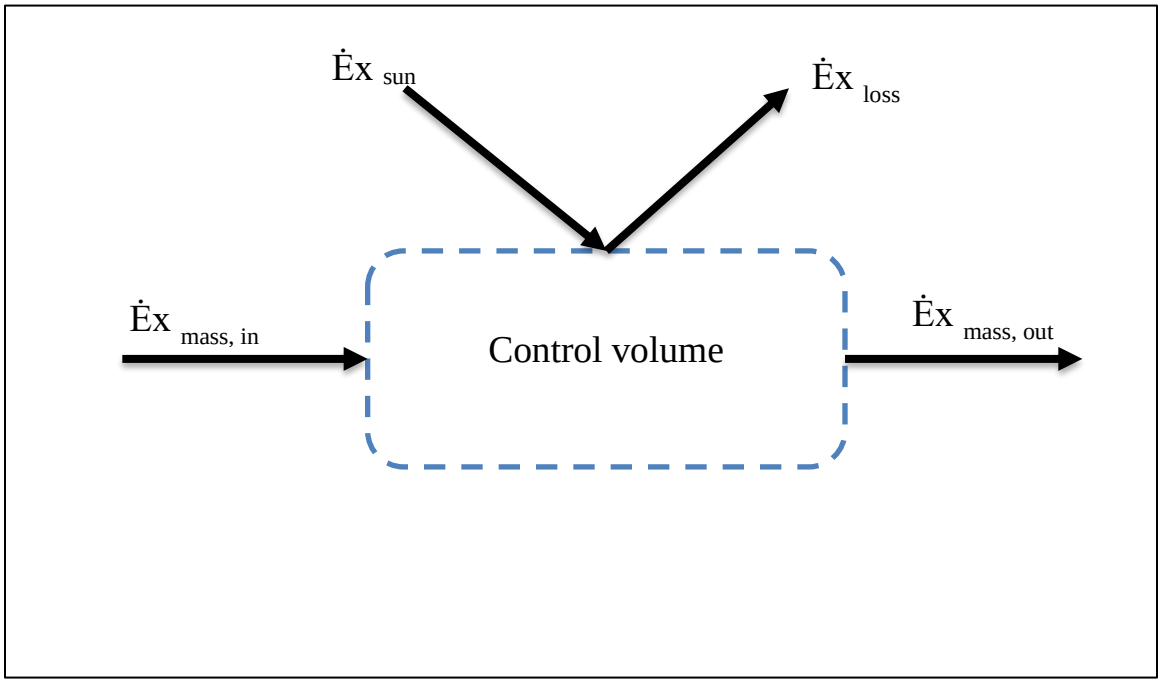

Figure 4. 13: Exergy analysis for solar air heater.

4.5.Error Analysis:

Our current work was done on the practical and theoretical sides together. To verify the validity of the numerical results against the experimental results, we calculate the error percentage between them and compare them with previous researchers. So, to estimate the error percentage, the following law was used [56]:

$$error\ ratio = \frac{NUM-EXP}{NUM} \times 100\% \qquad 4.30$$

Chapter Five

Results and Discussion

Chapter Five

Results and Discussion

5.1.Introduction:

The results obtained from the experimental data and numerical analysis are presented. The results are studied under the influence of constant solar radiation of (825 W/m^2) and variable air MFR ranging from 0.6 to 2.4 kg/min to study the thermal fluid behaviours of forced convection turbulent flow in the DP-SAH with three different models (flat, trapezoidal, and V-groove plate). Furthermore, validation of the results by the comparison between numerical analysis and experimental readings. Finally, a comparison was presented between the current mathematical model and previous studies.

5.2.Experimental Study Results:

To validate the performance of DP-SAH, experiments were conducted in a controlled indoor environment with a constant wind speed of 1.5 m/s and a room temperature of (24 – 26) ◦C, utilizing three types of absorber plates: flat, trapezoidal, and V-groove plates. Various air MFRs (0.6, 1.2, 1.8, and 2.4 kg/min) and a constant mean solar radiation of 825 W/m^2 were utilized in this study.

5.2.1. The Effect of Air Mass Flow Rate on Collector Temperatures:

Figures (5.1), (5.2), and (5.3) represent the effect of air MFR on mean temperatures of a double-pass solar air collector with constant solar radiation of 825 W/m^2 for three models of the absorbent plate (flat, trapezoidal, and V-groove). These

figures show the mean temperatures of the glass, absorption plate, the air in the first and second passages, and the background. It can be observed from experimental tests a decrease in the temperature curves when the air MFR increases, because when the airflow speed in the solar air heater is increased, the period for heat gain from solar radiation decreases; therefore, temperatures drop as the mass flow rate increases at the same solar radiation. The temperature behavior of the glass, the absorbent plate and the back plate only will be discussed in figures (5.1), (5.2), and (5.3). The temperature behavior of the air path will be explained in the following paragraphs of this chapter.

5.2.1.1. Temperatures of the Absorbent Plates:

We note that the temperature of the absorbent plate is the highest temperature value in the double-pass solar air collector of all three models. The temperature of the flat, trapezoidal and V-groove plate of (52.5) °C, (53.23) °C, and (56.967) °C, respectively, at an air MFR ranging between (0.6-2.4) kg/min. Thus, the highest temperature value will be for the V-grooved type plate compared to the other two types, followed by the trapezoidal plate and the flat plate, because V-groove has a larger area of absorber plate and shape of geometry causes more turbulence, as shown in figures (5.1), (5.2), and (5.3).

5.2.1.2. Temperatures of the Glass Cover:

The figures (5.1), (5.2), and (5.3) also show that the glass temperature is lower than the absorbent plate and higher than the air temperature in the first and second passages and the background. Still, at the solar collector in the presence of the plate with a v-groove, the temperature of the glass becomes lower than the air temperature

in the second passage when the MFR of air is at 2.4 kg/min. The glass temperature of DP-SAH with the flat, trapezoidal and V-groove plate of (47.9) °C, (45.8) °C, and (49.7) °C, respectively, at an air MFR ranging between (0.6-2.4) kg/min.

5.2.1.3. Temperatures of the Background Plates:

In the end, the background is the third solid part of the system. It has the lowest temperatures compared to the absorbent plate and glass, where the temperature ranges of it in DP-SAH with the flat, trapezoidal and V-groove plate ranges between (23.5) °C, (26.5) °C, and (26.4) °C, respectively, at an air MFR ranging between (0.6-2.4) kg/min.

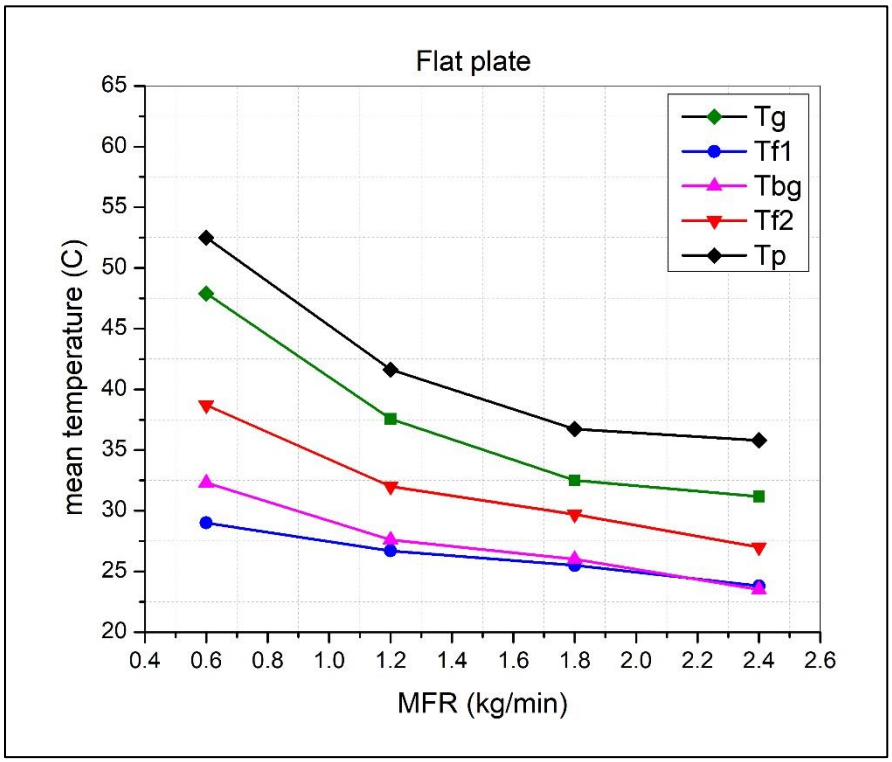

Figure 5. 1: Variation the average temperature in the double-pass solar air heater at Flat plate with MFR of air.

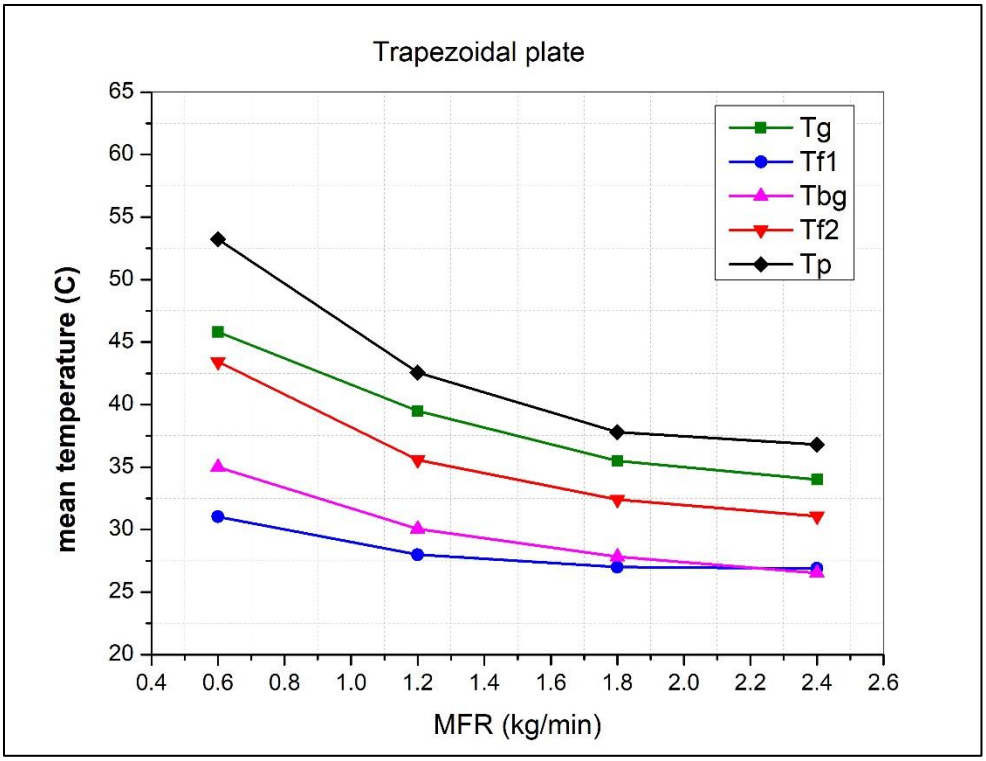

Figure 5. 2: Variation the average temperature in the double-pass solar air heater at Trapezoidal plate with MFR of air.

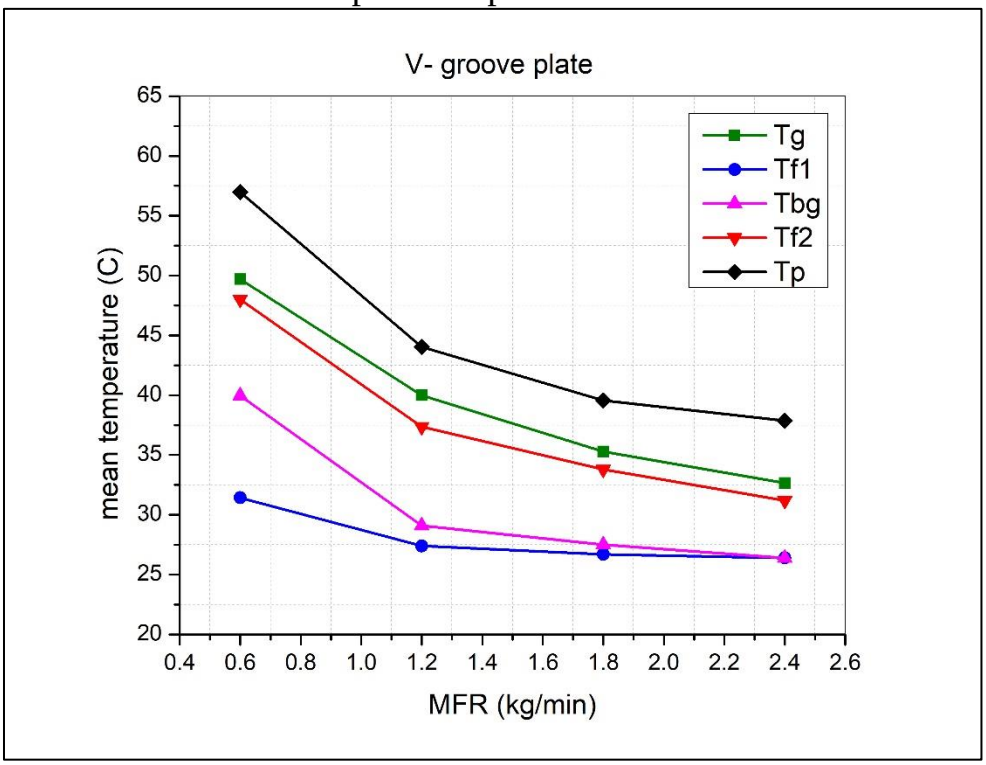

Figure 5. 3: Variation the average temperature in the double-pass solar air heater at V-groove plate with MFR of air.

5.2.2. The Distribution of Temperatures with the Length of the Solar Collector:

The figures (5.4) to (5.15) show the temperatures relative to the length of the collector, where the temperature was measured for the solid parts and air in the two passages at several points located at dimensions of 330, 660, and 990 mm, with constant solar radiation as well as the air MFR. The experiment was repeated with the change of the air MFR 4 times to be at (0.6, 1.2, 1.8, and 2.4) for each model of absorbent plates (flat, trapezoidal, and V-groove).

5.2.2.1. Flat Absorber Plate

Figures (5.4) to (5.7) show the temperatures of the flat plate, the temperature, in general, begins to decrease as the MFR of air to be heated increases. In these figures, show that the temperature of the absorbent plate is (52.8, 54.6, and 50.1) °C at a MFR of 0.6 kg/min, (41.8, 43.3, and 39.8) °C at a MFR of 1.2 kg/min, (37.1, 38.2, and 34.9) °C at an MFR of 1.8 kg/min, and (36.1, 37.1, and 34.2) °C at an MFR of 2.4 kg/min, where the temperature is measured at the dimensions (330, 660, and 990) mm, respectively. Thus, the highest temperature value is in the middle of all air MFR values for absorber plate. Thus, the flat absorbent plate's temperature ranges from (34.2 – 52.8) °C.

In the same figures mentioned above, show that the temperature of the glass is (47.9, 49.8, and 46) °C at an MFR of 0.6 kg/min, (37, 39.1, and 36.6) °C at an MFR of 1.2 kg/min, (32.7, 34.3, and 30.5) °C at an MFR of 1.8 kg/min, and (30.6, 32.7, and 30.2) °C at an MFR of 2.4 kg/min, where the temperature is measured at the dimensions (330, 660, and 990) mm, respectively. Thus, the highest temperature value is in the middle of all air MFR values for glass cover. Thus, the glass temperature ranges from (30.2 – 49.8) °C.

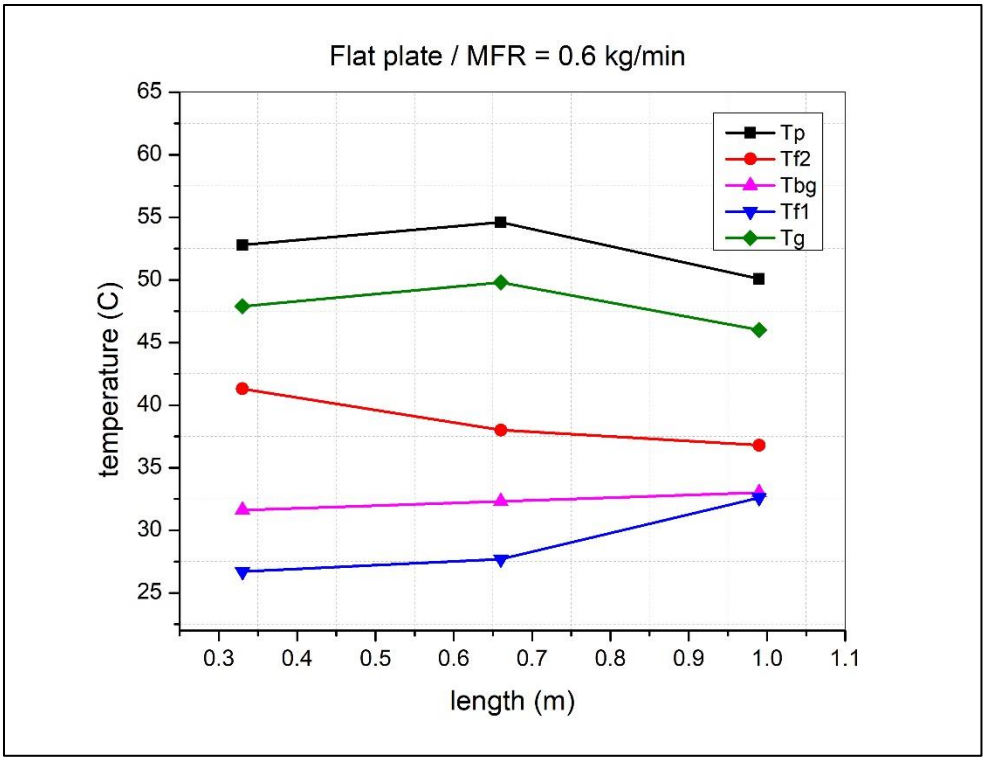

Figure 5. 4: The temperature along the length of the flat plate DP-SAH with solar radiation of 825 W/m^2 and a air MFR of 0.6 kg/min.

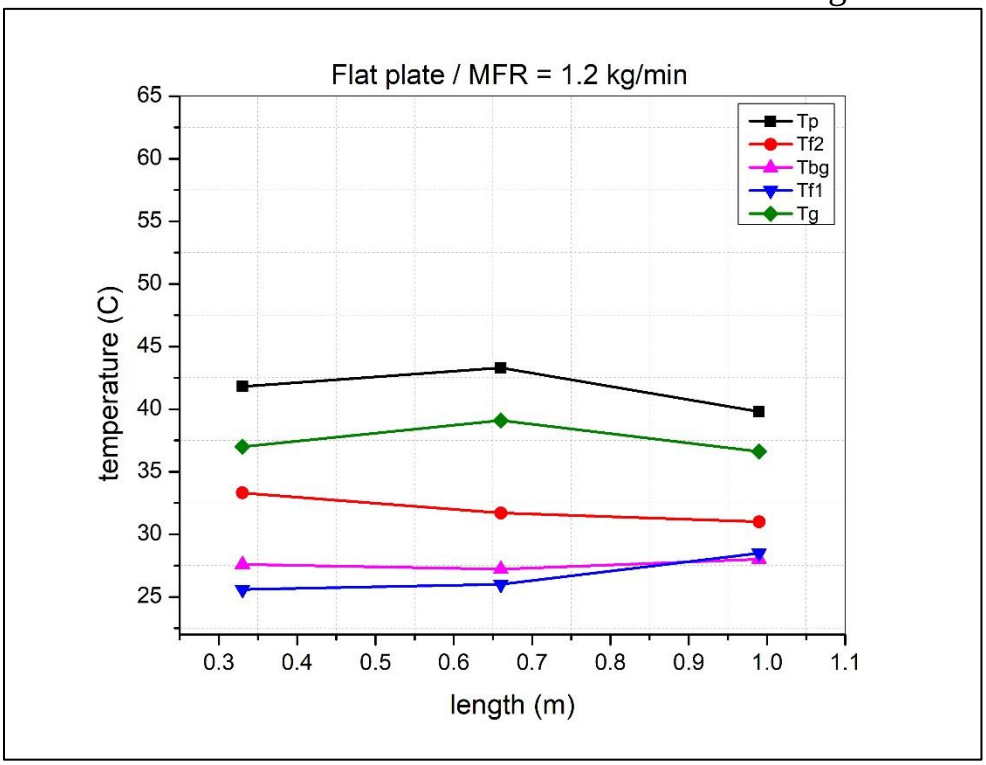

Figure 5. 5: The temperature along the length of the flat plate DP-SAH with solar radiation of 825 W/m^2 and a air MFR of 1.2 kg/min.

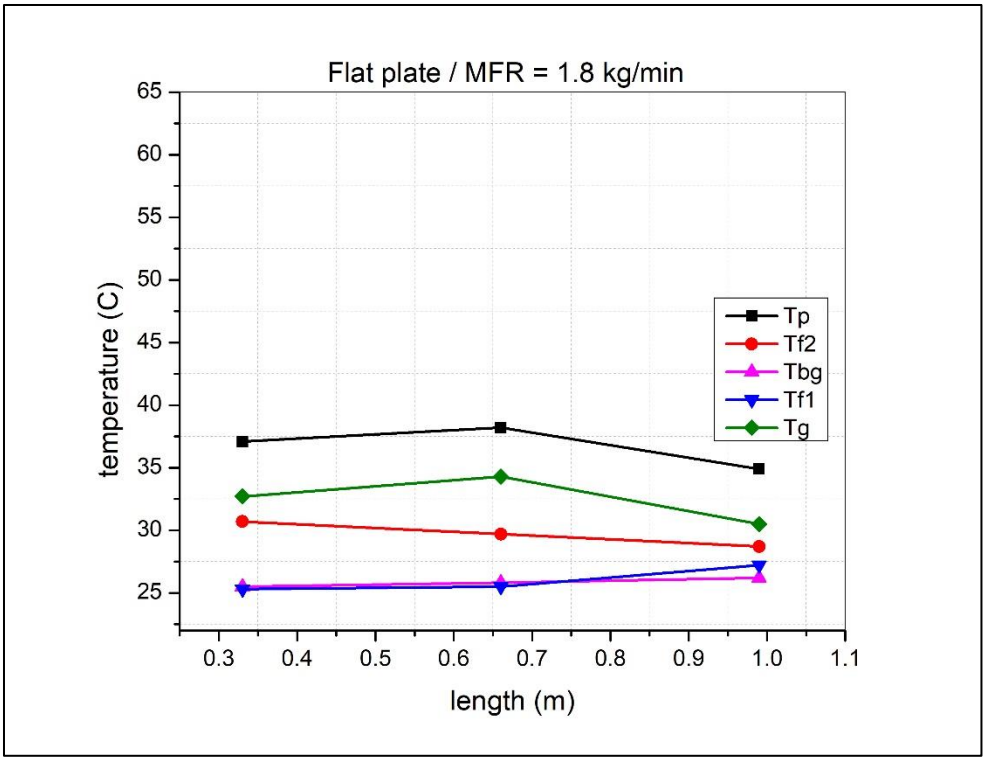

Figure 5. 6: The temperature along the length of the flat plate DP-SAH with solar irradiation of 825 W/m^2 and a air MFR of 1.8 kg/min.

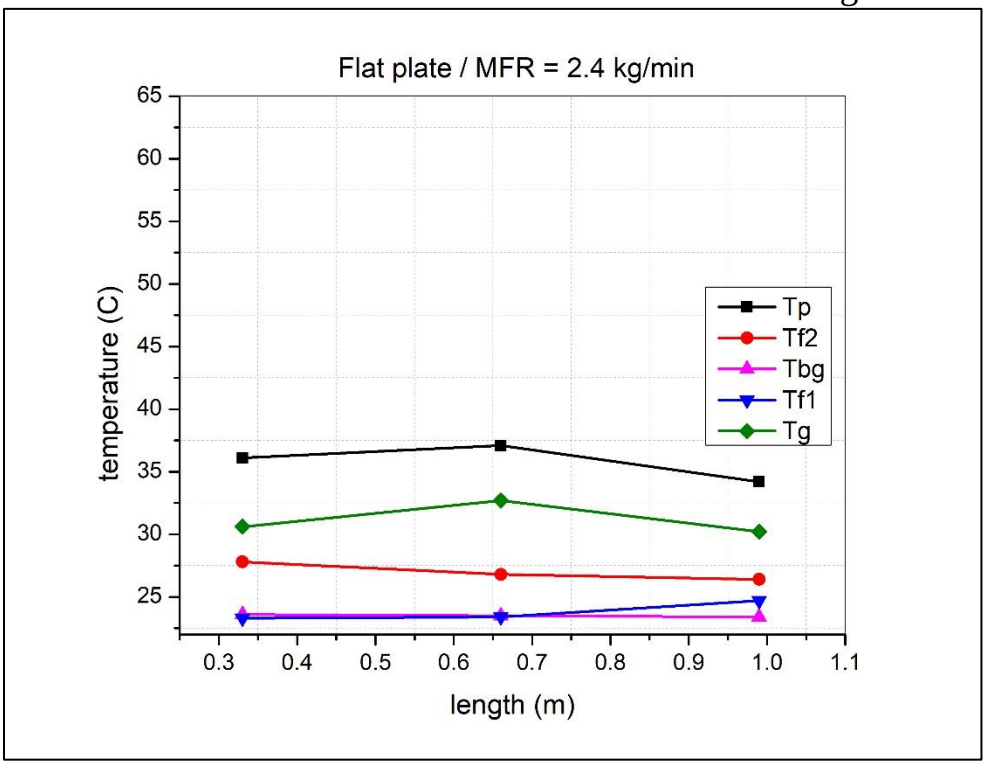

Figure 5. 7: The temperature along the length of the flat plate DP-SAH with solar radiation of 825 W/m^2 and a air MFR of 2.4 kg/min.

5.2.2.2. Trapezoidal Absorber Plate:

The temperatures of the trapezoidal plate are shown in figures (5.8) to (5.11), and show that they generally start to decline as the MFR of heated air increases. Observing these statistics, present that the temperature of the absorbent plate is (53.3, 55.7, and 50.7) °C at an MFR of 0.6 kg/min, (42.8, 43.8, and 41.1) °C at an MFR of 1.2 kg/min, (37.9, 38.7, and 36.8) °C at an MFR of 1.8 kg/min, and (36.8, 37.7, and 35.9) °C at an MFR of 2.4 kg/min, where the temperature is measured at the dimensions (330, 660, and 990) mm, respectively. So, the maximum temperature value is in the center among all values of air MFR for absorber plate. As a result, the temperature of the trapezoidal absorbent plate varies between (35.9 – 55.7) °C.

In the same data which was described previously that the glass reaches temperatures of (47, 47.6, and 42.8) °C at an MFR of 0.6 kg/min, (40, 42, and 36.5) °C at an MFR of 1.2 kg/min, (34.8, 38, and 33.7) °C at an MFR of 1.8 kg/min, and (34.5, 35, and 32.5) °C at an MFR of 2.4 kg/min, where the temperature is measured at the dimensions (330, 660, and 990) mm, respectively. So, the maximum temperature value is in the center among all values of air MFR for glass cover. As a result, the glass temperature is (32.5 – 47.6) °C.

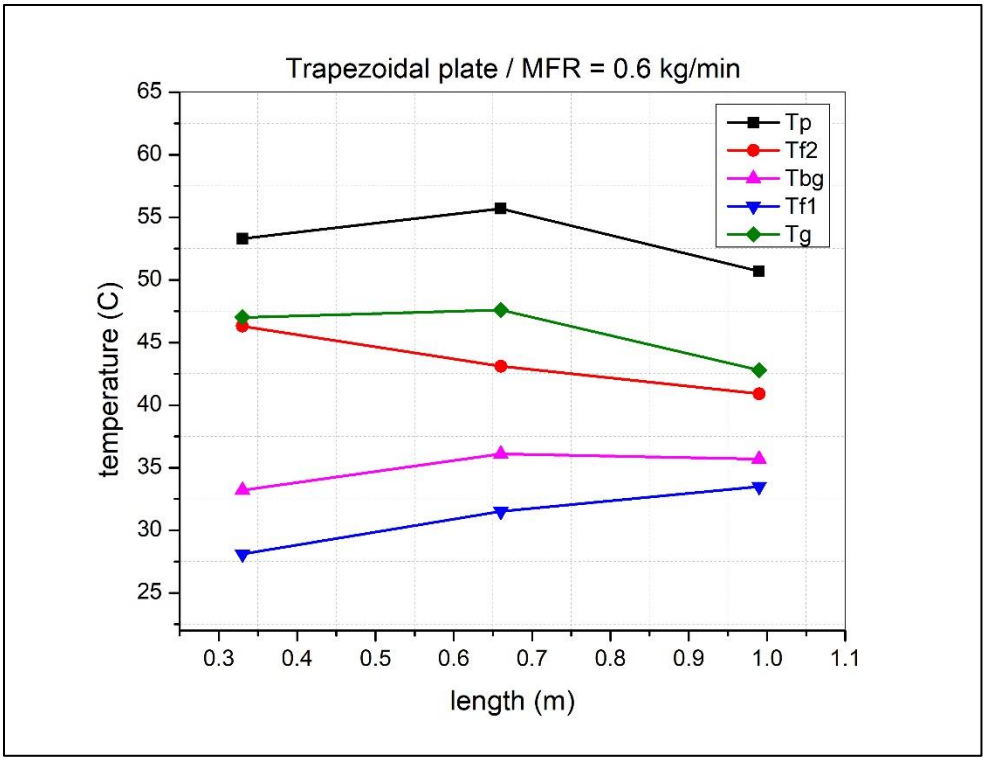

Figure 5. 8: The temperature along the length of the trapezoidal plate DP-SAH with solar radiation of 825 W/m^2 and a air MFR of 0.6 kg/min.

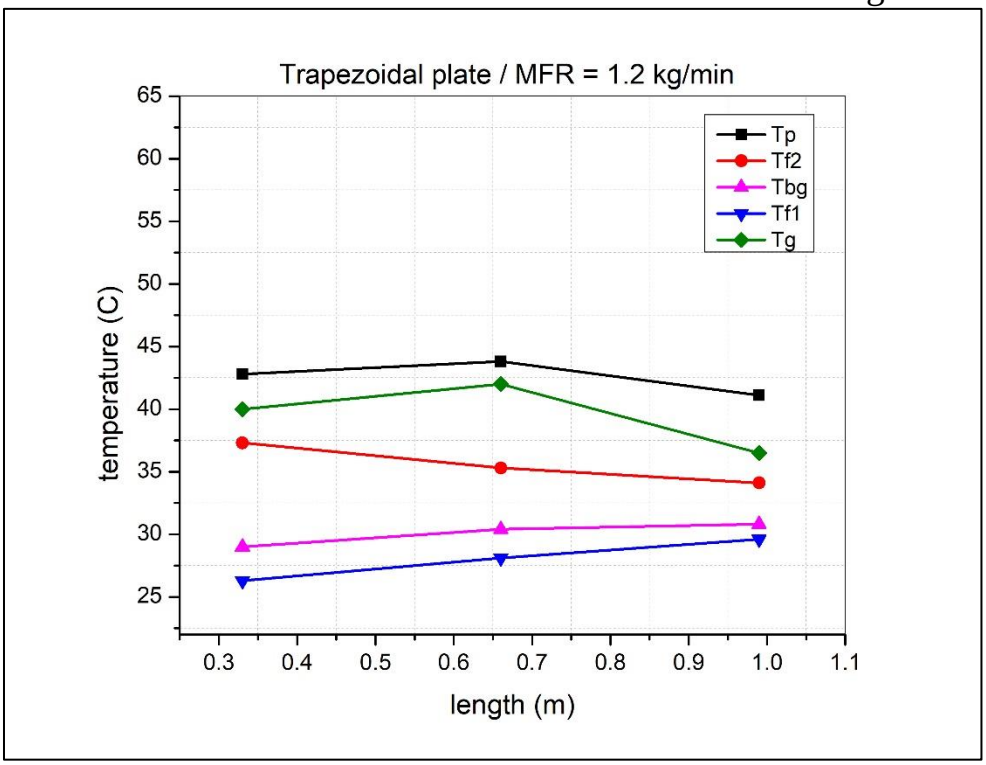

Figure 5. 9: The temperature along the length of the trapezoidal plate DP-SAH with solar radiation of 825 W/m^2 and a air MFR of 1.2 kg/min.

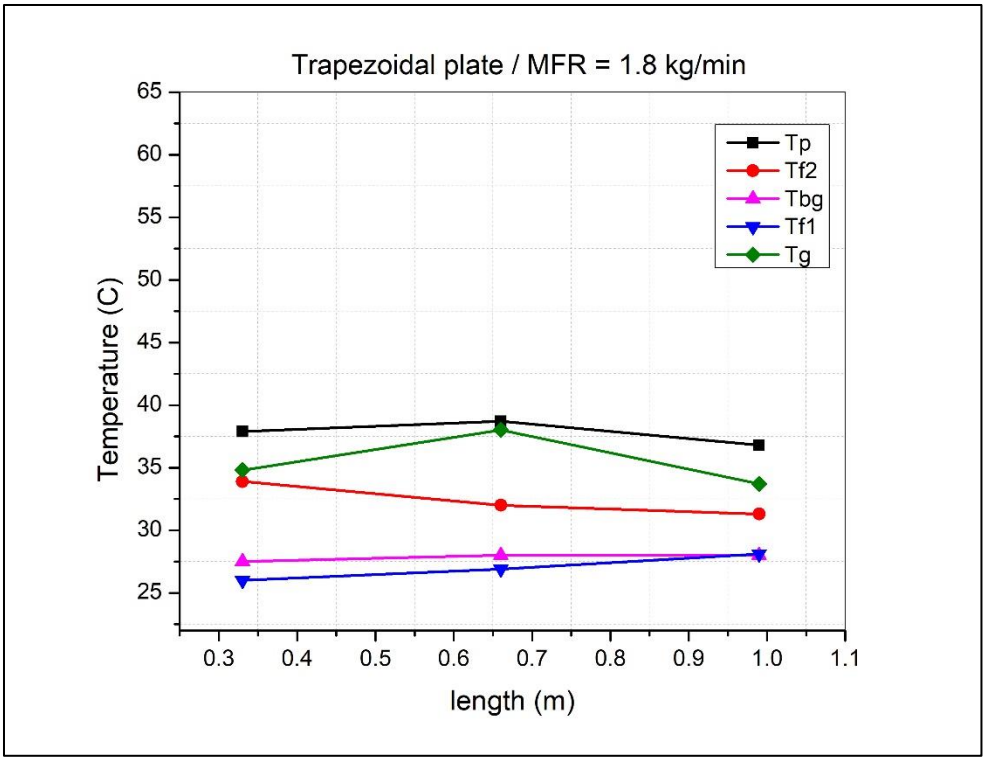

Figure 5. 10: The temperature along the length of the trapezoidal plate DP-SAH with solar irradiation of 825 W/m^2 and a air MFR of 1.8 kg/min.

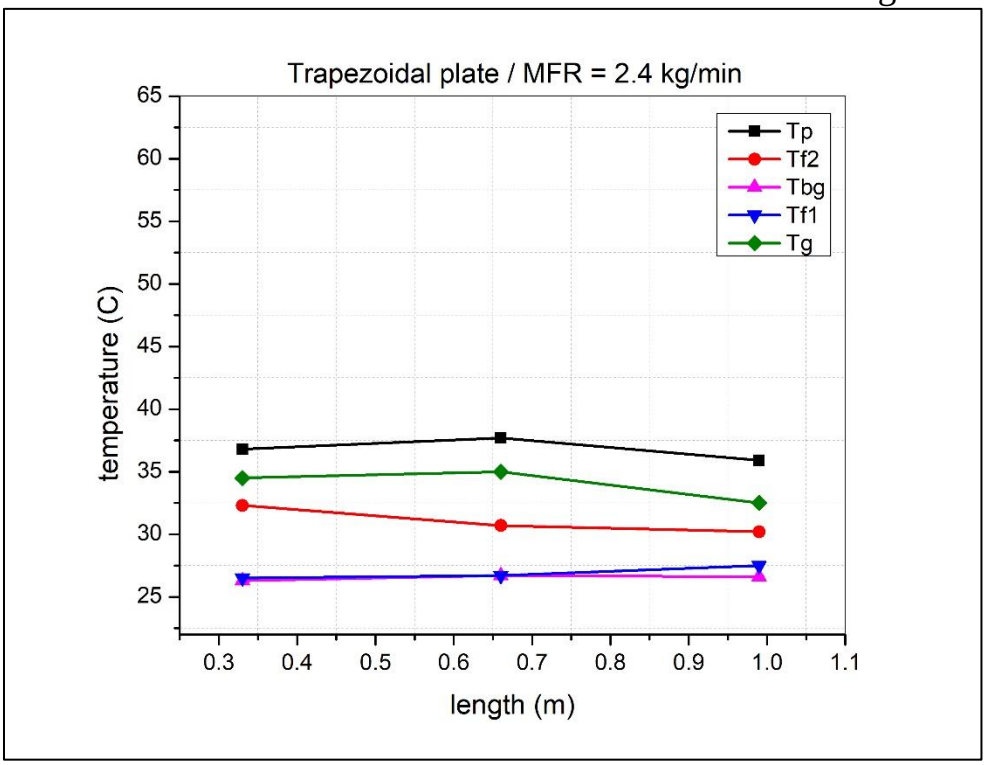

Figure 5. 11: The temperature along the length of the trapezoidal plate DP-SAH with solar irradiation of 825 W/m^2 and a air MFR of 2.4 kg/min.

5.2.2.3. V-Groove Absorber Plate:

Figures (5.12) to (5.15) depict the temperatures of the V- groove plate, and they generally begin to decrease as heating the MFR of air rises. With the aid of these statistics, we can determine that the temperature of the absorbent plate is (56.3, 58.9, and 55.7) °C at an MFR of 0.6 kg/min, (43.7, 45, and 43.4) °C at an MFR of 1.2 kg/min, (39.4, 40.2, and 39.1) °C at an MFR of 1.8 kg/min, and (37.7, 38.4, and 37.5) °C at an MFR of 2.4 kg/min, where the temperature is measured at the dimensions (330, 660, and 990) mm, respectively. Therefore, the maximum temperature value is in the middle of all air MFR values for absorber plate. As a result, the V-groove absorbent plate's temperature ranges from (37.5 – 58.9) °C.

The same data that was previously described shows that the glass temperature reaches (50.9, 51.4, and 46.8) °C at an MFR of 0.6 kg/min, (40.5, 41.3, and 38.2) °C at an MFR of 1.2 kg/min, (36, 36.5, and 33.4) °C at an MFR of 1.8 kg/min, and (33, 33.5, and 31.5) °C at an MFR of 2.4 kg/min, where the temperature is measured at the dimensions (330, 660, and 990) mm, respectively. Therefore, the maximum temperature value is in the middle for all air MFR for glass cover. Thus, the glass temperature ranges from (31.5 – 50.9) °C.

From what was presented in the previous paragraphs, the following is clear:

- The temperature is as high as possible in the middle of the background, the glass cover, and the absorbent plate because the radiation is concentrated in the middle and decreases at the edges, as shown in Figure (3.9) in the third chapter.

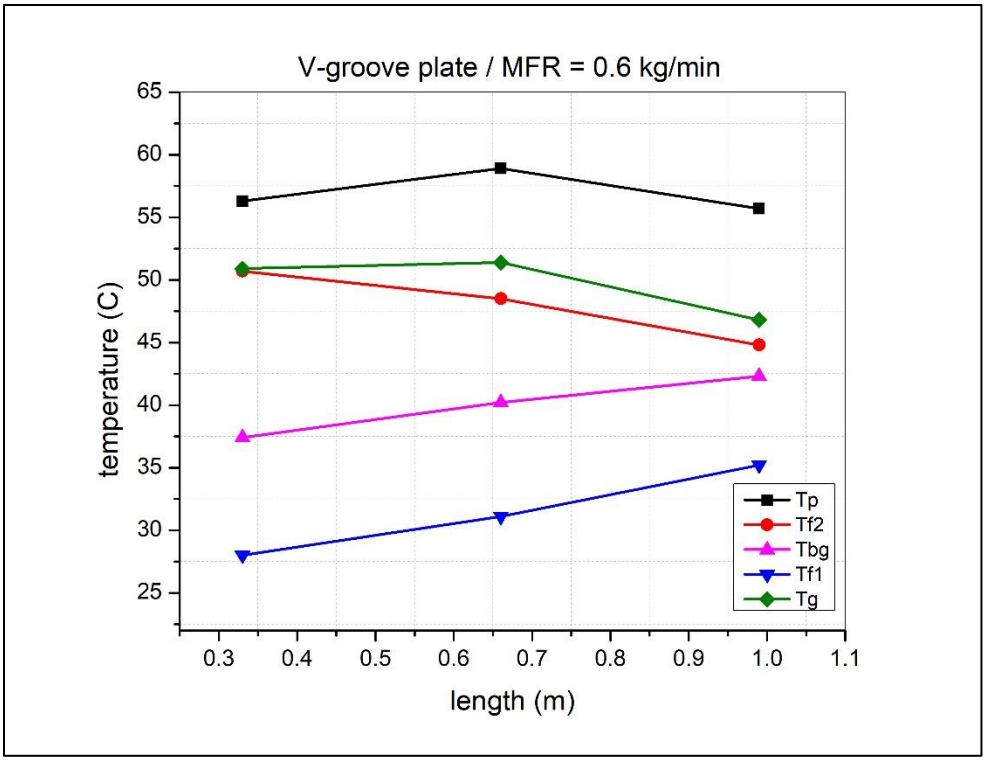

Figure 5. 12: The temperature along the length of the V-groove plate DP-SAH with solar radiation of 825 W/m^2 and a air MFR of 0.6 kg/min.

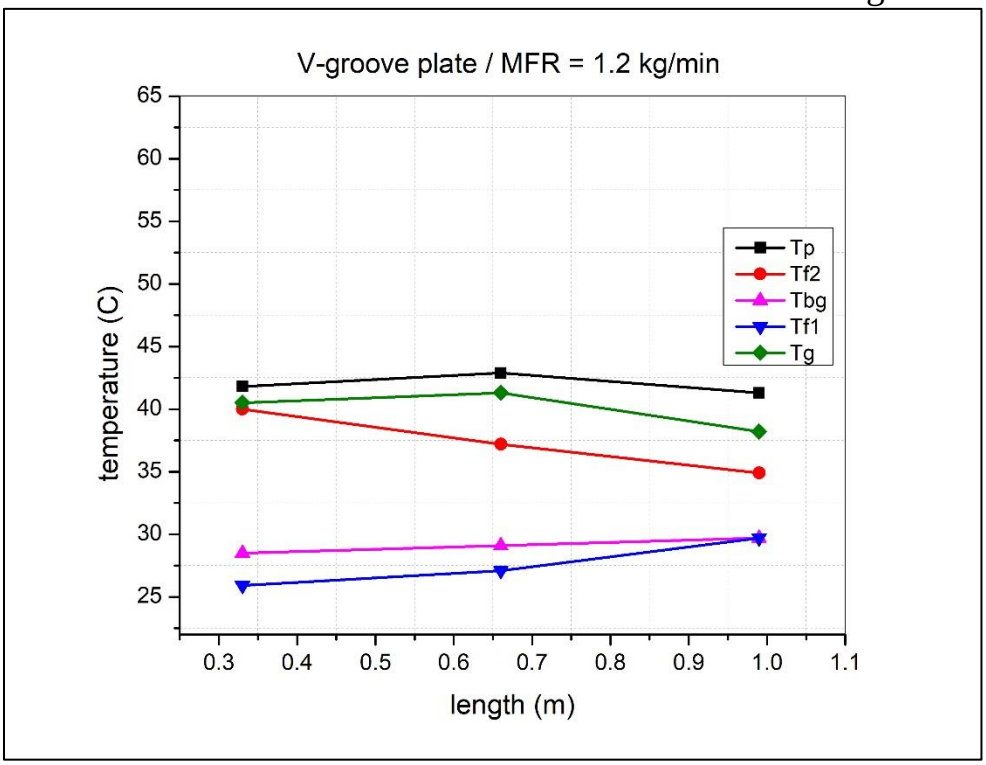

Figure 5. 13: The temperature along the length of the V-groove plate DP-SAH with solar radiation of 825 W/m^2 and a air MFR of 1.2 kg/min.

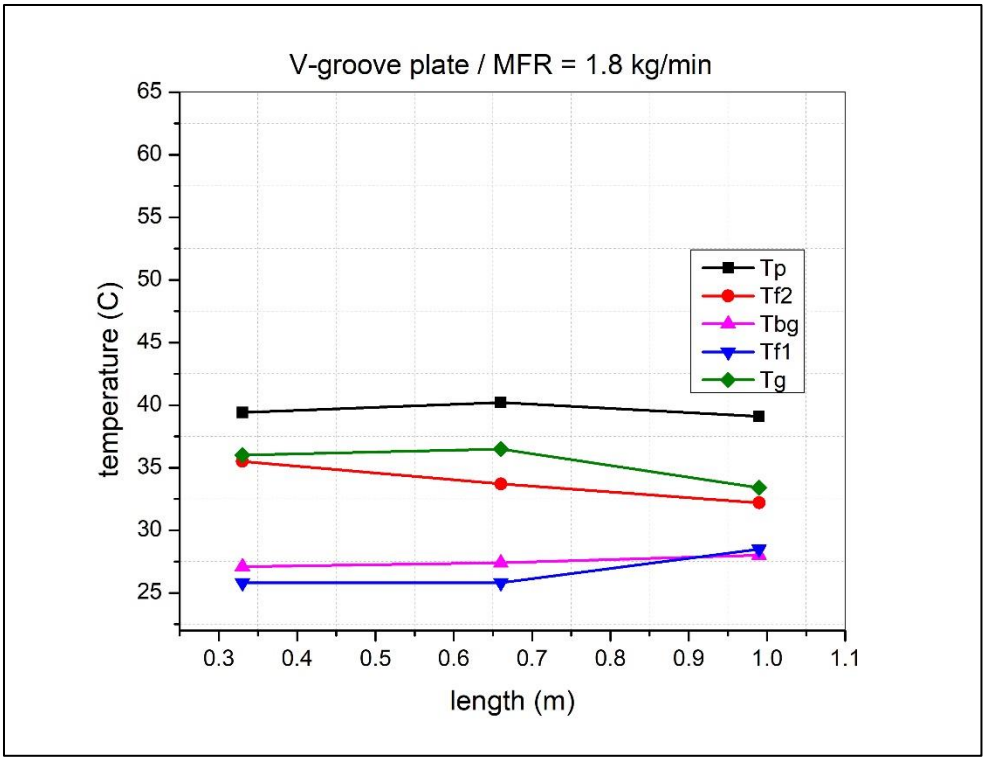

Figure 5. 14: The temperature along the length of the V-groove plate DP-SAH with solar irradiation of 825 W/m^2 and a air MFR of 1.8 kg/min.

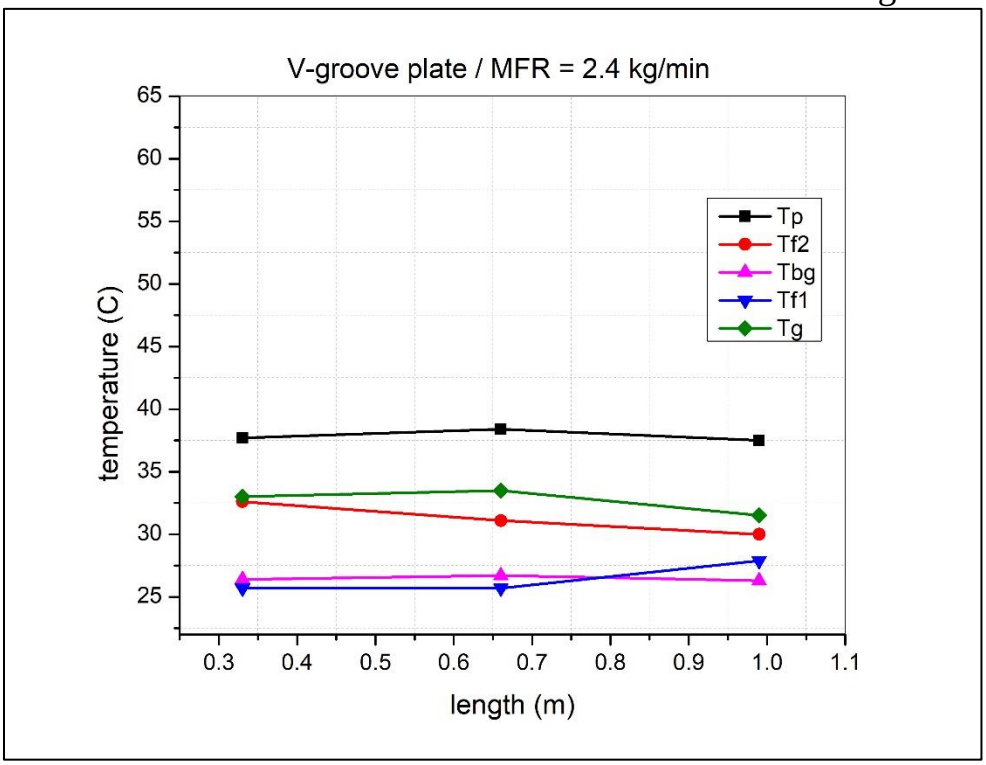

Figure 5. 15: The temperature along the length of the V-groove plate DP-SAH with solar radiation of 825 W/m^2 and a air MFR of 2.4 kg/min.

- The temperatures of the back plate, the glass and the absorbent plate decrease with the increase in the mass flow rate of the air. So, the highest temperatures are when the mass flow rate of air is 0.6 kg/min, and the lowest possible when the mass flow rate of air is 2.4 kg/min.
- Through what was previously shown for the absorbent plates, it was found that the V-groove plate has the highest temperature, followed by the trapezoidal plate and then the flat plate. This is due to the area used in manufacturing each plate and the geometry shape, which also causes turbulence in the airflow.
- The temperature of the background and the glass is affected by the temperature of the absorbent plate with a direct relationship between them so that the temperatures of the glass and the background increase in the V-groove and trapezoidal plates.
- In some results, the air temperature in the first passage is identical to or higher than that of the background. This is because the air gains heat from the background and the absorbent plate, starting from the entry point until reaching the circulation point (U-turn).

5.2.3. Temperature Variation of The Airflow Along the first and second Passage:

Figures (5.16) to (5.18) appear the temperature variation of the airflow along the first and second passage with the presence of a flat, trapezoidal, and V-groove absorption plate for different air MFRs (0.6, 1.2, 1.8, and 2.4) kg/min and under constant solar radiation of 825 W/m^2. The air flows in the first pass between the absorbent plate and the background and then is recycled towards the second pass between the glass cover and the absorbent plate.

In general, all the temperature curves increase gradually from the input to the output of the collector. Still, the temperature of the exiting air in the collector with a v-groove absorption plate is higher compared to the collectors with flat and trapezoidal plates. It can be attributed to the fact that the v-groove absorption plate has a large area than other plates and creates more turbulence than others, thus increasing the heat transfer area and becoming more effective.

Also, it noted that increasing the air MFR led to a decrease in the temperature of the outside air in the collector at the same solar radiation. This heat exchange behavior is explained by the shorter airflow period over the hot absorber plate inside the solar air heater at a larger MFR of air through DP-SAH.

At (0.6, 1.2, 1.8, and 2.4) kg/min, the output temperature of the flat plate reaches (41.2, 34.1, 31.6, and 28.3) °C, respectively. As for the trapezoidal plate, the outlet temperature reaches (47.2, 38.5, 34.7, and 33.3) °C, respectively. Finally, the plate with a V-groove, so the outlet temperature reaches (51.8, 39.9, 35.9, and 33.9) °C, respectively. Thus, the highest temperature of the outlet was obtained when using the plate with a V-groove at 0.6 kg/min for MFR.

In experiments, the entry temperature varies between (24-26) C; in some experiments, it is less than this limit, as it cannot be controlled entirely.

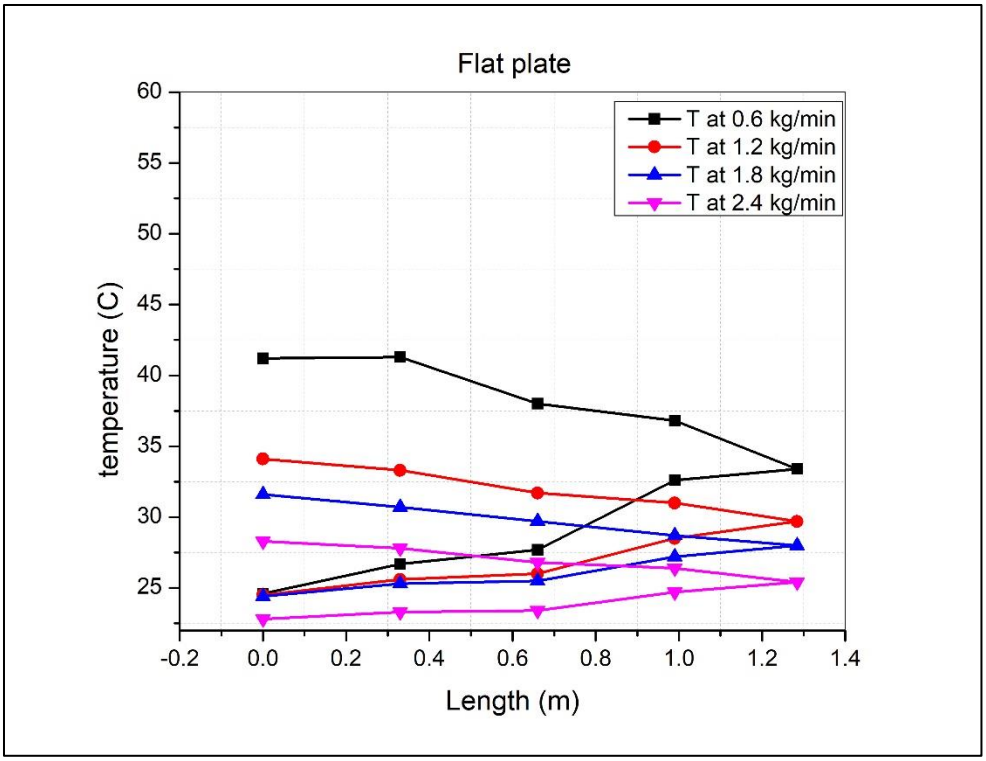

Figure 5. 16: The effect of MFR on the temperature of the airflow in the SAH at the inlet, first-pass, second-pass, and outlet points for flat plate.

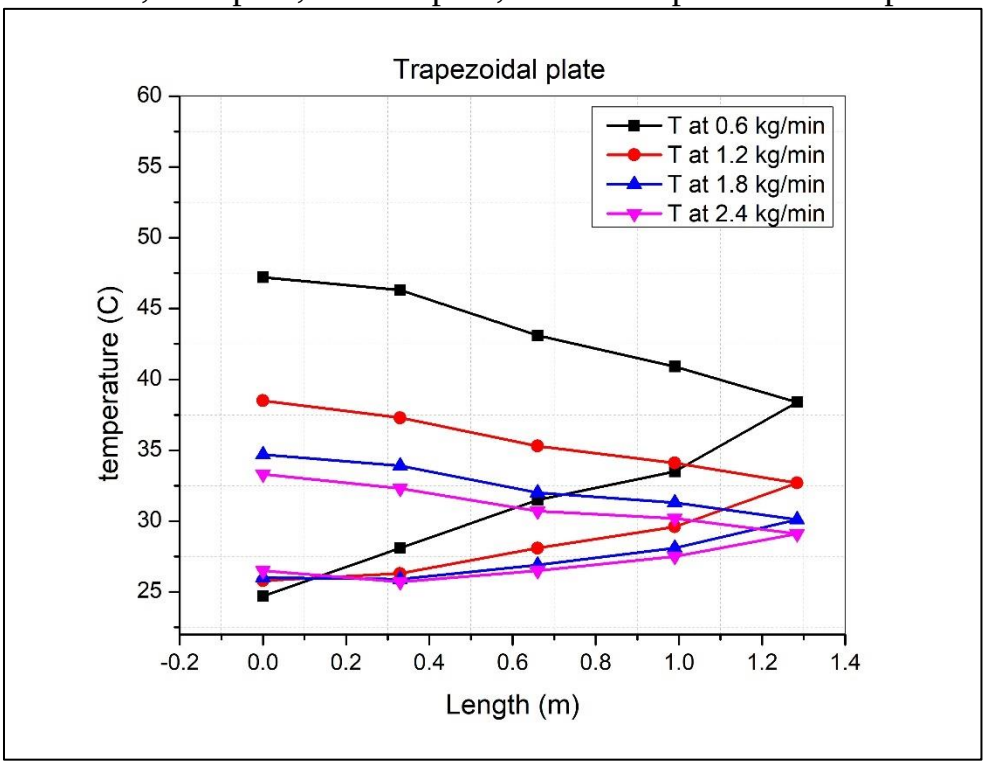

Figure 5. 17: The effect of MFR on the temperature of the airflow in the SAH at the inlet, first-pass, second-pass, and outlet points for trapezoidal plate.

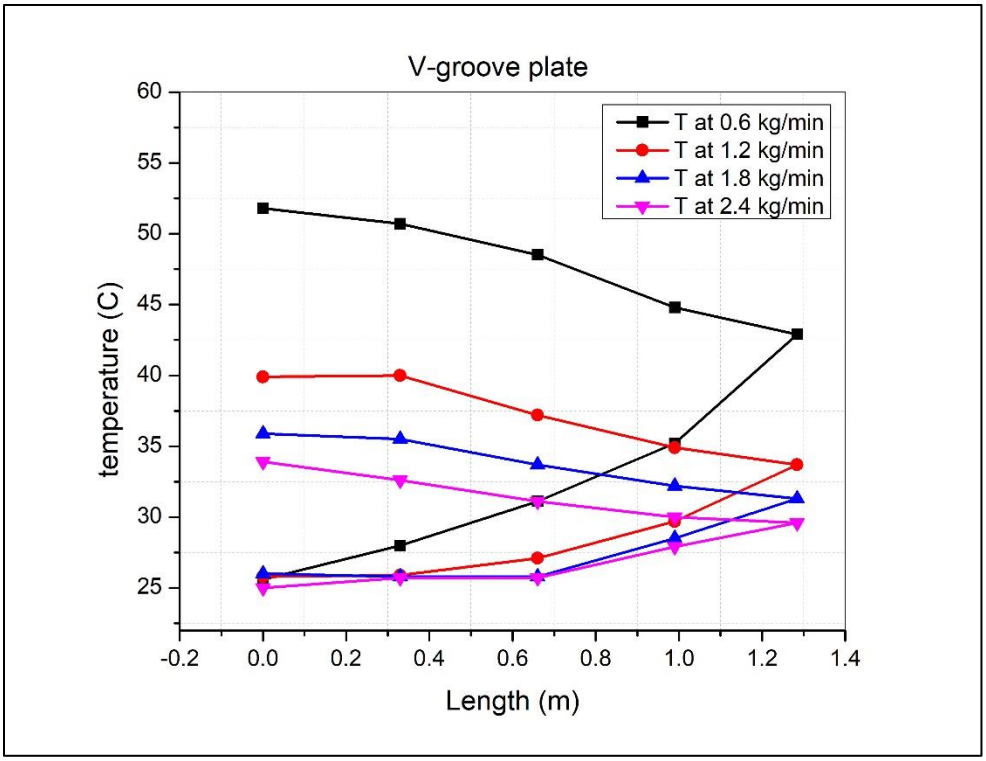

Figure 5. 18: The effect of MFR on the temperature of the airflow in the SAH at the inlet, first-pass, second-pass, and outlet points for V-groove plate.

5.2.4. Variation Temperature Rise of Air for Three Models of SAH:

Figure (5.19) shows the variation of air temperature rise versus air MFR for three models of solar collectors (flat, trapezoidal, and v-groove) under constant solar radiation (825 W/m^2). It has been observed that the temperature difference decreases with the increase in the air MFR in all models. Due to the high temperature of the air outlet, the airflow is reduced when the airflow speed increases.

Moreover, the increased air temperature in the collector with a V-groove plate was higher than the other plates because this plate provides more turbulence than other types in addition to its larger area. Also, the maximum values of air temperature rise obtained through the collector for the flat, trapezoidal and V-groove plate can be presented as approximately (16.6, 22.5, and 26.2) °C.

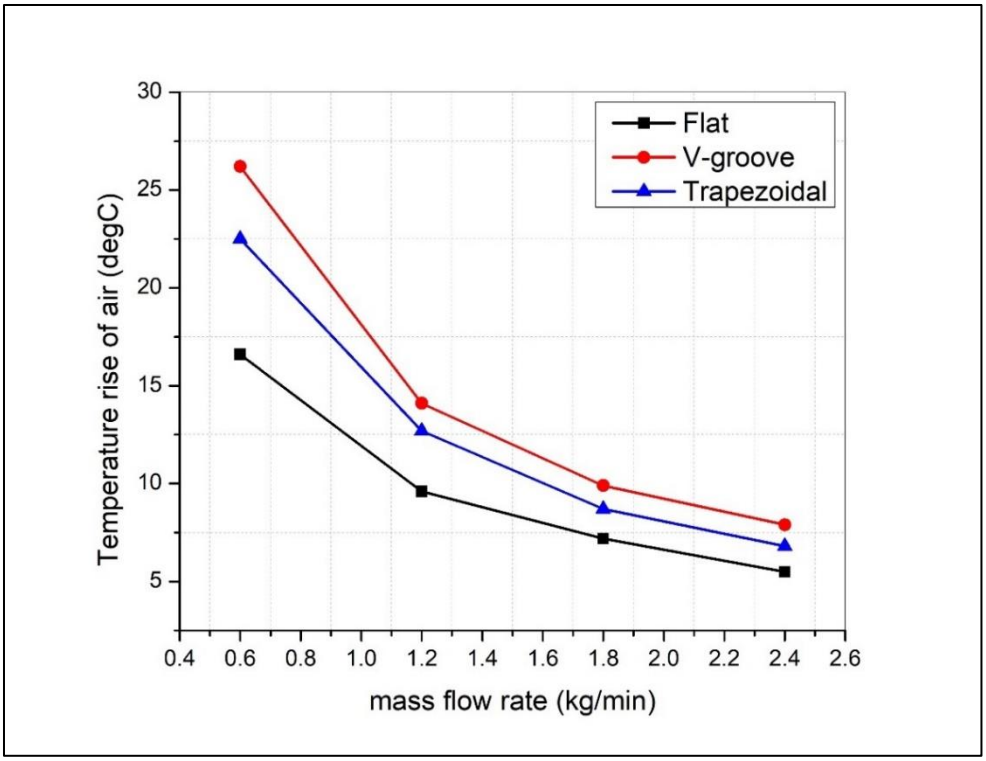

Figure 5. 19: Temperature rise of air ($\Delta T=T_{out} - T_{in}$) and air MFR of the DP-SAH for different absorber plate.

5.2.5. Useful Energy Rate and Thermal Efficiency:

Figures (5.20) and (5.21) show the effect of air MFR on the useful gain energy and thermal efficiency in three models of double-pass solar air heaters (flat, trapezoidal, and V-groove plate). The results expressed that with the increase in the airflow rate, the gain energy increased by changing the air MFR from 0.6 to 2.4 kg/min. Besides, the gain energy of the air for the solar air heater using a V-groove plate was higher than the other two collectors, as shown in figure (5.20) where the useful gain energy values obtained from the collectors with a flat, trapezoidal and V-groove plate reach to (167.252 – 222.05), (226.674 – 275.434) and (263.924 – 320.218) W, respectively. Thus, the flat plate has the lowest useful gain energy values, the trapezoidal plate has higher than the flat plate, and the V-groove plate has the highest useful gain energy value.

The thermal efficiency was studied in the double-pass solar air collector with three types of absorption plates (flat, trapezoidal, and V-groove) under constant solar intensity radiation of 825 W/m^2 and an air MFR ranging between 0.6 to 2.4 kg/min as shown in figure (5.21). It can be seen that the thermal efficiency increased when the air MFR increased in all models, which indicates that the thermal efficiency is highly dependent on the mas flow rate. It is also found that the thermal efficiency of the double-pass solar air heater of a flat plate absorber ranges between (27.69 – 55.64) %, and the thermal efficiency of a trapezoidal plate ranges between (45.7 – 72.91) %. Finally, the thermal efficiency of the V-groove plate ranges between (53.92 – 85.46) %. The figure also shows that the v-groove plate has a maximum thermal efficiency value of 85.46 %. Also, the trapezoidal plate has lower value than the V-groove plate, while the flat plate has the lowest thermal efficiency.

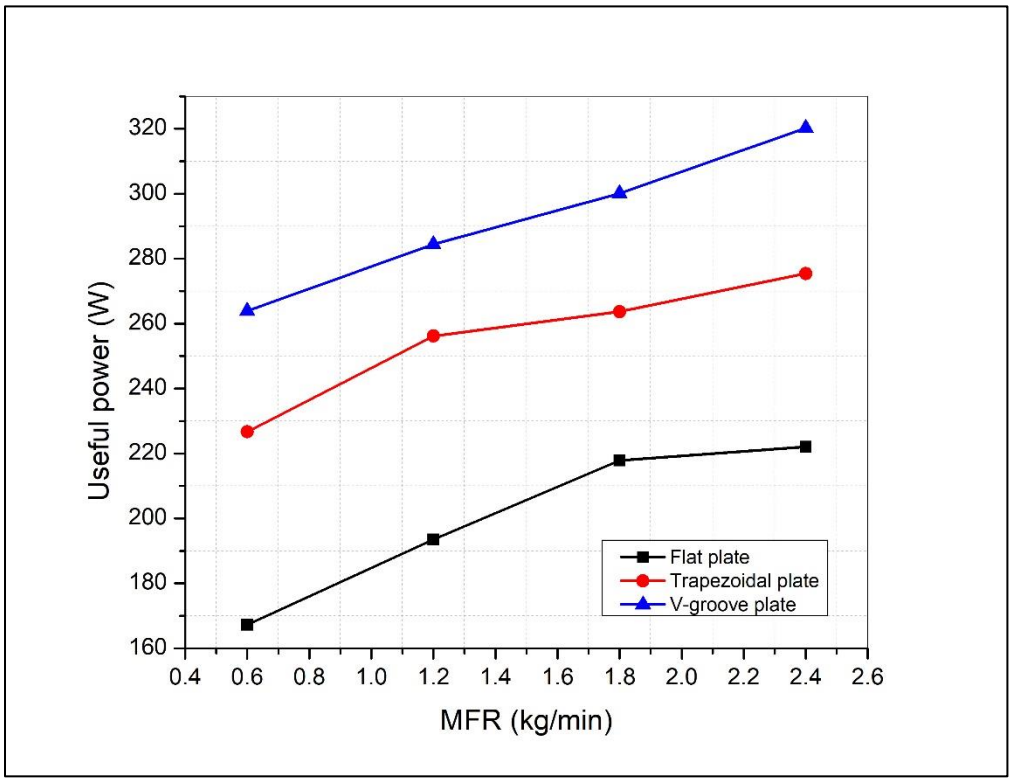

Figure 5. 20: Useful power of air against MFR for flat, trapezoidal, and V-groove plates.

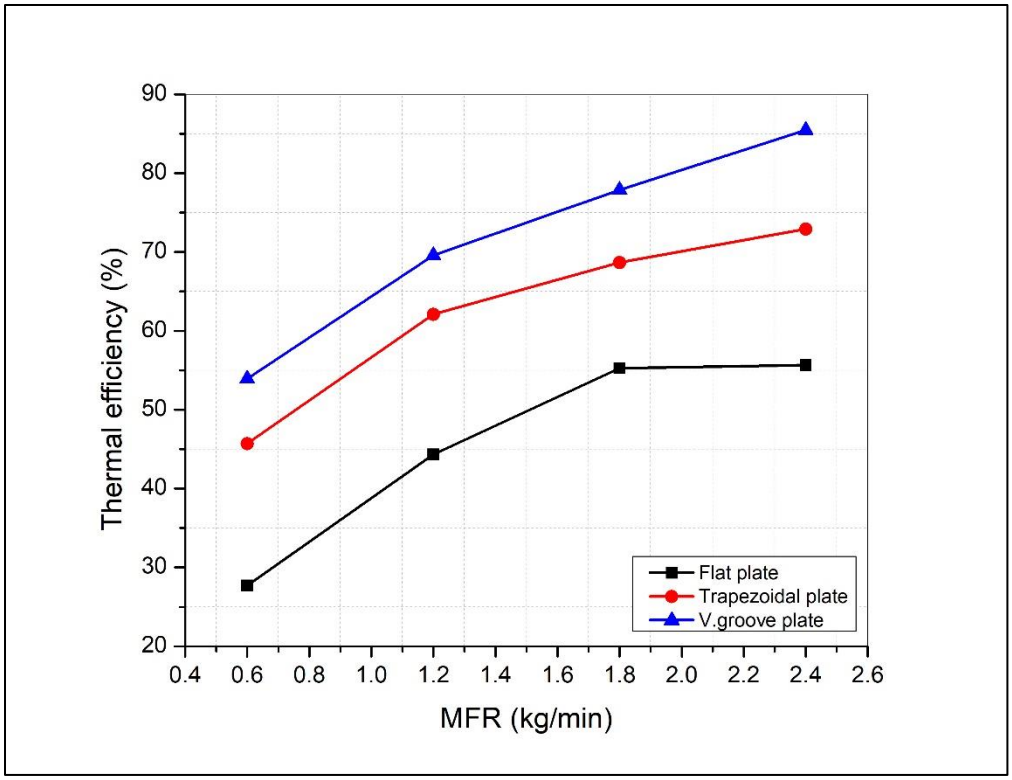

Figure 5. 21: Variation of thermal efficiency with MFR.

5.2.6. Exergy and Exergy Efficiency:

The exergy gain versus the air MFR in flat, trapezoidal, and V-groove absorber plate solar air heaters is shown in figure (5.22). it is also noted in the figure that the minimum and maximum exergy gain through the three types of solar air heaters was (17.449 – 33.76) W for the flat absorber plate, (31.439 – 53.83) W for trapezoidal absorber plate, and (34.62 – 73.68) W for V-groove absorber plate.

The maximum exergy gain is achieved at a lower MFR (0.6) kg/min. The highest exergy gain occurred in the V-groove type solar air heater, where the maximum value was up to (73.68) W, while it was less than that in the SAH with a trapezoidal plate, while the flat plate was the lowest of three types. The quality of converting available energy into useful energy is higher in the V-groove plate solar air heater, which results in higher exergy gain.

Figure (5.23) shows the variation of exergy efficiency with the MFR of solar air heaters with three types of absorbent plates (flat, trapezoidal, and V-groove) at a constant radiation intensity of 825 W/m^2. The exergy efficiency of flat, trapezoidal, and V-groove solar air heaters range is (5.18 – 10.04), (9.35 – 16.02), and (10.30 – 21.93) %, respectively.

It is noted that the V-groove plate has maximum exergy efficiency compared to the solar air heater with the trapezoidal plate, which in turn is higher than the flat plate in all ranges of MFR. The improvement is due to the increase in the heat transfer surface area and the occurrence of turbulence that leads to an increase in thermal energy gain. It is also seen from the figure that the V-groove absorber plate is more efficient at a low MFR. The percentage of exergy efficiency enhancement decreases with increasing MFR due to the higher MFR and outlet temperature.

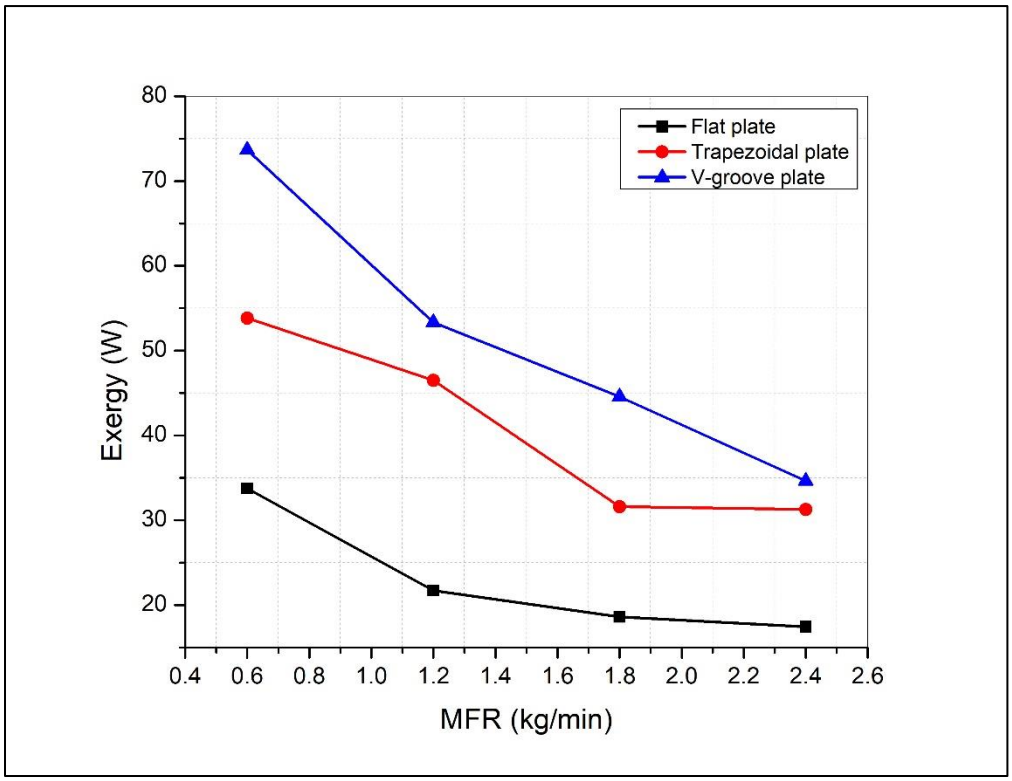

Figure 5. 22: Exergy of air against MFR for flat, trapezoidal, and V-groove plates.

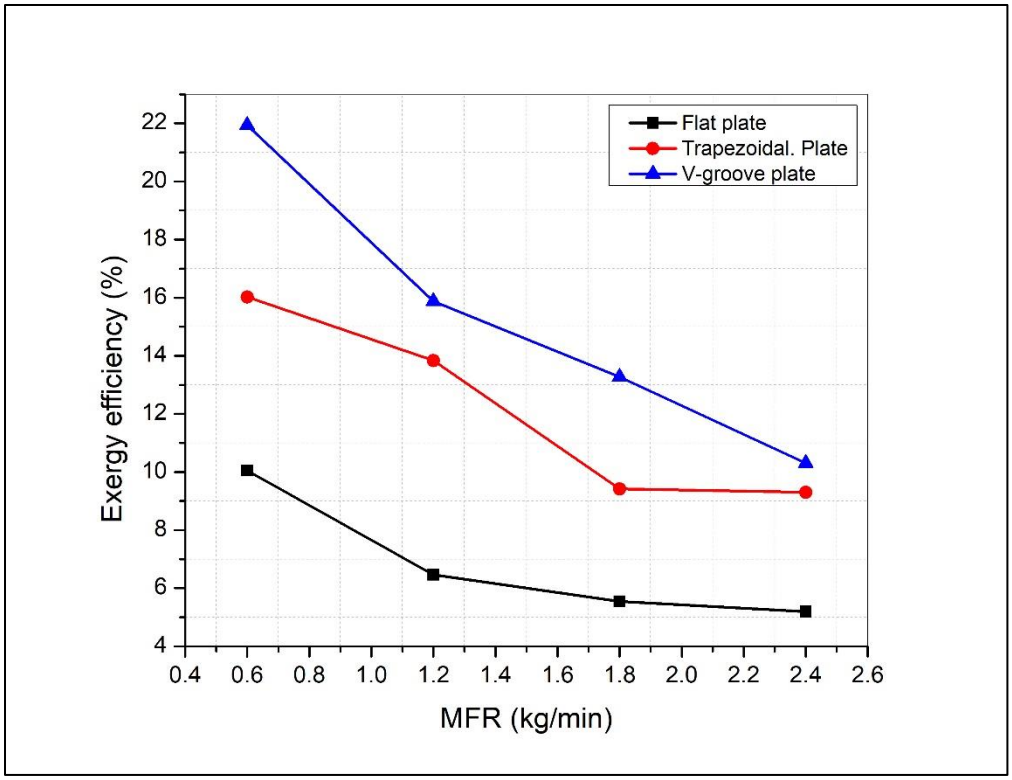

Figure 5. 23: Variation of exergy efficiency with MFR.

5.2.7. Pressure Drops:

The effect of airflow rate on the pressure drops at the inlet and outlet of the DP-SAH under solar radiation intensity of (825) W/m^2, which is found in the experimental tests, can be appeared in figure (5.24). Tests revealed that the pressure drop curves were increased by increasing the air MFR between the inlet and outlet.

The pressure drop in the V-groove plate solar air heater is higher than that of the flat and trapezoidal plate solar air heaters due to the increased friction while using the V-groove plate. The maximum experimental pressure drops with V-groove, trapezoidal and flat plate is (59), (45), and (15) Pa, respectively, at an air flow rate (2.4) kg/min.

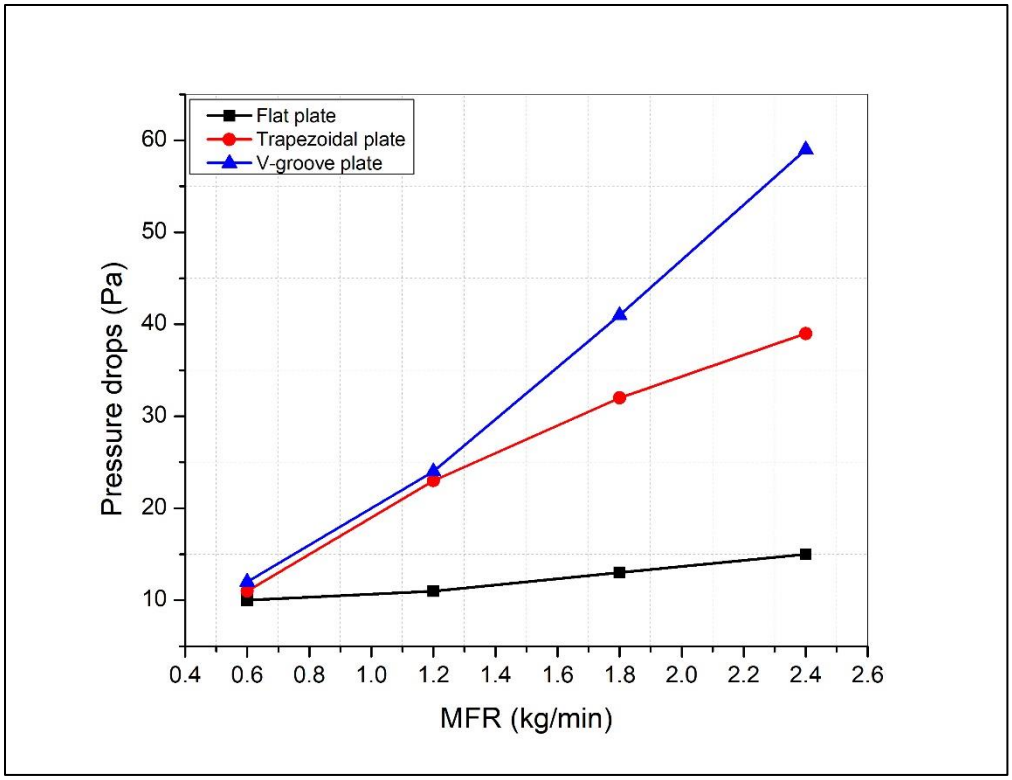

Figure 5. 24: Variation of pressure drops with MFR of air.

The results expressed that the representative maximum drop between the input and output of the collector is about (59) Pa in the V-groove plate collector with a MFR of (2.4) kg/min. The decreased pressure is due to the flow of recirculated air at the end of the collector into the second channel formed between a cover glass and absorption plate and friction. The pressure loss across the solar air collector is negligible where (59) Pa represents only (0.058) % of atmospheric pressure; hence the density change due to pressure change is very small.

5.3.Numerical Analysis Results:

This section presents the performance test results of solar air collectors based on variations in the absorber plate geometry. A two-dimensional numerical simulation of solar air heaters was carried out using three absorption plates (flat, trapezoidal,

and V-groove). The governing equations of the SAH system were determined and solved using the simulation software COMSOL Multiphysics v5.5 to determine the best absorption plate of the three types.

5.3.1. Temperature Distributions:

Figures (5.25) to (5.27) appear the variation of the air temperature distribution along the double-pass solar air collector at constant radiation intensity of 825 W/m^2 and at different MFR range (0.6 – 2.4) kg/min using three types of absorption plates (flat, trapezoidal and V-groove).

The numerical results showed that the air temperature increases along the collector's path in the first and second pass due to the energy exchange from the absorbent surface to the air flowing in the collector. Results showed that the outlet temperature of the air decreases in the collector with the increase in the airflow velocity due to the low heat exchange.

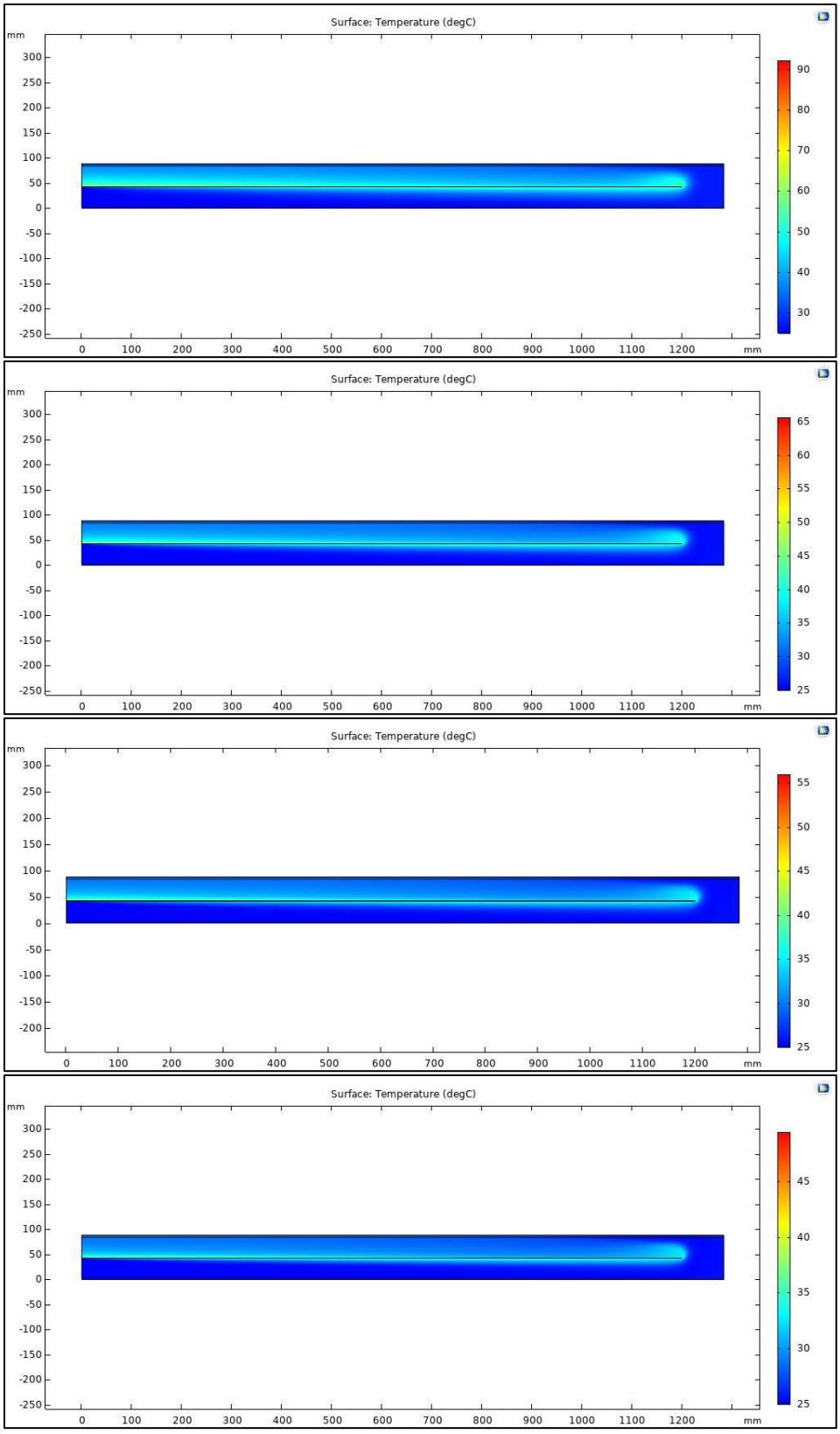

Figure 5. 25: Isothermal contors of Temperature for DP-SAH at for flat plate at MFR of (0.6), (1.2), (1.8), and (2.4) kg/min, respectively, at I=825 W/m^2.

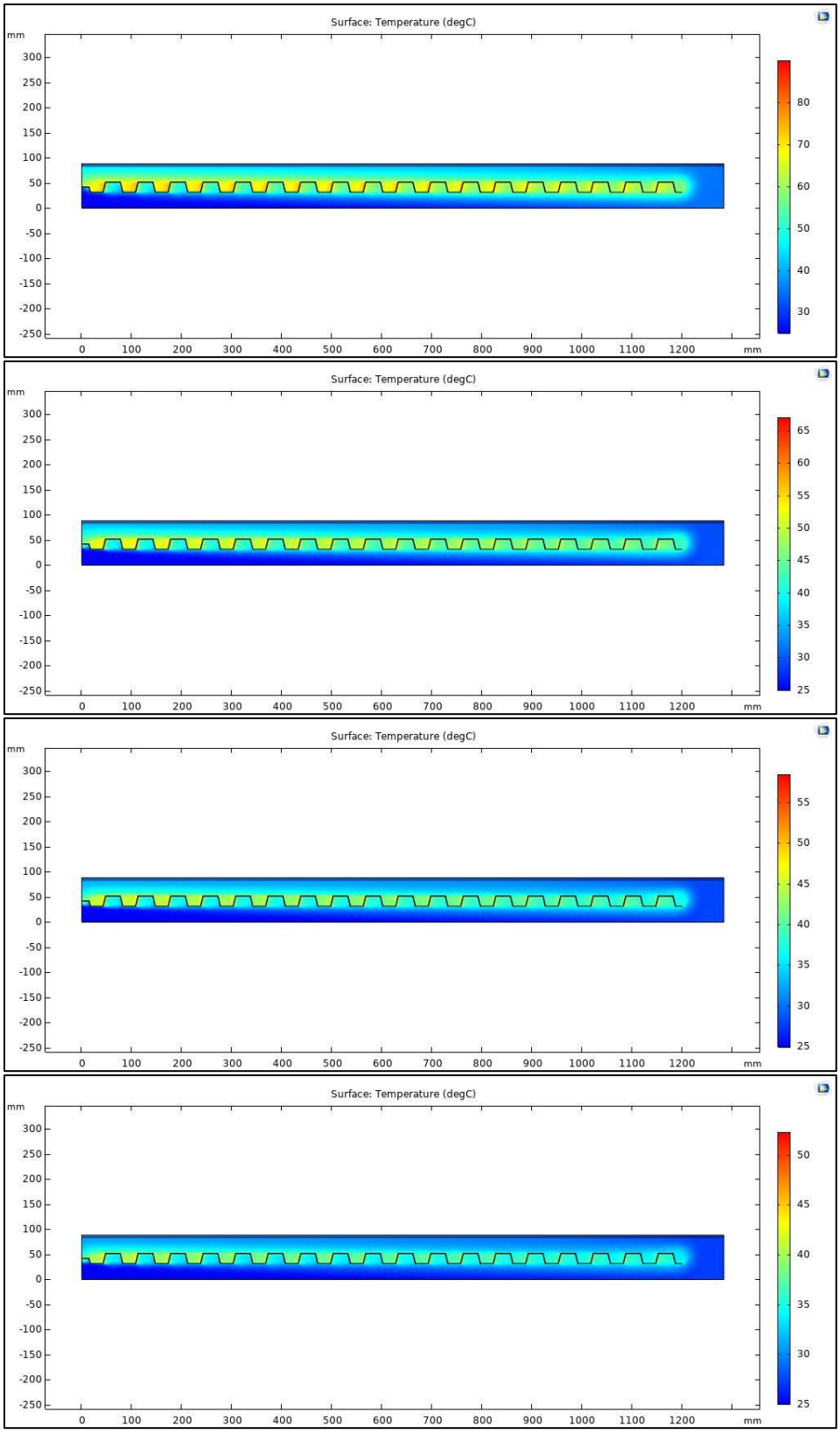

Figure 5. 26: Isothermal contors of Temperature for DP-SAH at for trapezoidal plate at MFR of (0.6), (1.2), (1.8), and (2.4) kg/min, respectively, at I=825 W/m^2.

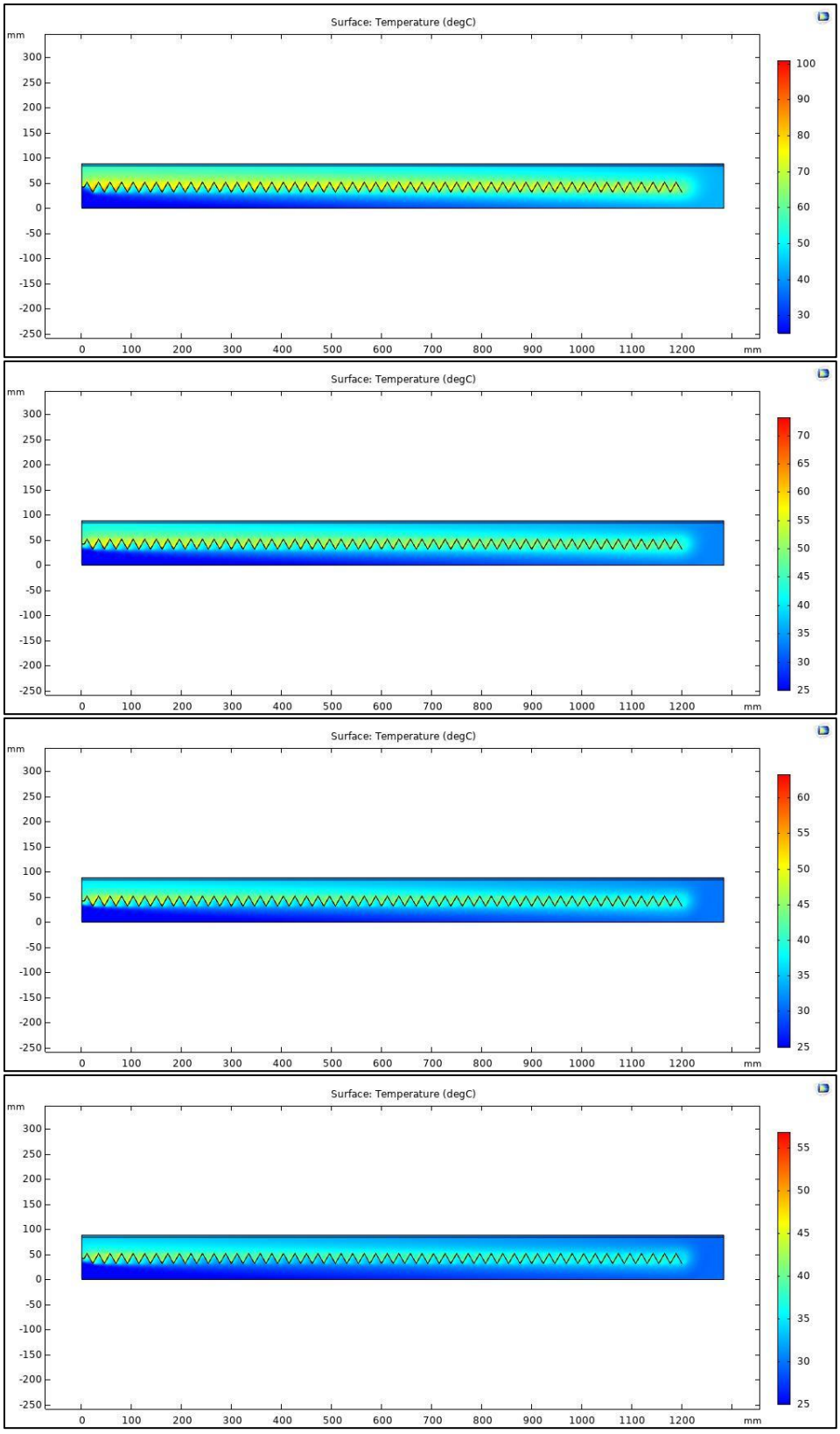

Figure 5. 27: Isothermal contors of Temperature for DP-SAH at for V-groove plate at MFR of (0.6), (1.2), (1.8), and (2.4) kg/min, respectively, at I=825 W/m^2.

Figures (5.25), (5.26), and (5.27) show the temperature distribution of the three plates. These figures show that the temperature decreases with the increase in the mass flow rate of the air for all plates, and the highest temperatures were for the V-groove plate, followed by the trapezoidal plate, and the flat plate has the lowest temperatures. The temperature distribution of the solar air heater along the air path will be illustrated in the following paragraphs.

5.3.2. Velocity Distribution:

Figures (5.28) and (5.29) show the change in the flow direction at the end of the first pass creates eddies that increase the exchange of energy at the absorption surface in the second pass compared to the airflow of a conventional heater. Also, changing the geometry of the absorbent plate increases the air turbulence in both passages, which causes an increase in the exchange of energy between the absorbent surface and the flowing air.

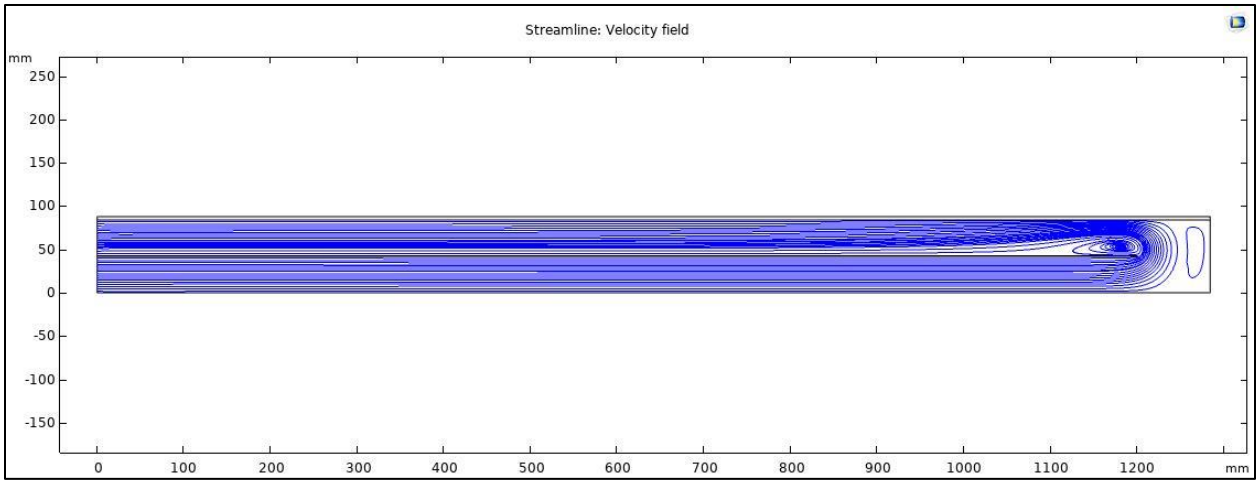

(a) Flat plate

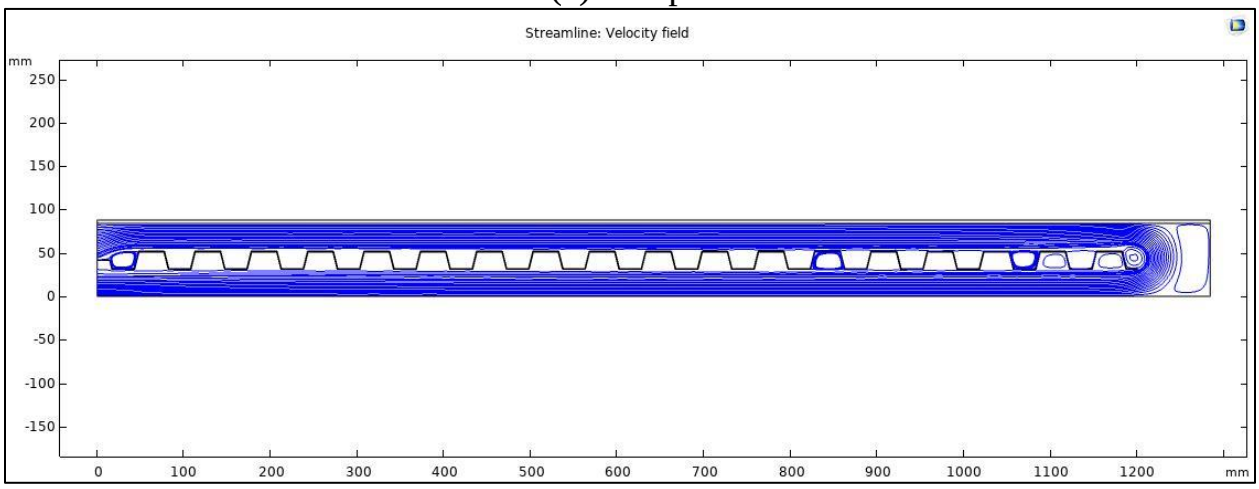

(b) Trapezoidal plate

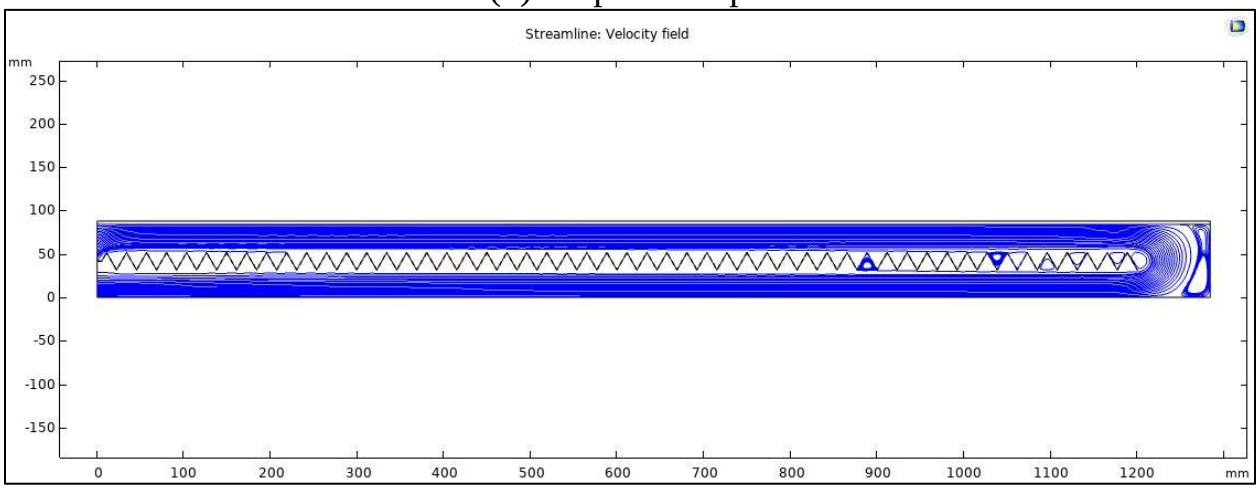

(c) V-groove plate

Figure 5. 28: Velocity streamline for DP-SAH with the same MFR of 0.6 kg/min and different absorber plate (a) Flat plate (b) Trapezoidal plate (c) V-groove plate.

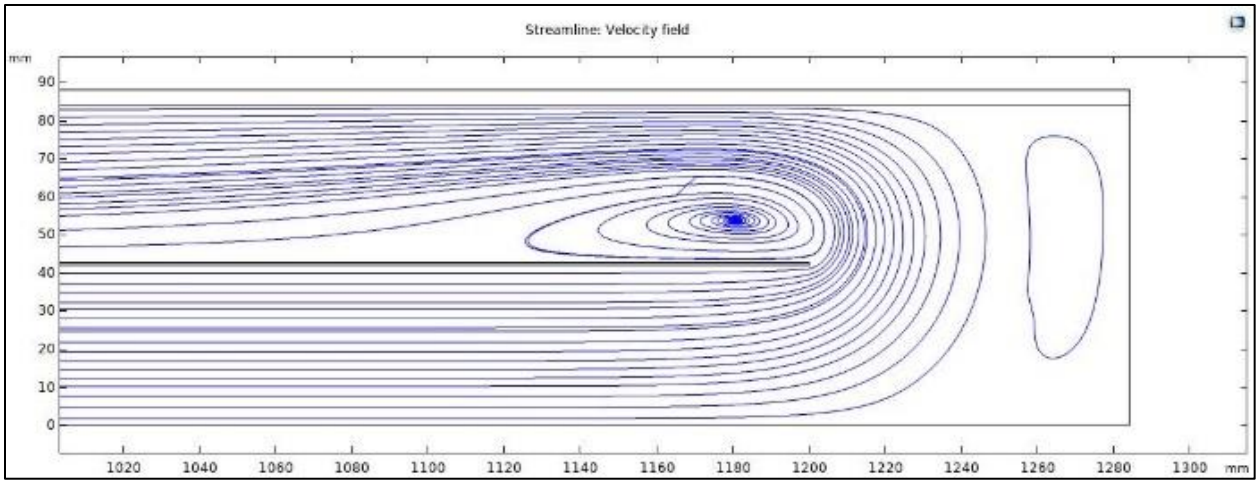

(a) Flat plate

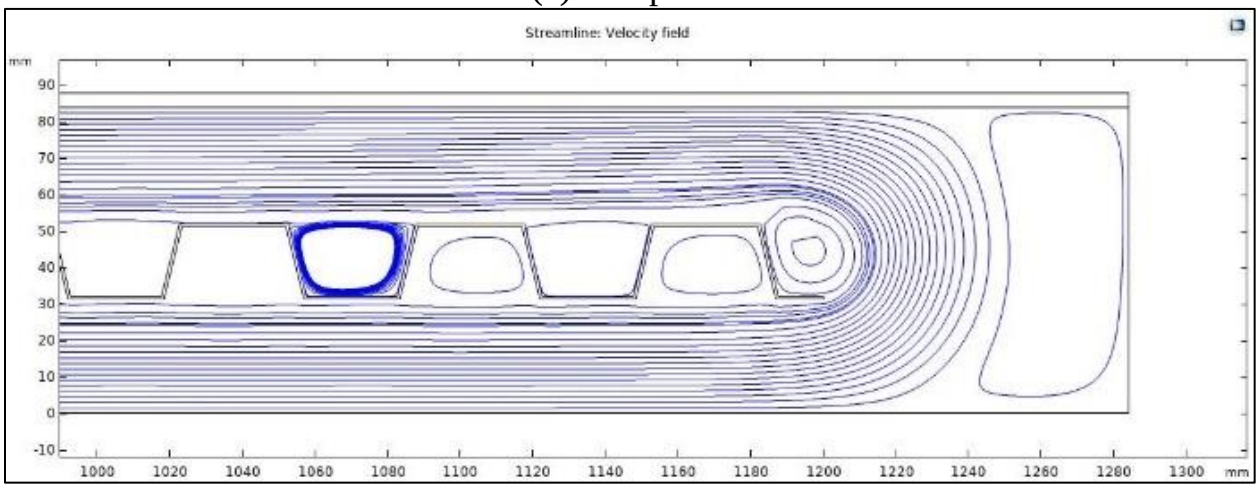

(b) Trapezoidal plate

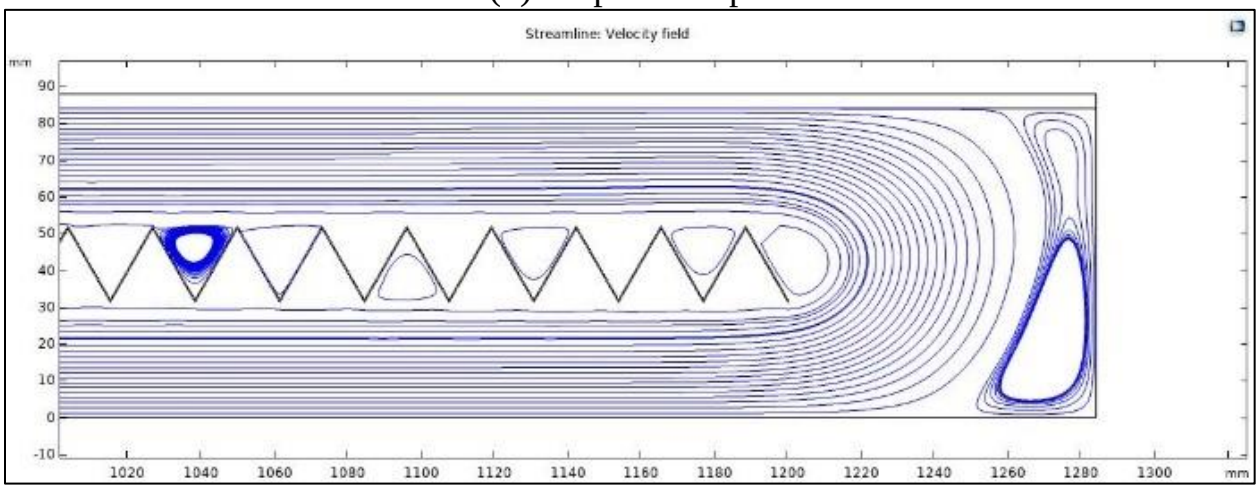

(c) V-groove plate

Figure 5. 29: Velocity streamline cross-section of DP-SAH with the same MFR of 0.6 kg/min and different absorber plate (a) Flat plate (b) Trapezoidal plate (c) V-groove plate.

5.3.3. The Effect of Air MFR on Collector Temperature for Absorbent Plates:

Based on the results obtained from the numerical analysis using the COMSOL Multiphysics v5.5 program, the mean temperature in the double-pass solar air collector was represented by a constant solar radiation intensity of 825 W/m^2 with variable values of the MFR ranging (0.6 – 2.4) kg/min using three types of absorbent plates (flat, trapezoidal and V-groove) in figures (5.30), (5.31), and (5.32).

These figures show the mean temperatures of the absorption plate and the air in the first and second passages. It can be observed from numerical tests a decrease in the temperature curves when the air MFR is increased.

Also, the results show that the temperature of the absorbent plate is the highest temperature value in the double-pass solar air collector of all three models. The temperature of the flat, trapezoidal and V-groove plate ranges between (40.19 – 58.58) °C, (41.27 – 61.34) °C, and (41.94 – 67.79) °C, respectively, at an MFR ranging between (0.6 – 2.4) kg/min. Thus, the highest temperature value will be the V-groove type plate compared to the other two types, followed by the trapezoidal plate and flat plate.

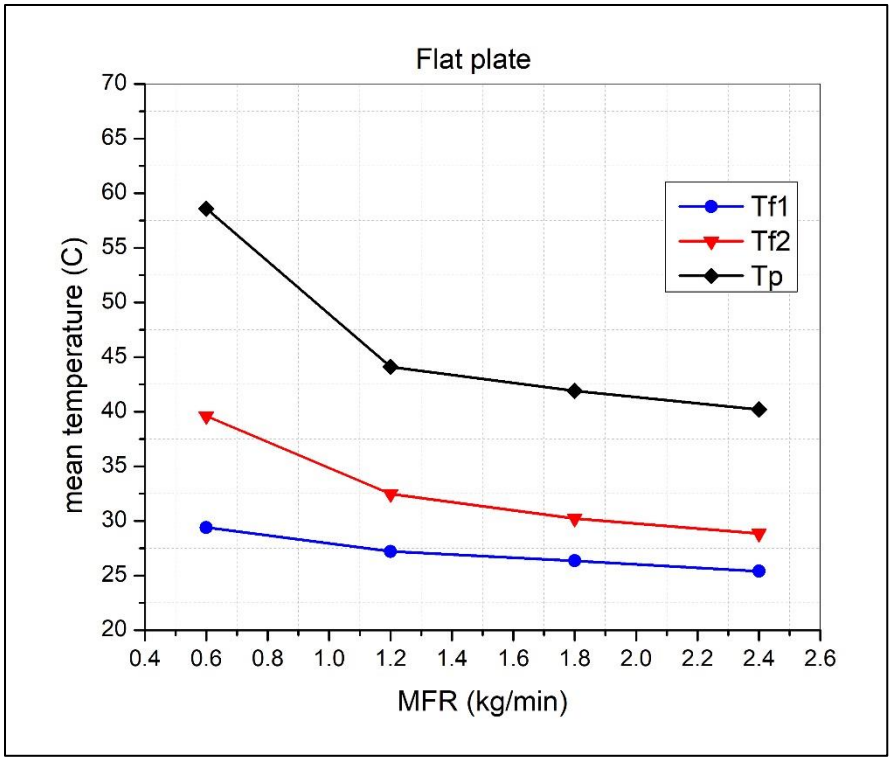

Figure 5. 30: The numerical average temperature in the Flat plate DP-SAH and MFR of air.

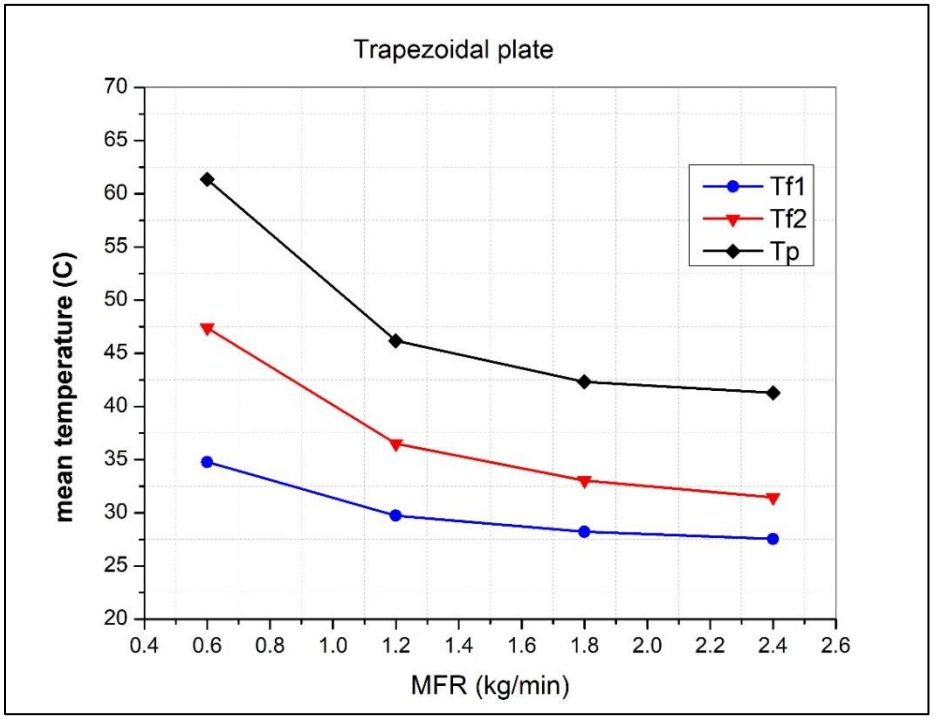

Figure 5. 31: The numerical average temperature in the Trapezoidal plate DP-SAH and MFR of air.

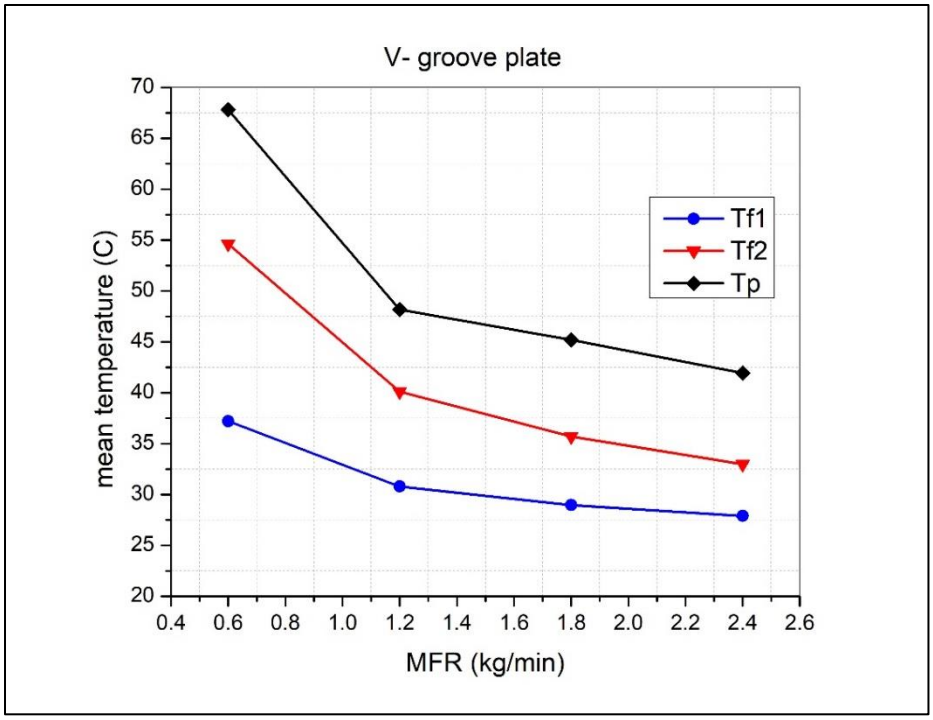

Figure 5. 32: The numerical average temperature in the V-groove plate DP-SAH and MFR of air.

5.3.4. Temperature Variation of The Airflow Along the First and Second Passage in The Double-Pass Solar Air Collector:

Figures (5.33), (5.34), and (5.35) represent the results obtained from the numerical analysis using the COMSOL Multiphysics v5.5 software, where the change in temperature of the airflow along the path of a double-pass solar air collector with a flat, trapezoidal and V-groove plate at a variable MFR ranging between (0.6 – 2.4) kg/min.

The figure shows the path of air from the entrance of the collector to the first passage limited between the absorption plate and the background, and then it is recycled to the second passage located between the glass and the absorption plate. The figures show the increase in air temperature from the input to the output of the collector. The results show that the air temperature at the outlet of the collector with a V-groove absorption plate is higher than that of the collector with a trapezoidal

absorption plate. And the air temperature at the outlet of the collector with a trapezoidal absorption plate is also higher than a flat absorption plate.

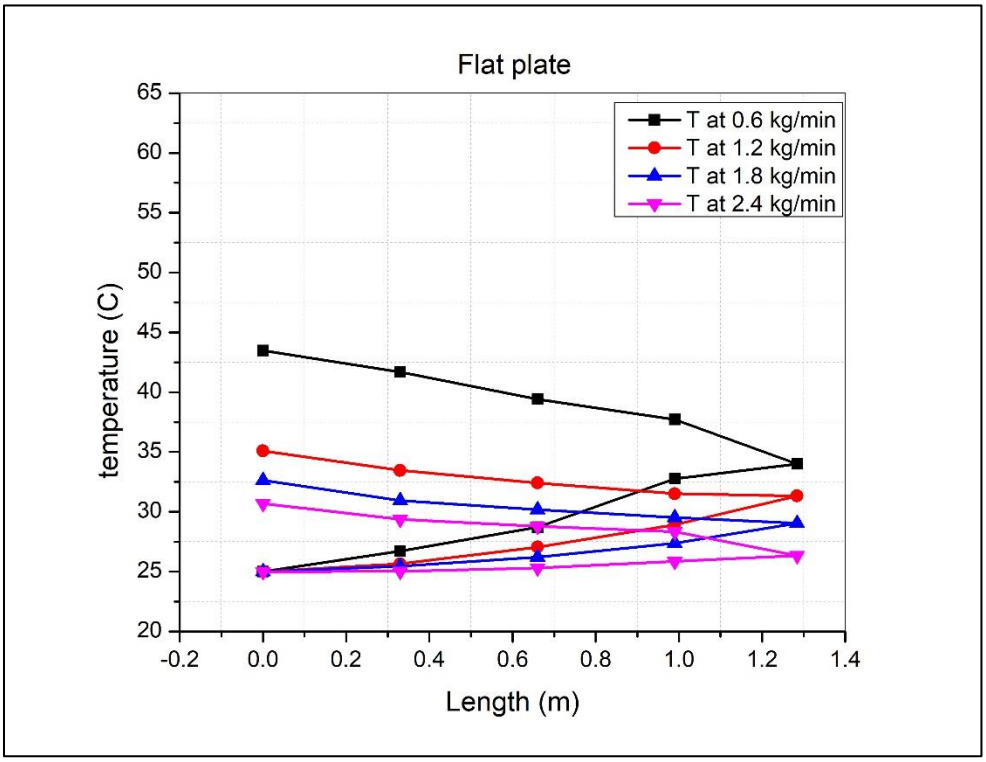

Figure 5. 33: The effect of MFR on the temperature of the airflow in the SAH at the inlet, first-pass, second-pass, and outlet points for flat plate in numerical simulation at I=825 W/m^2.

Results indicated that an increase in the air MFR causes a decrease in the temperature of the outside air in the collector at the same intensity as solar radiation. At a MFR of (0.6, 1.2, 1.8, and 2.4) kg/min, the outlet air temperature with a flat absorption plate is (43.483, 35.091, 32.644, and 30.69), respectively. At the same time, the outside air temperature when there is a trapezoidal absorption plate reaches (50.597, 38.548, 34.719, and 33.425), respectively. Finally, the outside air temperature when an absorption plate with a V-groove reaches (58.1, 42.5, 37.476, and 34.3), respectively.

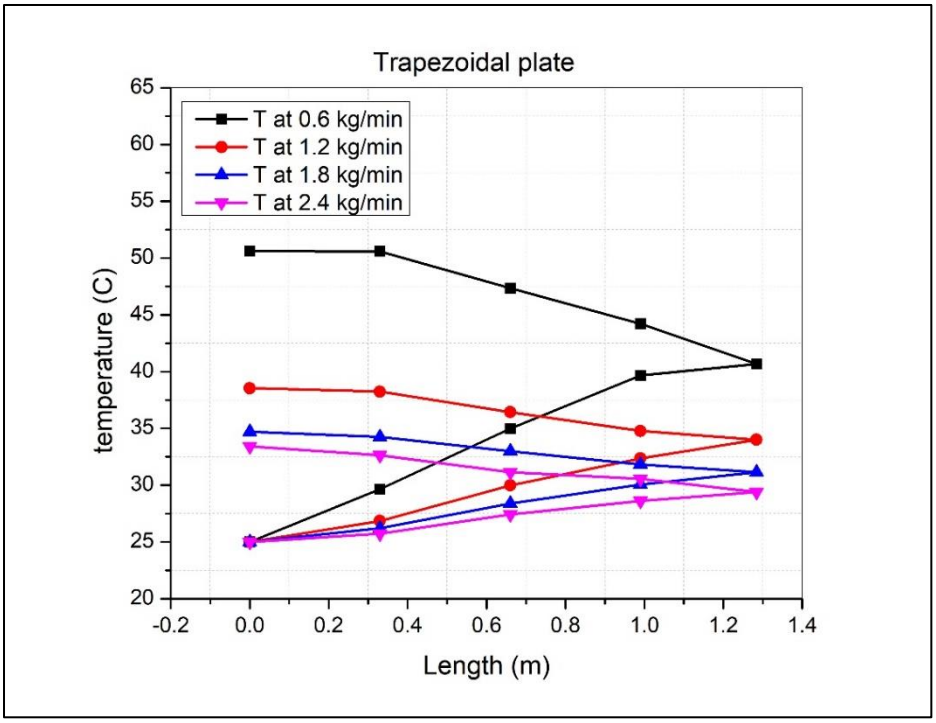

Figure 5. 34: The effect of MFR on the temperature of the airflow in the SAH at the inlet, first-pass, second-pass, and outlet points for trapezoidal plate in numerical simulation at I=825 W/m^2.

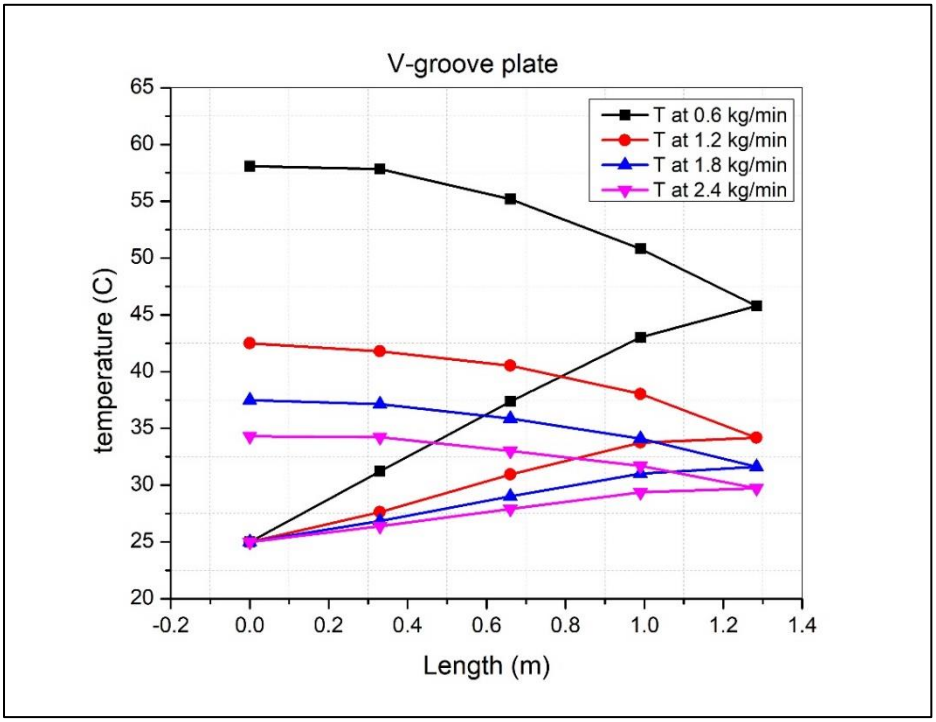

Figure 5. 35: The effect of MFR on the temperature of the airflow in the SAH at the inlet, first-pass, second-pass, and outlet points for V-groove plate in numerical simulation at I=825 W/m^2.

5.3.5. Thermal Efficiency:

Figure (5.36) shows the thermal energy efficiency of the numerical analysis of solar air heaters when using three types of absorption plates (flat, trapezoidal and V-groove) with a MFR ranging between (0.6 – 2.4) kg/min. The figure shows that the thermal efficiency of all solar air heaters increases with the MFR because the heat removal capacity depends on the MFR.

Based on the results shown in the figure, the thermal efficiency of the solar air collector with a flat absorption plate range (28.8 – 56.27) %. At the same time, it reaches (48.94 – 87.8) % when using a trapezoidal absorption plate in the solar air collector, which is higher than the conventional solar air collector, which is higher than the conventional solar air heater. However, the maximum thermal efficiency that can be reached in solar air collectors when using an absorption plate with a V-groove ranges between (67 – 99) %. Thus, the thermal efficiency is higher in the third type than in the first and second types.

The reason for the high efficiency in the numerical study is due to the assumptions that were imposed to facilitate the application and solution of the program, in addition to the fact that the aspects are completely isolated in the program, unlike the practical side, in which heat exchange can occur through insulators.

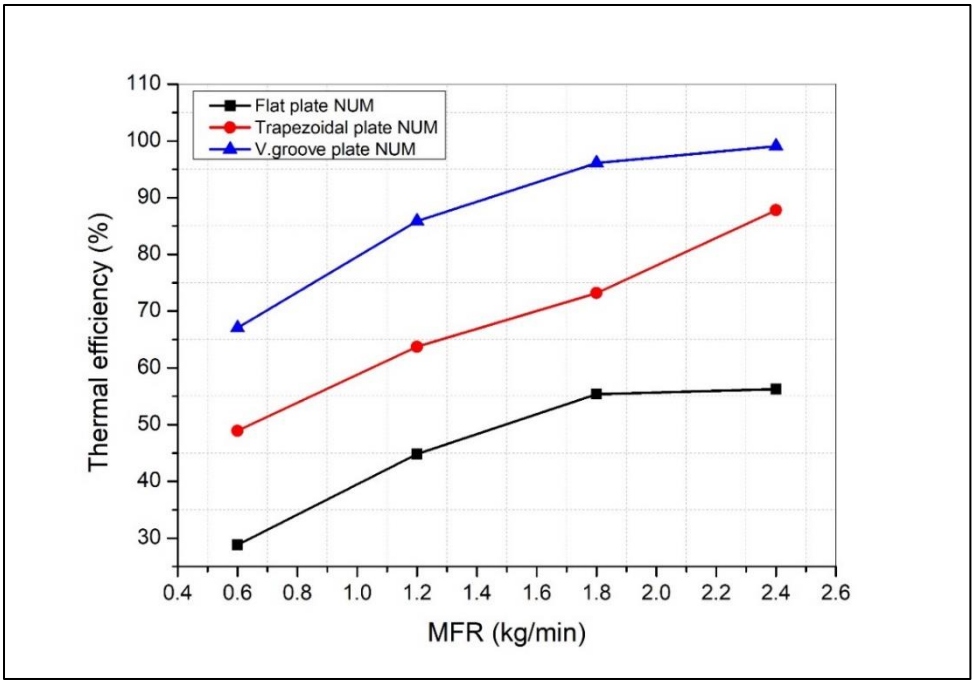

Figure 5. 36: Variation of thermal efficiency with MFR in numerical simulation.

1.1. Validation of the Numerical Study:

In each numerical analysis operation, verification is a very substantial step. In this study, to validate the numerical model, a comparison was conducted between the numerical analysis and a previous study that used the results produced by Abdulaziz Doukhi [57] to legitimize the CFD analysis. This demands the analysis of the gained results of the CFD validation for average outlet air temperatures (Tout) for DP-SAH, where the error ratio was calculated between the results of the current work and the results of Abdulaziz Doukhi, and it was found to be less than 2%. The average outlet air temperature for the DP-SAH is illustrated in Figure (5.37).

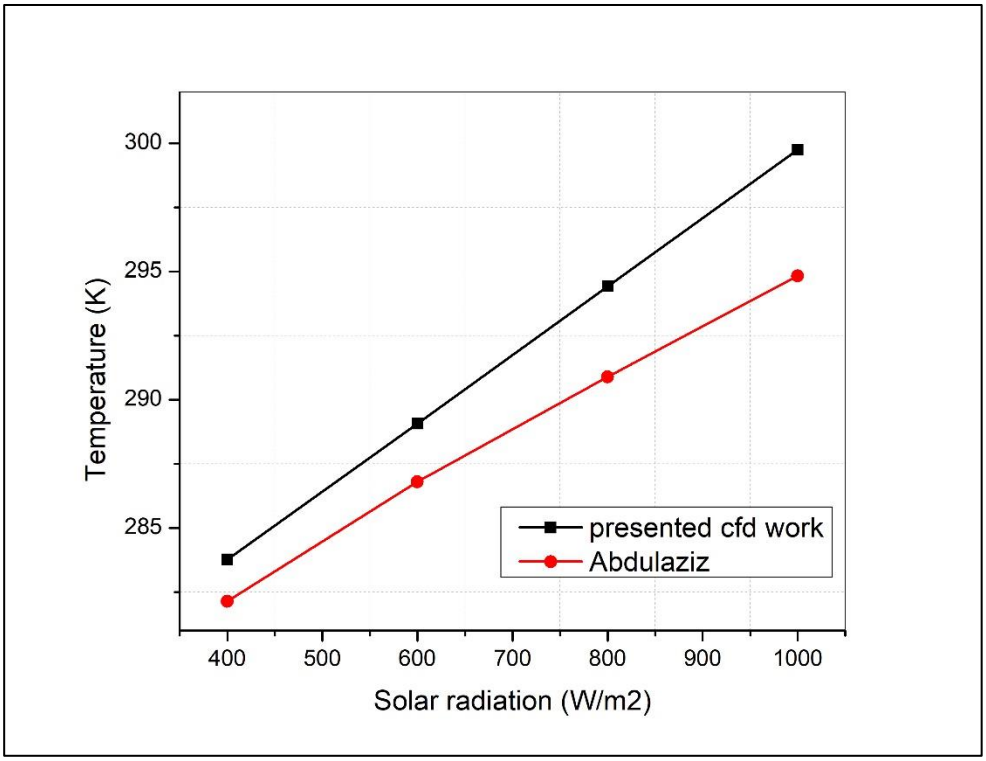

Figure 5. 37: outlet air temperature according to different solar radiation for the CFD analysis results compared with [57].

1.2. Comparison of Experimental and Numerical Results:

In this part of the discussion of the results, the experimental results are compared with the numerical analysis, where the same conditions of the experimental side were applied to the computational model to predict the experimental data accurately. The error ratio between the experimental results and numerical analysis is also calculated.

1.2.1. Air Temperature Along the First and Second Passage for DP-SAH:

Figures from (5.38) to (5.43) show a comparison of the difference between the air temperatures from the inlet of the collector to the outlet of three types of absorbing

plates for solar air collectors (flat, trapezoidal, and V-groove). At the constant MFR for all models at (0.6 and 1.2) kg/min only and constant solar radiation, its value 825 W/m^2.

The comparison results indicated that the numerical analysis temperature values are higher than the experimental temperature values. At the mass rate 0.6 and 1.2 kg/min, figures (5.38) and (5.41) compare the numerical and experimental analysis of a SAH with a flat absorption plate, respectively. The figures show a temperature difference at the outlets of 2.283 and 0.991 °C, respectively.

At the same time, figures (5.39) and (5.42) compare the numerical and experimental analysis of a solar air heater with a trapezoidal absorption plate, respectively, where the figures show the temperature difference at the outlet that reaches 3.397 and 0.048 °C, respectively.

Based on figures (5.40) and (5.43), the temperature difference at the outlet reaches (6.3) and (2.6), respectively, when a comparison is made between the numerical and experimental analysis of the solar air heater with a V-groove absorption plate.

The average maximum error in outlet temperature between experimental and numerical findings was ± 4.43 %. It is apparent from the figures that there is an agreement between the experimental readings, and the numerical analysis is acceptable.

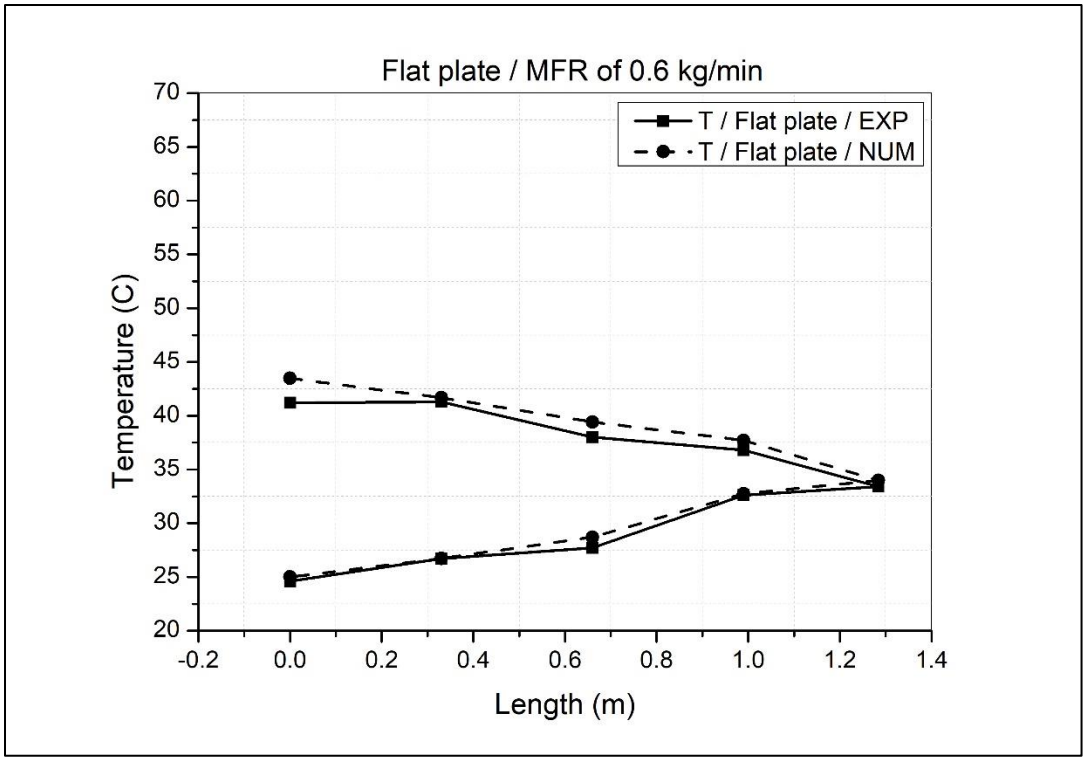

Figure 5. 38: Compared experimental and numerical results of air temperature along the first and second pass in the flat plate DP-SAH at an MFR of 0.6 kg/min.

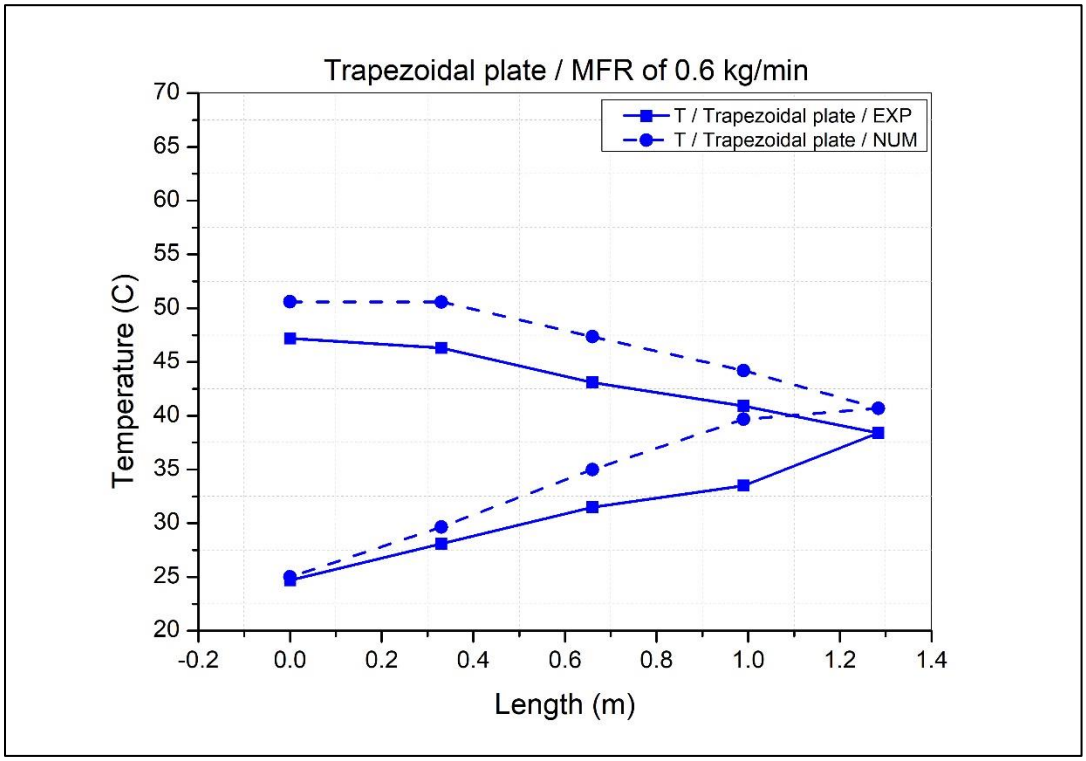

Figure 5. 39: Compared experimental and numerical of air temperature along the first and second pass in the trapezoidal plate DP-SAH at an MFR of 0.6 kg/min.

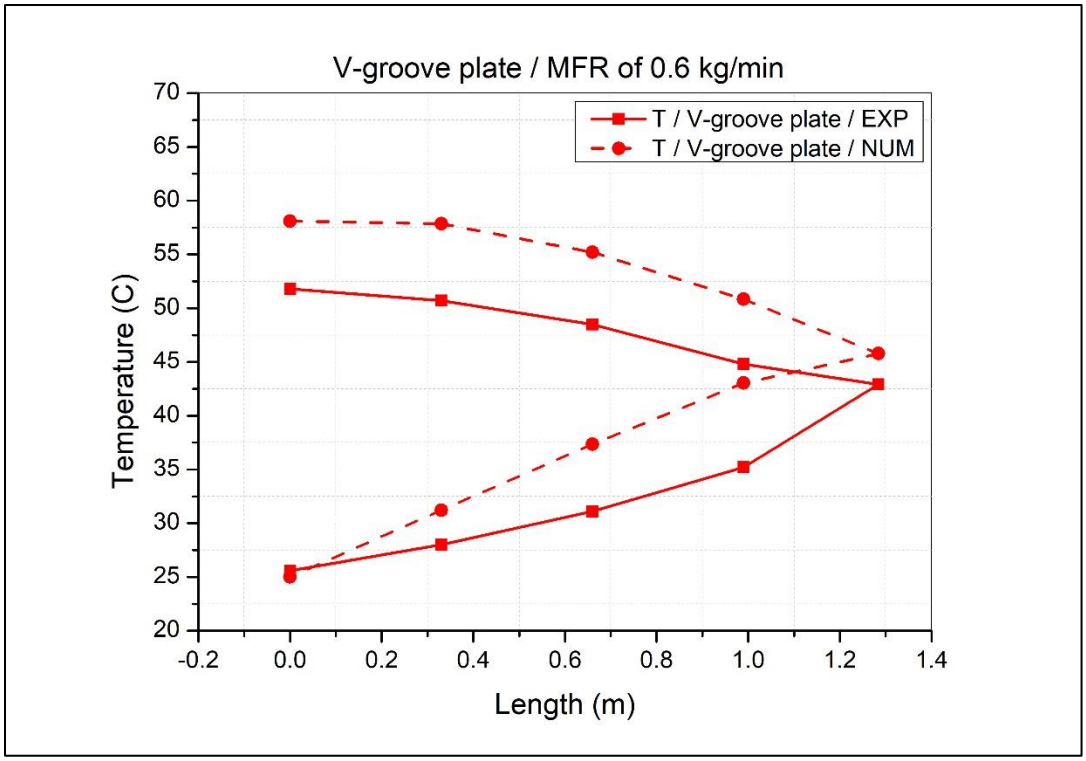

Figure 5. 40: Compared experimental and numerical results of air temperature along the first and second pass in the V-groove plate DP-SAH at an MFR of 0.6 kg/min.

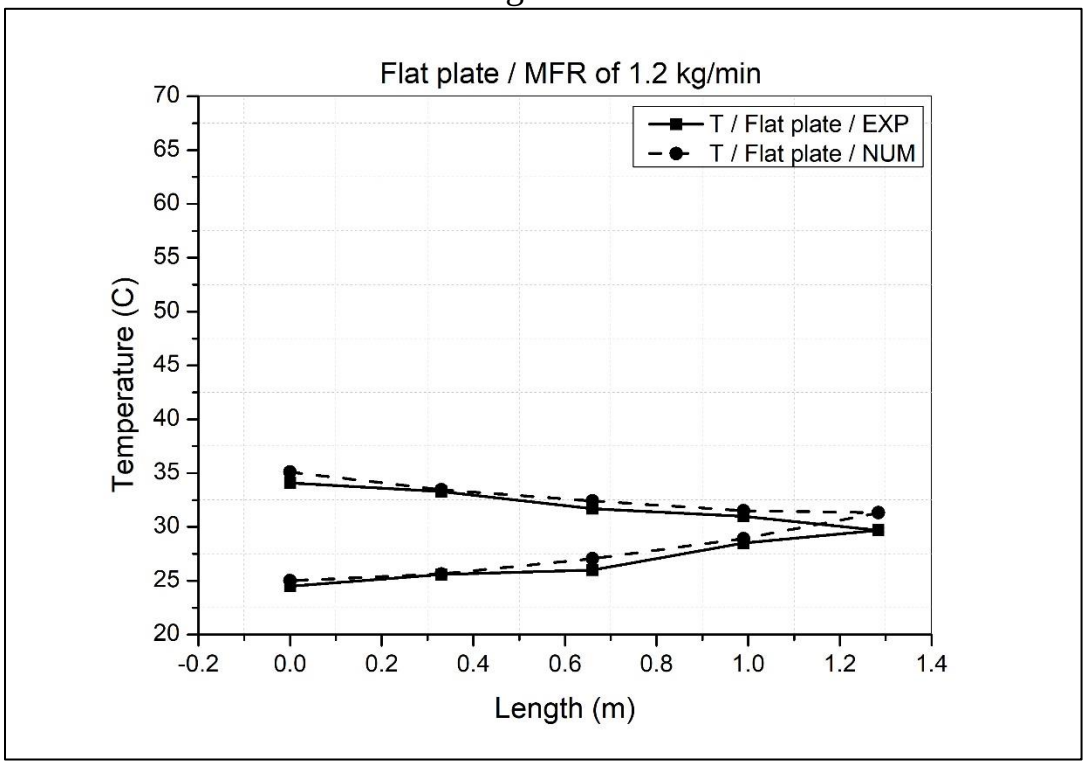

Figure 5. 41: Compared experimental and numerical results of air temperature along the first and second pass in the flat plate DP-SAH at an MFR of 1.2 kg/min.

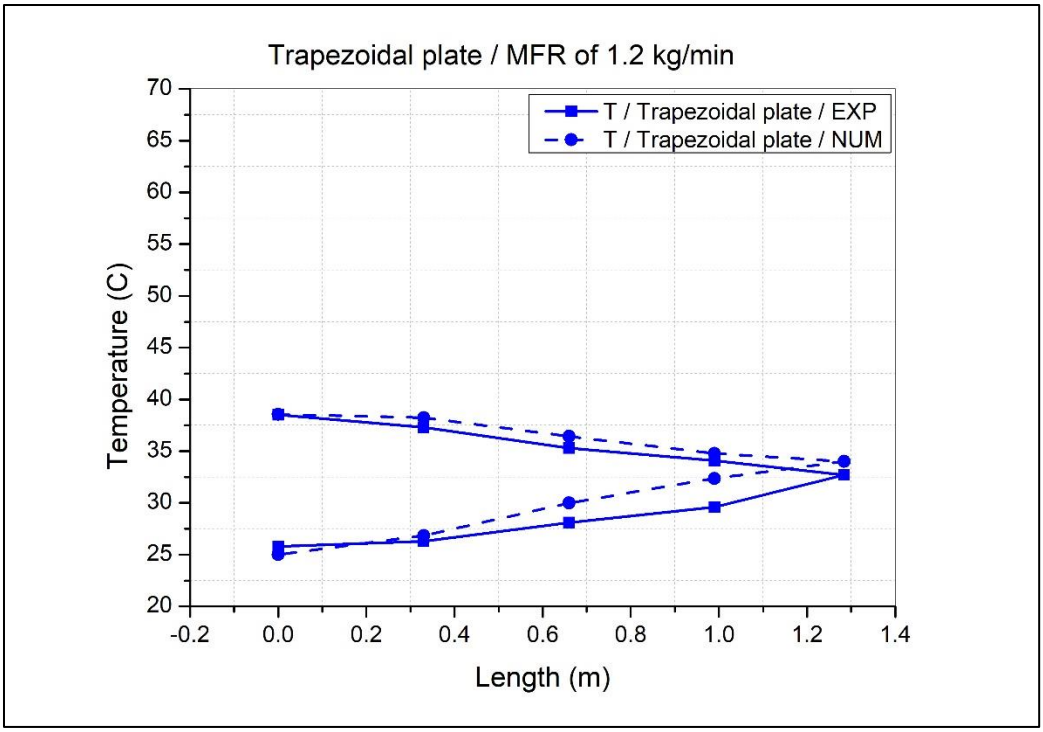

Figure 5. 42: Compared experimental and numerical results of air temperature along the first and second pass in the trapezoidal plate DP-SAH at an MFR of 1.2 kg/min.

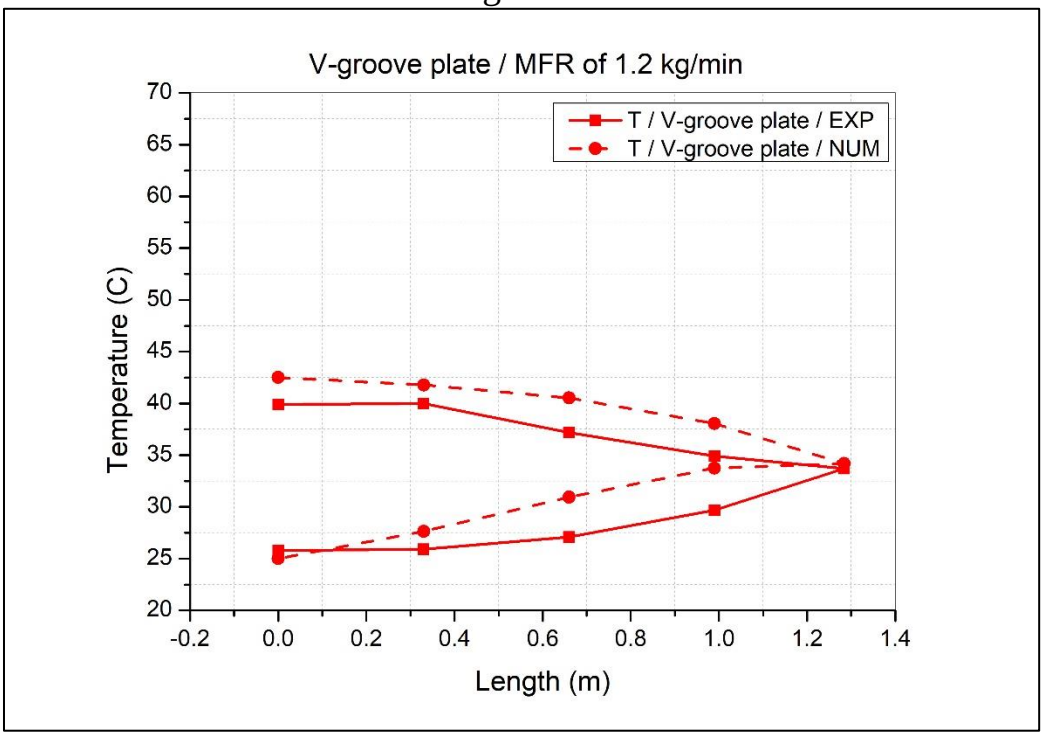

Figure 5. 43: Compared experimental and numerical results of air temperature along the first and second pass in the V-groove plate DP-SAH at an MFR of 1.2 kg/min.

1.2.2. Thermal Efficiency:

Figures (5.44), (5.45), and (5.46) show the comparison between the numerical and experimental analysis of the thermal efficiency of SAH when using three models of absorbent plates (flat, trapezoidal and V-groove).

The results shows that the error values for the thermal efficiency were (3.83, 1.13, 0.13, and 1.1) % for the flat absorption plate, (6.61, 2.53, 6.17, and 16.95) % for the trapezoidal absorption plate, and (19.5, 18.96, 18.8, and 13.74) % for the V-groove absorption plate at the MFR (0.6, 1.2, 1.8, and 2.4) kg/min, respectively.

The accuracy of the measuring devices employed in the studies and some assumptions are to charge for the errors in the results. It is noted that there is good correspondence between experimental measurements and the numerical results.

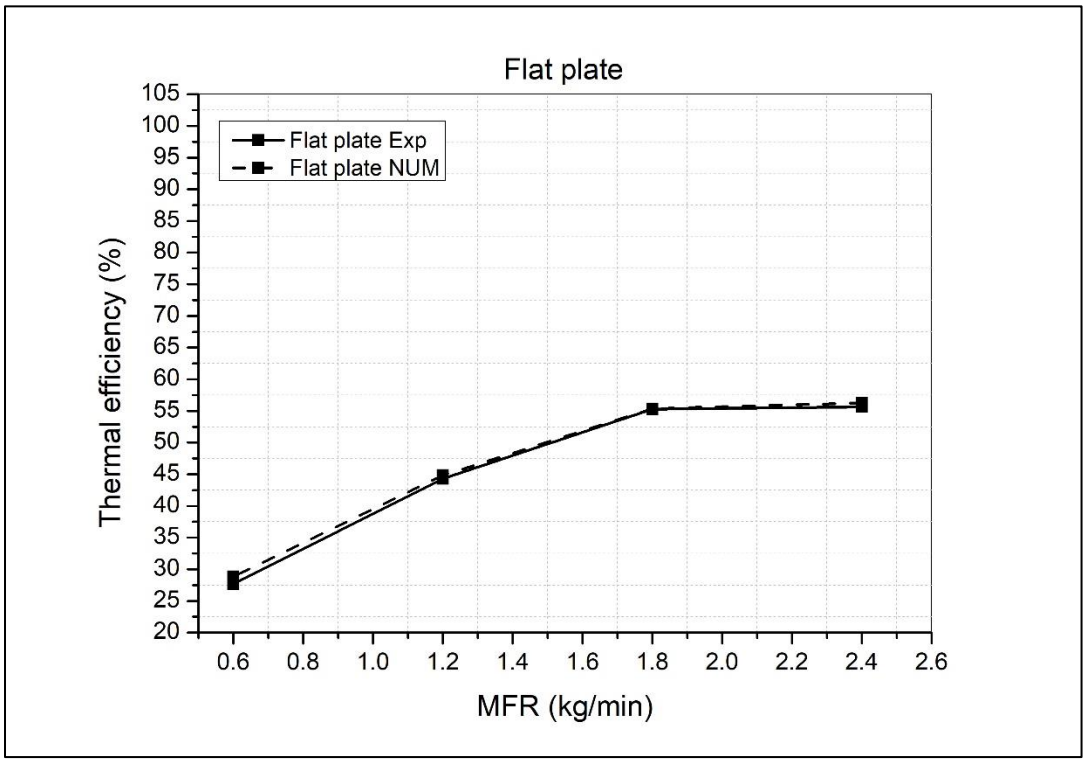

Figure 5. 44: Compared experimentally and numerically thermal effeciency for flat plate.

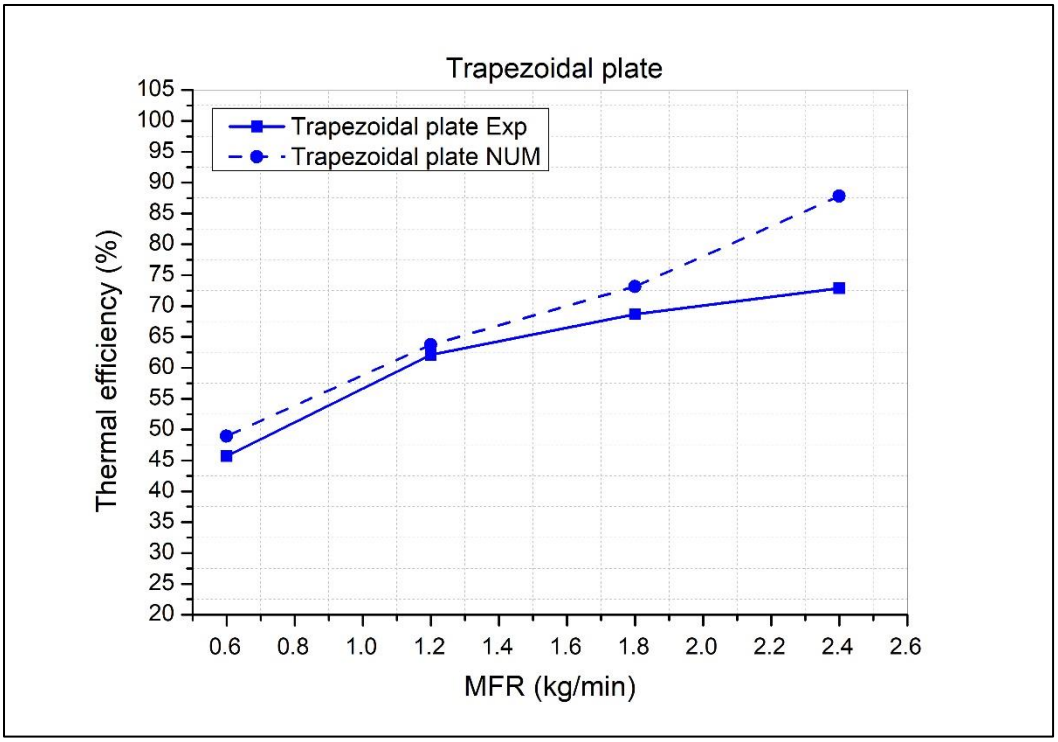

Figure 5. 45: Compared experimentally and numerically thermal effeciency for trapezoidal plate.

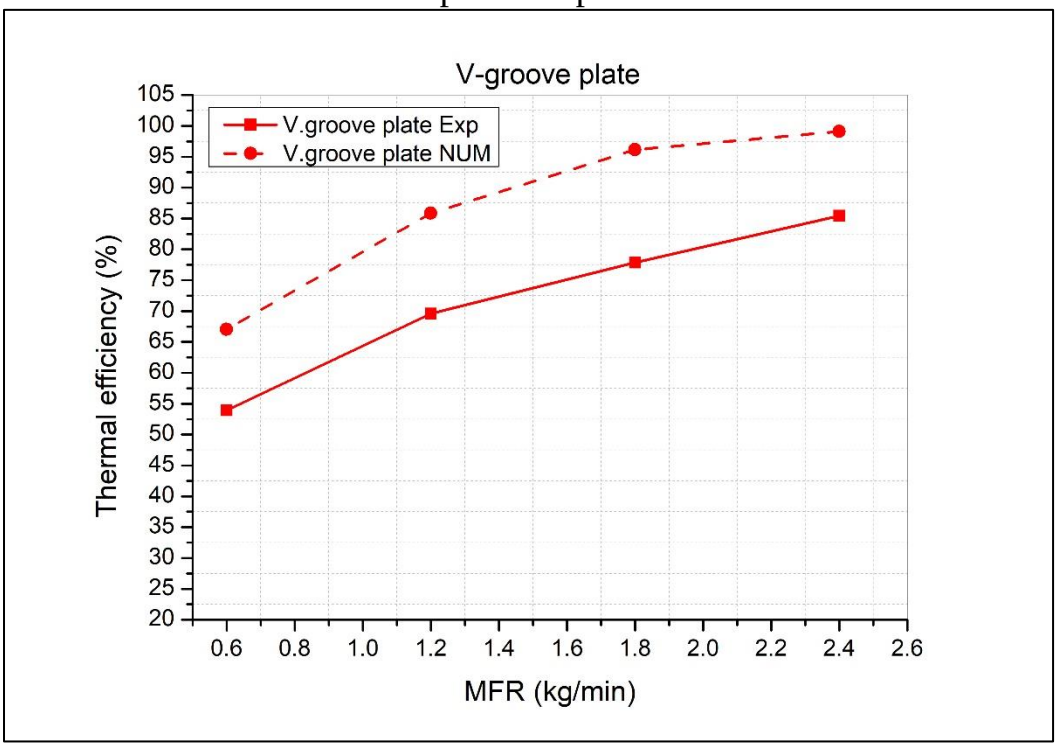

Figure 5. 46: Compared experimentally and numerically thermal effeciency for V-groove plate.

1.3.Error Analysis:

Tables (5.1), (5.2), and (5.3) show the average temperature of the absorption plate, the average temperature of the first and second pass of air, the return temperature, the exit temperature, and the thermal efficiency of the experimental results, numerical results and the error percentage for three models of the absorption plates in the solar air heaters at four MFR. The results shown a reasonable agreement between the experimental and numerical readings.

Table 5. 1: The error ratio between the experimental and numerical analysis for average temperatures and thermal efficiency of the flat plate double-pass solar air heater.

MFR (kg/min)	Type	T_p	$T_{1^{st}pass}$	$T_{2^{nd}pass}$	T_{return}	T_{out}	η_{th}
0.6	Exp	52.5	29	38.7	33.4	41.2	27.69
	Num	58.58	29.39	39.6	33.99	43.48	28.8
	Error	10.37	1.35	2.28	1.75	5.25	3.83
1.2	Exp	41.63	26.7	32	29.7	34.1	44.32
	Num	44.106	27.2	32.4	31.32	35.09	44.83
	Error	5.606	1.85	1.4	5.19	2.82	1.13
1.8	Exp	36.73	26	29.7	28	31.6	55.27
	Num	41.894	26.34	30.215	29.05	32.644	55.35
	Error	12.31	1.308	1.7	3.624	3.198	0.13
2.4	Exp	35.8	23.8	27	25.4	28.3	55.646
	Num	40.19	25.388	28.83	26.347	30.69	56.27
	Error	10.929	6.25	6.35	3.59	7.78	1.1

Table 5. 2: The error ratio between the experimental and numerical analysis for avearage temperatures and thermal efficiency of the trapezoidal plate double-pass solar air heater.

MFR (kg/min)	Type	T_p	$T_{1^{st}pass}$	$T_{2^{nd}pass}$	T_{return}	T_{out}	η_{th}
0.6	Exp	53.2	31.03	43.433	38.4	47.2	45.70
	Num	61.34	34.77	47.37	40.686	50.59	48.94
	Error	13.22	10.747	8.32	5.618	6.713	6.61
1.2	Exp	42.56	28	35.56	32.7	38.5	62.1
	Num	46.17	29.73	36.48	34	38.54	63.72
	Error	7.81	5.83	2.52	3.8	0.124	2.53
1.8	Exp	37.5	27	32.4	30.1	34.7	68.66
	Num	42.31	28.21	33.02	31.14	34.719	73.18
	Error	10.67	4.3	1.87	3.34	0.054	6.17
2.4	Exp	36.8	26.9	31.06	29.1	33.3	72.91
	Num	41.27	27.25	31.44	29.404	33.425	87.8
	Error	10.84	1.3	1.18	1.033	0.373	16.95

Table 5. 3: The error ratio between the experimental and numerical analysis for average temperatures and thermal efficiency of the V-groove plate double-pass solar air heater.

MFR (kg/min)	Type	T_p	$T_{1^{st}pass}$	$T_{2^{nd}pass}$	T_{return}	T_{out}	η_{th}
0.6	Exp	56.96	31.43	48	42.9	51.8	53.92
	Num	67.79	37.2	54.6	45.78	59.1	67
	Error	15.96	15.5	12.12	6.29	10.84	19.5

MFR (kg/min)	Type	T_p	$T_{1^{st}pass}$	$T_{2^{nd}pass}$	T_{return}	T_{out}	η_{th}
1.2	Exp	44.03	27.56	37.366	33.7	39.9	69.57
	Num	48.16	30.78	40.11	34.18	42.5	85.85
	Error	8.57	10.44	6.85	1.418	6.11	18.96
1.8	Exp	39.56	26.7	33.8	31.3	35.9	77.88
	Num	45.19	28.96	35.7	31.618	37.476	96
	Error	12.45	7.8	5.33	1.0	4.2	18.8
2.4	Exp	37.86	26.43	31.23	29.6	32.9	85.46
	Num	41.94	27.89	32.98	29.718	34.3	99
	Error	9.72	5.24	5.3	0.397	5.79	13.74

Chapter six

Conclusions and Recommendations

Chapter six

Conclusions and Recommendations

2.1. Conclusions:

The important conclusions can be summarized in the following points:

1. When the MFR increases, the thermal efficiency of the collector increases, and the temperature difference between the inlet and outlet of the collector decreases, the outlet air temperature of the collector in corrugated is more than that of the flat plate collector.
2. Changing the geometry of the absorbent plate resulted in a significant increase in heat dissipation rate.
3. When comparing the flat absorbing plate of the collector, it was found that the average thermal efficiency of the corrugated plates of the collector increases significantly depending on the solar radiation on the surface of the collector, the rate of air mass flow, and the surface characteristics of the absorbent plate. The heat transfer surface area of the absorbent plate that touches the air is larger and additional turbulence occurs in flow.
4. The maximum thermal efficiency measured experimentally is obtained for the V-groove plate solar air heater compared to the trapezoidal plate solar air heater, which is also higher than the FP-SAH. The thermal efficiency of the V-groove plate is about 85.46 % at MFR of 2.4 kg/min, while for the trapezoidal plate, it is about 72.91 % at MFR of 2.4 kg/min, and for the flat plate is about 55.64 % at MFR of 2.4 kg/min. Thus, the thermal efficiency is improved by up to 34.89 % and 23.68 % for the V-groove and trapezoidal plates, respectively.

5. The difference between the values of energy and entropy created determines the exergy output for a given MFR; it has been observed that when the air's inlet temperature is low, low values of MFR yield the highest exergy output. However, if the air's inlet temperature is high, exergy output will rise with the MFR. Maximum exergy efficiency is 10.04, 16.02 and 21.93 % at MFR at 0.6 kg/min for flat, trapezoidal and V-groove plates, respectively.
6. At MFR of 0.6 kg/min and solar radiation of 825 W/m^2, the highest exergy gain obtained by DP-SAH for flat, trapezoidal and V-groove plates were 33.76, 53.83 and 73.68 W, respectively.
7. Although the pressure of the solar collector decreases in the presence of an absorption plate with a variable geometry than the smooth plate, its value is small to affect the final output of the SAH with a non-flat geometry plate.

2.2.Recommendations:

For future projects, the following suggestions are made:

1. Investigating the effect of a double-glazing cover on the air temperature rise through the solar air heater.
2. Studying the effect of variable air gap in the first and second pass and the inlet temperature on the outlet temperature and the thermal performance of the double pass solar air heater.
3. Studying the effect of other geometries of the absorption plate on the outlet temperature and thermal performance.
4. A combination of different types of absorbent plates, such as corrugated and ribs.

5. Using a porous material as a trapezoidal plate to study its effect on temperature and thermal performance.

6. The effect of the absorbent plate material on heat transfer and thermal efficiency.

References:

[1] S. Sukhatme and J. J. C. S. Nayak, "Solar energy in western Rajasthan," pp. 62-68, 1997.

[2] U. S. E. I. Administration. (2022, April 2022). *U.S. energy facts explained*. Available: https://www.eia.gov/energyexplained/us-energy-facts/

[3] H. H. Abada, A. N. Al-Shamani, and M. D. Faisal, "A grid connected PV system for a rural resident in Al-Najaf, Iraq," in *AIP Conference Proceedings*, 2020, vol. 2290, no. 1, p. 050056: AIP Publishing LLC.

[4] M. M. Alkilani, S. Kamaruzzaman, and M. J. A. J. o. E. S. Sohif, "Fabrication and experimental investigation of PCM capsules integrated in solar air heater," vol. 7, no. 6, pp. 542-546, 2011.

[5] H. F. Oztop, F. Bayrak, A. J. R. Hepbasli, and S. E. Reviews, "Energetic and exergetic aspects of solar air heating (solar collector) systems," vol. 21, pp. 59-83, 2013.

[6] T. Alam, M.-H. J. R. Kim, and S. E. Reviews, "Performance improvement of double-pass solar air heater–A state of art of review," vol. 79, pp. 779-793, 2017.

[7] A. Dewan, P. Mahanta, K. S. Raju, P. S. J. P. o. t. I. o. M. E. Kumar, Part A: Journal of Power, and Energy, "Review of passive heat transfer augmentation techniques," vol. 218, no. 7, pp. 509-527, 2004.

[8] V. Smil, *General energetics: energy in the biosphere and civilization*. Wiley New York, 1991.

[9] S. M. Salih, J. M. Jalil, and S. E. J. R. E. Najim, "Experimental and numerical analysis of double-pass solar air heater utilizing multiple capsules PCM," vol. 143, pp. 1053-1066, 2019.

[10] T. Zhu, Y. Diao, Y. Zhao, and C. J. A. T. E. Ma, "Performance evaluation of a novel flat-plate solar air collector with micro-heat pipe arrays (MHPA)," vol. 118, pp. 1-16, 2017.

[11] J. Duffy, *The sanitarians: A history of American public health*. University of Illinois Press, 1992.

[12] T. Kotas, Y. Mayhew, R. J. P. o. t. I. o. M. E. Raichura, Part A: Journal of Power, and Energy, "Nomenclature for exergy analysis," vol. 209, no. 4, pp. 275-280, 1995.

[13] N. Hajjaji, M.-N. Pons, A. Houas, and V. J. E. P. Renaudin, "Exergy analysis: An efficient tool for understanding and improving hydrogen production via the steam methane reforming process," vol. 42, pp. 392-399, 2012.

[14] A. A. J. E. c. Hegazy and management, "Thermohydraulic performance of air heating solar collectors with variable width, flat absorber plates," vol. 41, no. 13, pp. 1361-1378, 2000.

[15] M. S. Al-Jethelah, A. T. Al-Sammarraie, and H. S. Dheyab, "Air space impact on the performance of a solar air heater," in *Proceedings of the 2019 COMSOL conference in Boston*, 2019.
[16] D. Lakshmi, A. Layek, and P. M. J. E. P. Kumar, "Performance analysis of trapezoidal corrugated solar air heater with sensible heat storage material," *Energy Procedia*, vol. 109, pp. 463-470, 2017.
[17] M. Harde *et al.*, "Performance Enhancement of Solar Air Heater with Jet Impingement on Trapezoidal Absorber Plate," *Int J Innov Res Stud*, vol. 8, pp. 472-479, 2018.
[18] L. Diana, A. G. Safitra, and G. Muhammad, "Numerical Investigation of Airflow in a Trapezoidal Solar Air Heater Channel," in *2019 International Electronics Symposium (IES)*, 2019, pp. 248-253: IEEE.
[19] S. Darici, A. J. H. Kilic, and M. Transfer, "Comparative study on the performances of solar air collectors with trapezoidal corrugated and flat absorber plates," *Heat and Mass Transfer*, vol. 56, no. 6, pp. 1833-1843, 2020.
[20] H. Xiao, Z. Dong, Z. Liu, and W. J. A. T. E. Liu, "Heat transfer performance and flow characteristics of solar air heaters with inclined trapezoidal vortex generators," *Applied Thermal Engineering*, vol. 179, p. 115484, 2020.
[21] J. Reddy, B. Das, and S. J. J. o. B. E. Negi, "Energy, exergy, and environmental (3E) analyses of reverse and cross-corrugated trapezoidal solar air collectors: An experimental study," *Journal of Building Engineering*, vol. 41, p. 102434, 2021.
[22] E. Alic, M. Das, and E. K. J. J. o. C. P. Akpinar, "Design, manufacturing, numerical analysis and environmental effects of single-pass forced convection solar air collector," *Journal of Cleaner Production*, vol. 311, p. 127518, 2021.
[23] K. Joudi, A. J. E. c. Mohammed, and management, "Experimental performance of a solar air heater with a “V” corrugated absorber," *Energy Conversion and management*, vol. 26, no. 2, pp. 193-200, 1986.
[24] A. Kabeel and K. J. R. E. Mečárik, "Shape optimization for absorber plates of solar air collectors," *Renewable Energy*, vol. 13, no. 1, pp. 121-131, 1998.
[25] A. El-Sebaii, S. Aboul-Enein, M. Ramadan, S. Shalaby, and B. J. E. Moharram, "Investigation of thermal performance of-double pass-flat and v-corrugated plate solar air heaters," *Energy*, vol. 36, no. 2, pp. 1076-1086, 2011.
[26] M. Hedayatizadeh, Y. Ajabshirchi, F. Sarhaddi, S. Farahat, A. Safavinejad, and H. Chaji, "Analysis of exergy and parametric study of a v-corrugated solar air heater," *Heat and Mass Transfer*, vol. 48, no. 7, pp. 1089-1101, 2012.
[27] M. Hedayatizadeh, F. Sarhaddi, A. Safavinejad, F. Ranjbar, and H. J. E. Chaji, "Exergy loss-based efficiency optimization of a double-pass/glazed v-corrugated plate solar air heater," *Energy*, vol. 94, pp. 799-810, 2016.

[28] C.-D. Ho, Y.-E. Tien, and H. J. I. J. o. G. E. Chang, "Performance improvement of a double-pass V-corrugated solar air heater under recycling operation," *International Journal of Green Energy,* vol. 13, no. 15, pp. 1547-1555, 2016.
[29] S. Sharma, S. N. J. W. A. o. S. Saha, Engineering, I. J. o. E. Technology, and P. Engineering, "Thermohydraulic performance of double flow solar air heater with corrugated absorber," *World Academy of Science, Engineering Technology, International Journal of Energy Power Engineering,* vol. 11, no. 7, pp. 855-861, 2017.
[30] C.-D. Ho, C.-F. Hsiao, H. Chang, Y.-E. Tien, and Z.-S. J. E. Hong, "Efficiency of recycling double-pass V-corrugated solar air collectors," *Energies,* vol. 10, no. 7, p. 875, 2017.
[31] A. Omer, H. Ndiritu, and S. J. J. O. S. R. I. E. Wanjii, "V-groove Absorber Plate Design Investigation for Flat Plate Solar Collector Using Numerical Simulation," *JOURNAL OF SUSTAINABLE RESEARCH IN ENGINEERING,* vol. 5, no. 3, pp. 128-137, 2020.
[32] A. D. Tuncer, A. Khanlari, A. Sözen, E. Y. Gürbüz, C. Şirin, and A. J. R. E. Gungor, "Energy-exergy and enviro-economic survey of solar air heaters with various air channel modifications," *Renewable Energy,* vol. 160, pp. 67-85, 2020.
[33] A. A. Farhan, A. I. M. Ali, and H. E. J. R. E. Ahmed, "Energetic and exergetic efficiency analysis of a v-corrugated solar air heater integrated with twisted tape inserts," *Renewable Energy,* vol. 169, pp. 1373-1385, 2021.
[34] H. Hassan, M. S. Yousef, S. J. S. E. T. Abo-Elfadl, and Assessments, "Energy, exergy, economic and environmental assessment of double pass V-corrugated-perforated finned solar air heater at different air mass ratios," *Sustainable Energy Technologies and Assessments,* vol. 43, p. 100936, 2021.
[35] M. Metwally, H. Abou-Ziyan, and A. J. R. E. El-Leathy, "Performance of advanced corrugated-duct solar air collector compared with five conventional designs," *Renewable Energy,* vol. 10, no. 4, pp. 519-537, 1997.
[36] M. A. Karim and M. J. E. Hawlader, "Performance investigation of flat plate, v-corrugated and finned air collectors," *Energy,* vol. 31, no. 4, pp. 452-470, 2006.
[37] H. J. R. E. Benli, "Experimentally derived efficiency and exergy analysis of a new solar air heater having different surface shapes," *Renewable Energy,* vol. 50, pp. 58-67, 2013.
[38] E. A. Handoyo, D. Ichsani, and S. Sutardi, "Experimental studies on a solar air heater having V-corrugated absorber plate with obstacles bent vertically," in *Applied Mechanics and Materials*, 2014, vol. 493, pp. 86-92: Trans Tech Publ.

[39] P. Velmurugan and R. J. S. Kalaivanan, "Energy and exergy analysis in double-pass solar air heater," *Sādhanā,* vol. 41, no. 3, pp. 369-376, 2016.
[40] Q. A. Abed, V. Badescu, A. Ciocanea, I. Soriga, and D. J. J. o. N.-E. T. Bureţea, "Models for new corrugated and porous solar air collectors under transient operation," *Journal of Non-Equilibrium Thermodynamics,* vol. 42, no. 1, pp. 79-97, 2017.
[41] S. Li, H. Wang, X. Meng, and X. J. A. t. e. Wei, "Comparative study on the performance of a new solar air collector with different surface shapes," *Applied thermal engineering,* vol. 114, pp. 639-644, 2017.
[42] S. N. Saha, S. J. I. J. o. M. Sharma, and M. Engineering, "Performance evaluation of corrugated absorber double flow solar air heater based on energy, effective and exergy efficiencies," *International Journal of Mechanical and Mechatronics Engineering,* vol. 17, no. 1, pp. 63-76, 2017.
[43] S. J. R. E. Singh, "Experimental and numerical investigations of a single and double pass porous serpentine wavy wiremesh packed bed solar air heater," *Renewable Energy,* vol. 145, pp. 1361-1387, 2020.
[44] R. Khatri, S. Goswami, M. Anas, S. Sharma, S. Agarwal, and S. J. E. R. Aggarwal, "Performance evaluation of an arched plate solar air heater with porous aluminum wire mesh cylindrical fins," *Energy Reports*, vol. 6, pp. 627-633, 2020.
[45] K. Shih, "Indoor test for thermal performance evaluation of Sunworks (liquid) solar collector," 1977.
[46] W. Wang and B. Laumert, "Simulate a ‘sun’for solar research: a literature review of solar simulator technology," 2014.
[47] M. Al-Damook, Z. A. H. Obaid, M. Al Qubeissi, D. Dixon-Hardy, J. Cottom, and P. J. J. N. H. T. Heggs, Part A: Applications, "CFD modeling and performance evaluation of multipass solar air heaters," vol. 76, no. 6, pp. 438-464, 2019.
[48] P. Catalano, M. J. A. s. Amato, and Technology, "An evaluation of RANS turbulence modelling for aerodynamic applications," vol. 7, no. 7, pp. 493-509, 2003.
[49] D. C. Wilcox, *Turbulence modeling for CFD*. DCW industries La Canada, CA, 1998.
[50] H. K. Versteeg and W. Malalasekera, *An introduction to computational fluid dynamics: the finite volume method*. Pearson education, 2007.
[51] A. D. Tuncer, A. Khanlari, A. Sözen, E. Y. Gürbüz, C. Şirin, and A. J. R. E. Gungor, "Energy-exergy and enviro-economic survey of solar air heaters with various air channel modifications," vol. 160, pp. 67-85, 2020.
[52] H. Hassan, M. S. Yousef, S. J. S. E. T. Abo-Elfadl, and Assessments, "Energy, exergy, economic and environmental assessment of double pass V-

corrugated-perforated finned solar air heater at different air mass ratios," vol. 43, p. 100936, 2021.
[53] S. Darici, A. J. H. Kilic, and M. Transfer, "Comparative study on the performances of solar air collectors with trapezoidal corrugated and flat absorber plates," vol. 56, no. 6, pp. 1833-1843, 2020.
[54] A. Biçer, A. G. Devecioğlu, V. Oruç, and Z. J. I. J. o. G. E. Tuncer, "Experimental investigation of a solar air heater with copper wool on the absorber plate," vol. 17, no. 15, pp. 979-989, 2020.
[55] M. Abuşka and S. J. S. E. Şevik, "Energy, exergy, economic and environmental (4E) analyses of flat-plate and V-groove solar air collectors based on aluminium and copper," vol. 158, pp. 259-277, 2017.
[56] H. Jasak, "Error analysis and estimation for the finite volume method with applications to fluid flows," 1996.
[57] A. Doukhi, P. Heggs, and M. J. R. G. Aldamook, "MSc. advanced chemical engineering," vol. 4, no. 6, pp. 345-674, 2019.

Appendix [A]

Spectral distribution and characteristics of tungsten halogen lamps

- Halogen floodlight 500 W, 110-240 V, 50-60 HZ Black.
- Dimensions: (172 × 125) mm^2.
- Manufactured by: Ningbo Start Electrical Co., Ltd. China.

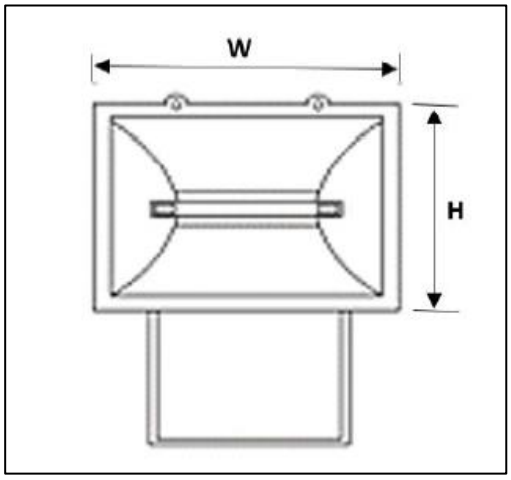

(a) Halogen floodlight photograph.

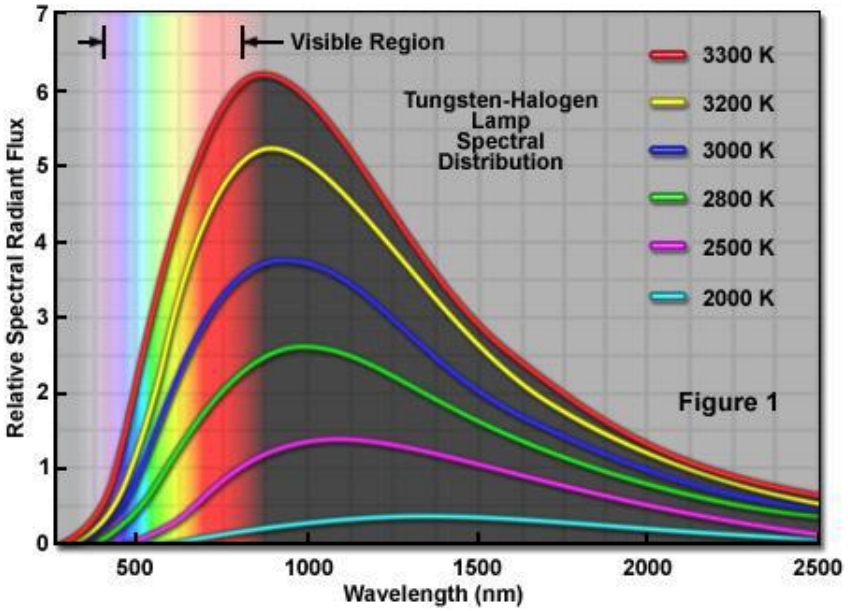

(b) Tungsten halogen lamp spectral distribution.

Appendix [B]

Thermocouples calibration

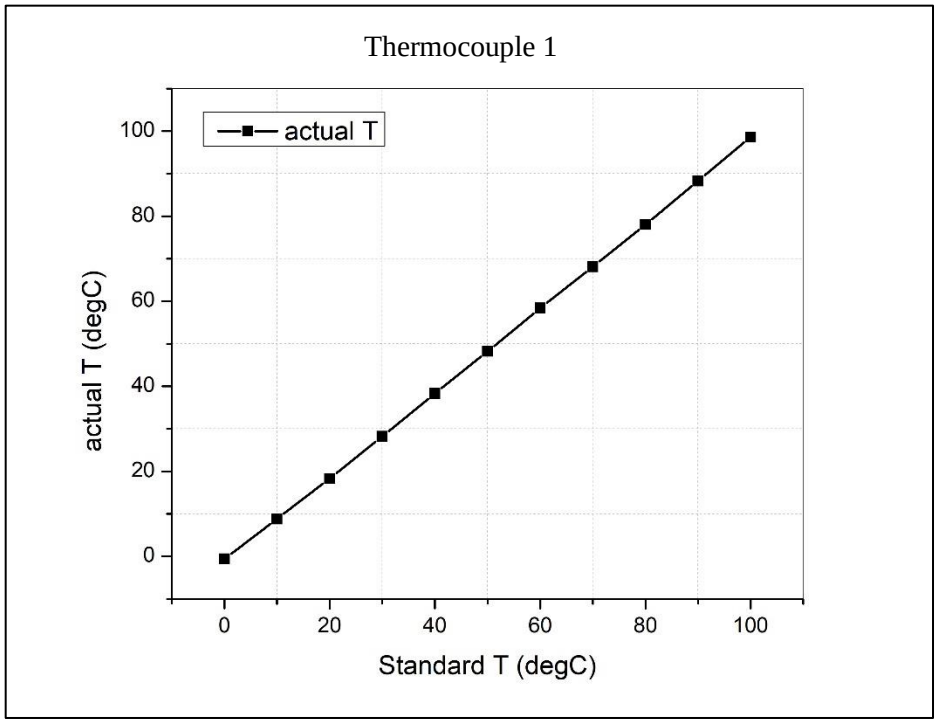

Temp. / senser	0	10	20	30	40	50	60	70	80	90	100
Senser 1	-0.6	8.8	18.3	28.3	38.3	48.2	58.4	68.1	78	88.3	98.6
Senser 2	-0.3	9.2	18.7	28.7	38.7	48.7	58.8	68.5	78.3	88.7	99.4
Senser 3	-0.5	9.2	18.8	28.7	39	49.1	59.3	69.2	79.3	89.6	99.8
Senser 4	-1	8.5	18.2	28.2	38.3	48.3	58.4	68.2	78.2	88.1	97.9
Senser 5	-0.5	9	18.7	28.7	38.7	48.7	58.7	68.4	78.4	88.4	98.1
Senser 6	-0.3	9.3	18.8	28.6	38.8	48.7	58.7	68.5	78.5	88.5	98.7
Senser 7	-0.9	8.5	18.2	28.3	38.4	48.5	58.7	68.6	78.6	89	99.1
Senser 8	-0.2	9.3	18.8	28.7	38.8	48.8	58.8	68.6	78.5	88.9	98.4

Temp. / senser	0	10	20	30	40	50	60	70	80	90	100
Senser 9	-0.7	8.7	18.4	28.4	38.5	48.5	58.9	68.7	78.7	88.9	101.2
Senser 10	-0.4	9.1	18.7	28.6	38.8	48.9	59.1	69	79.1	89.3	99.2
Senser 11	0	9.4	18.9	28.6	38.7	48.6	58.8	68.5	78.6	88.5	98.8
Senser 12	-0.2	9.3	18.9	28.8	39	49	59.3	69.1	79.2	89.5	99.5
Senser 13	0.1	9.2	18.9	28.8	38.8	48.8	58.9	68.6	78.4	88.7	98.4
Senser 14	0.1	9.4	19.1	29	39.1	49.1	59.2	69	78.9	89.1	98.7
Senser 15	0	9.4	19.1	29.1	39.3	49.3	59.4	69.2	79.1	89.1	99.3
Senser 16	-0.6	9.5	19.5	28.5	38	48.9	58	69.2	78.5	88.1	98.4
Senser 17	-0.3	9.7	19.7	28.8	38.5	49.2	59.2	69.3	78.6	88.3	99.2
Senser 18	0	9.8	19.8	28.8	38.4	49	58.9	68.9	78.4	87.8	98.7
Senser 19	-0.1	10	19.9	29.2	38.3	49.8	59.7	69.8	79.3	89.2	100.4

Appendix [C]

Characteristics of the data logger (model AT-4532)

Property	Value
Thermocouple compatibility	K.
Accuracy	0.2% +1 ˚C
Range	From -200 °C to 1300 °C (varies depending on thermocouple)
Resolution	0.1 °C

Channels	32-channel thermocouples
Speed	Fast: 100 m/s – channel Medium: 500 m/s – channel Low: 1 m/s – channel
Correction	Error correction for each channel
Comparator	High and low beep High and low value setting individually for each channel
Interface	U-disc interface RS232C interface Mini UBS (virtual serial port)

Appendix [D]

Anemometer calibration certificate

Appendix [E]

Characteristics of solar power meter (the Pyranometer model TENMARS TM 207)

Property	Value
Range	From 0 to 2000 W/m^2
Temperature Error	± 0.38 ˚C
Drift	< ± 2% per year
Accuracy	±10 W/m^2 or ± 5%
Sampling time	0.25 second
Operating temperature	From 0 °C to 50 °C
Spectral response	400 mm – 1100 mm
Humidity	< 80% RH
Weight	0.5 kg
Dimensions W, D, and H	22.5 cm, 15.75 cm, and 4.75 cm.
Battery	1 pcs 9 V

Appendix [F]

Energy Analysis:

The balance of energy for the SAH system is described by considering the system (SAH) as a united control volume which can be expressed as [51]:

$$\textbf{Accumuated energy in plate } \dot{Q}_{acc} + \textbf{Energy gained by air } \dot{Q}_u = \textbf{Absorbed energy by plate } \dot{Q}_{abs} - \textbf{Energy losses } \dot{Q}_L \quad (1)$$

$$\dot{Q}_{acc} + \dot{Q}_u = \dot{Q}_{abs} - \dot{Q}_L \quad (2)$$

Where the accumulated rate of energy by the absorption plate is computed as follows [51]:

$$\dot{Q}_{acc} = m_p c_{p,p} \left(\frac{dT_{p,m}}{dt}\right) \quad (3)$$

The structural parameters of a SAH, as well as the climatic and environmental variables, have a significant impact on a SAH's thermal efficiency. SAH's energy analysis is expressed in terms of the first law of thermodynamics. The energy gain rate of SAH is found as [54]:

$$\dot{Q}_u = \dot{m} c_p (T_{out} - T_{in}) \quad (4)$$

The rate of solar energy absorption is calculated as follows [54]:

$$\dot{Q}_{abs} = \tau \alpha A_c I \quad (5)$$

The total rate of energy transfer from the collector to the surrounding environment by conduction, convection, and radiation is known as the lost energy rate, and it can be computed as follows [54]:

$$\dot{Q}_L = U_L A_c (T_{abs} - T_a) \quad (6)$$

Heat losses from the solar air heater to the surrounding occurred by all three heat transfer mechanisms. The overall heat loss coefficient of SAH can be defined by [54]:

$$U_L = U_b + U_e + U_t \quad (7)$$

Bottom and edge heat loss coefficients (U_b and U_e) are neglected, and the top heat transfer coefficient from the SAH could be defined as [55]:

$$\boldsymbol{U_t = h_w + h_r} \quad \textbf{8}$$

Where h_w is the heat transfer coefficient related to wind speed, and h_r is the radiation heat transfer coefficient.

Convective heat transfer, which occurs by wind, could be obtained by using the following equation [55]:

$$\boldsymbol{h_w = 2.8 + 3V \quad for \quad 0 \leq V \leq 7\ m/s} \quad 9$$

The radiation heat transfer coefficient that occurs between the solar air heater transparent cover and surrounding could be calculated by the equation [55]:

$$\boldsymbol{h_r = \sigma\varepsilon\left(T_{abs} - T_g\right)\left(T_{abs}^2 + T_g^2\right)\left(\frac{(T_g - T_s)}{(T_g - T_a)}\right)} \quad \textbf{10}$$

Depending on the absorber's temperature and the wind's convective impact over the glass cover, the glass cover experiences the maximum amount of power loss among these components. Consequently, it is found by combining the terms from the following equations [55]:

$$\boldsymbol{\left(M_p c_p \left(\frac{dT_{p,m}}{dt}\right)\right) + \left(\dot{m} c_p (T_{out} - T_{in})\right) = A_c[(\tau\alpha\, I\,) - \left(U_L (T_{abs} - T_a)\right)} \quad \textbf{11}$$

Since we recorded the experimental data for steady-state case, the first term in equations, i.e., $\dot{Q}_{acc}$ is negligible, then equation (3.21) is written as [55]:

$$\boldsymbol{\dot{Q}_u = \dot{Q}_{abs} - \dot{Q}_L} \quad 12$$

The thermal efficiency of solar air heater, η is found by dividing the energy gain rate of solar air heater defined by equation (3.22) by the rate of solar energy absorption determined by equation (3.15) as [55]:

$$\boldsymbol{\eta = \frac{\dot{Q}_u}{\dot{Q}_{abs}}} \quad \textbf{13}$$

Reynolds number (Re) for the flow within the air duct has been written as [55]:

$$Re = \frac{\rho V D_h}{\mu} \quad (14)$$

The hydraulic mean diameter (D_h) of the rectangular duct is determined as follows [55]:

$$D_h = \frac{4A_{cs}}{P} \quad (15)$$

$$D_h = \frac{4(HW)}{2(H+W)} \quad (16)$$

The all-thermos physical properties of the air in the duct are evaluated at the mean temperature of T_m is [55]:

$$T_m = \frac{T_{in}+T_{out}}{2} \quad (17)$$

Exergy analysis:

Considering the SAH and heat collector as one control volume, assuming the steady-state condition, the general mass balance equation can be expressed as follows [53]:

$$\Sigma \dot{m}_{in} = \Sigma \dot{m}_{out} \quad (18)$$

The general balance of exergy equation of solar air heater is expressed as follows [53]:

$$\Sigma \dot{E}x_{in} - \Sigma \dot{E}x_{out} = \Sigma \dot{E}x_{dest} \quad (19)$$

Or:

$$\Sigma \dot{E}x_{heat} - \Sigma \dot{E}x_{work} + \Sigma \dot{E}x_{mass,in} - \Sigma \dot{E}x_{mass,out} = \Sigma \dot{E}x_{dest} \quad (20)$$

Using the equation above, then, the rate of the general exergy balance can be described as follows [53]:

$$\Sigma\left(1 - \frac{T_a}{T_s}\right)\dot{Q}_s - \dot{W} + \Sigma \dot{m}_{in}\Psi_{in} - \Sigma \dot{m}_{out}\Psi_{out} = \dot{E}x_{dest} \quad (21)$$

Where:

$$\Psi_{in} = (h_{in} - h_a) - T_a(S_{in} - S_a) \quad (22)$$

$$\Psi_{out} = (h_{out} - h_a) - T_a(S_{out} - S_a) \quad (23)$$

By substituting equation (3.32) and (3.33) into equations (3.31), then we have [53]:

$$\left(\mathbf{1}-\frac{\boldsymbol{T_a}}{\boldsymbol{T_s}}\right)\dot{\boldsymbol{Q}}_{\boldsymbol{abs}}-\dot{\boldsymbol{m}}[(\boldsymbol{h_{out}}-\boldsymbol{h_{in}})-\boldsymbol{T_a}(\boldsymbol{S_{out}}-\boldsymbol{S_{in}})]=\dot{\boldsymbol{E}}\boldsymbol{x_{dest}} \quad \mathbf{24}$$

Where ($\dot{Q}_{abs}$) is the rate of solar energy absorption by the solar air heater, computed using equation (3.15).

The variations in the enthalpy and the entropy of the air at the SAH are given by [53]:

$$\Delta h = h_{out} - h_{in}$$

$$\boldsymbol{\Delta h = c_p(T_{f,out} - T_{f,in})} \quad \mathbf{25}$$

$$\Delta S = S_{out} - S_{in}$$

$$\boldsymbol{\Delta S = c_p \ln\frac{T_{f,out}}{T_{f,in}} - R \ln\frac{P_{out}}{P_{in}}} \quad \mathbf{26}$$

By substituting equations (3.35), (3.36), and (3.37) into equation (3.34), the equation can be arranged as below [53]:

$$\left(\mathbf{1}-\frac{\boldsymbol{T_a}}{\boldsymbol{T_s}}\right)\boldsymbol{I(\tau\alpha)A}-\dot{\boldsymbol{m}}\boldsymbol{c_p}\left(\boldsymbol{T_{f,out}}-\boldsymbol{T_{f,in}}\right)+\dot{\boldsymbol{m}}\boldsymbol{c_p}\boldsymbol{T_a}\ln\frac{\boldsymbol{T_{f,out}}}{\boldsymbol{T_{f,in}}}-\dot{\boldsymbol{m}}\boldsymbol{R}\boldsymbol{T_a}\ln\frac{\boldsymbol{P_{out}}}{\boldsymbol{P_{in}}}=\dot{\boldsymbol{E}}\boldsymbol{x_{dest}} \quad \mathbf{27}$$

The exergy gain (Ex $_{out}$), is computed by using the following equation [53]:

$$\dot{\boldsymbol{E}}\boldsymbol{x_{out}}=\dot{\boldsymbol{m}}\boldsymbol{c_p}\left(\boldsymbol{T_{out}}-\boldsymbol{T_{in}}-\boldsymbol{T_a}\ln\left(\frac{\boldsymbol{T_{out}}}{\boldsymbol{T_{in}}}\right)\right)-\left(\frac{\dot{\boldsymbol{m}}}{\boldsymbol{\rho}}\right)\Delta\boldsymbol{P}\left(\frac{\boldsymbol{T_a}}{\boldsymbol{T_m}}\right) \quad \mathbf{28}$$

The exergy heat is computed by using the following equation [53]:

$$\dot{\boldsymbol{E}}\boldsymbol{x_{in}}=\left(\mathbf{1}-\frac{\boldsymbol{T_a}}{\boldsymbol{T_s}}\right)\dot{\boldsymbol{Q}}_{\boldsymbol{abs}} \quad 29$$

The exergy efficiency of a solar air heater can be as follows [53]:

$$\boldsymbol{\eta_{ex}}=\frac{\dot{\boldsymbol{E}}\boldsymbol{x_{out}}}{\dot{\boldsymbol{E}}\boldsymbol{x_{in}}} \quad \mathbf{30}$$

Appendix [H]: List of publications

1- Fatima A. Tali, Salah M. Salih, Tahssen Ali Hussain, "**Energy and Exergy analysis for Trapezoidal Plate Double-Pass Solar Air Collector"**; Cite as: "AIP Conference Proceeding", 4th International Conference on Sustainable Engineering Techniques (ICSET 2022)

4th International Conference on Sustainable Engineering Techniques (ICSET 2022)

Baghdad, Iraq, 5-6 October, 2022

Letter of Acceptance and Invitation Ref: 92 Date: 17 / 7 / 2022

Paper ID: 101

Paper Title:

Energy and Exergy Analysis for Trapezoidal Plate Double-Pass Solar Air Collector

Dear Fatima A. Tali , Salah M. Salih , Tahssen Ali Hussain.

With heartiest congratulations I am pleased to inform you that based on the recommendations of the reviewers; your paper identified above has been accepted for publication and oral presentation by *the 4th International Conference on Sustainable Engineering Techniques (ICSET 2022)*. Your paper will be published in the *AIP Conference Proceedings*.

Herewith, the Conference Organizing Committee sincerely invites you to present your paper at the conference to be held at the Middle Technical University / Engineering Technical College, Baghdad, Iraq, 5- 6 October, 2022.

We look forward to your participation in the ICSET 2022.

Yours sincerely,

Prof. Dr. Nabil Jamil Yasin

ICSET 2022 Organizing Committee, Baghdad, Iraq.

https://icset4.tecb.mtu.edu.iq/

2- Fatima A. Tali, Salah M. Salih, Tahssen Ali Hussain, **"The enhancement of the solar air heater energy and exergy by using different absorber designs: Review"**; Cite as: " Tikrit Journal of Engineering Sciences".

?Comments to TJES Editor

.Improve Language is required

Reviewer Recommendation

.Accepted with minor corrections

Reviewer Recommendation

.Accepted with minor corrections

?Return manuscript after reply from Author If you have corrections

yes

الخلاصة

تم فحص كفاءة الطاقة القصوى لسخانات الهواء الشمسية مزدوجة التمرير (DP-SAH) باستخدام ثلاث انواع من الواح الامتصاص (مسطحة وشبه منحرفة وذات اخدود على شكل V) تجريبيا وعدديا. تهدف هذه الدراسة الى تحسين اداء الطاقة القصوى لمجمع الهواء الشمسي من خلال استخدام مسارين مع اشكال هندسية مختلفة لسطح الامتصاص لتوجيه مائع نقل الحرارة مع انخفاض ضغط اقل. تم تحديد تأثير معدل التدفق الكتلي المتنوع وكثافة الطاقة الشمسية على ارتفاع الطاقة وانخفاض الضغط في حالة مستقرة لانواع مختلفة من مجمعات الهواء الشمسي باستخدام محاكاة شمسي داخلي.

تمت الدراسة التجريبية على سخان الهواء الشمسي مزدوج التمرير بابعاد هي (1284 × 320 × 84 مم) بساحة مشروع (0.411) مم^2 ، بأستخدام ثلاث انواع من الواح الامتصاص. لتحقيق جريان مضطرب بالكامل تم الاحتفاظ بنسبة العرض الى الارتفاع (W/H) عند (10) في قناتين من (DP-SAH). تم اخذ الحد الادنى من وحدات الدخول والخروج بناء على معيار ASHARE لمجمعات الطاقة الشمسية الحرارية.

تم اجراء تجارب النظام داخل المختبر باستخدام ستة مصابيح هالوجين من التنجستن كمحاكي لجهاز العرض. وتم تصميم ثلاث الواح امتصاص من معدن الالمنيوم بسمك 0.7 مم ليكون النوع الاول التقليدي (لوحة مسطحة) والنوع الثاني شبه منحرف والنوع الثالث ذات اخدود على شكل V ابعاد كل لوحة هي (1200 × 320 مم).

كذلك تمت الدراسة العددية باستخدام برنامج (COMSOL Multiphysics v5.5) المتاح تجاريا لحل المعادلات الحاكمة ثنائية الابعاء للاستمرارية و Navier Stokes والطاقة وكذلك معادلات نموذج الاضطراب (κ-ε). تم اجراء عمليات المحاكاة الحالية تحت نفس الظروف الحدودية لتأكيد دقة البيانات التجريبية مع متوسط خطأ في الكفاءة الحرارية للسخانات الشمسية بلوحة امتصاص مسطحة وشبه منحرفة ذات اخدود على شكل V (± 1.54 %، ± 8.06 %، ± 17.75 %)، على التوالي، وكانت النتائج مقبولة وجيدة.

اجريت التحقيقات بمعدلات تدفق كتلة الهواء مختلفة (0.6، 1.2، 1.8، 2.4) كغم / دقيقة واشعاع شمسي ثابت يبلغ 825 واط / م^2.

بينت النتائج ان درجة حرارة الهواء تتناسب عكسيا مع معدل تدفق كتلة الهواء، لوحظ ايضا ان كفاءة الطاقة القصوى يعتمدان بشكل كبير على معدل تدفق كتلة الهواء في كل النماذج.

الى جانب ذلك، كانت الكفاءة الحرارية لمجمع الهواء الشمسي مزدوج التمرير ولوحة امتصاص مسطحة وشبه منحرفة وذات اخدود على شكل V عند اجراء التجارب العملية لتتراوح تقريبا بين (27.69 – 55.64) %، و(45.7 – 72.91) %، و(53.92 – 82.46) % على التوالي تحت معدل تدفق كتلة الهواء يتراوح (0.6 – 2.4) كغم / دقيقة، بينما كانت كفاءة الطاقة القصوى لوحة امتصاص مسطحة وشبه منحرفة وذات اخدود على شكل V عند اجراء التجارب العملية لتتراوح تقريبا بين (5.18 – 10.04) % و(9.35 – 16.025) % و(10.3 – 21.93) % على التوالي.

بينما تتراوح الكفاءة الحرارية في التحليل العددي للوحة السطحة (28.8 – 56.27) % وللوحة شبه المنحرفة (48.94 – 87.8) % وللوحة ذات اخدود على شكل V (67 – 99) % على التوالي.

جمهورية العراق
وزارة التعليم العالي والبحث العلمي
جامعة الفرات الاوسط التقنية
الكلية التقنية الهندسية / النجف

تقصي اداء منحني هواء شمسي مزدوج الممر مع انواع متعددة من الواح الامتصاص

رسالة مقدمة الى

قسم هندسة تقنيات ميكانيك القوى في الكلية التقنية الهندسية – النجف / جامعة الفرات الاوسط التقنية

كجزء من متطلبات نيل شهادة الماجستير التقني في هندسة تقنيات ميكانيك القوى

تقدمت بها

فاطمة عبد اللطيف تالي

بكالوريوس هندسة تقنيات ميكانيك القوى

2016

اشراف

م. د. صلاح مهدي صالح **أ. م. د. تحسين علي حسين**

2023 شباط